The Clustering of Dusty Star-Forming Galaxies: Connecting CMB Cosmology and Galaxy Evolution

Graeme Erik Addison

Physics Department and Merton College, Oxford

A thesis submitted for the degree of Doctor of Philosophy
in the University of Oxford.

Trinity Term 2012

For my parents

Declaration

I declare that no part of this thesis has been accepted, or is currently being submitted, for any degree or diploma or certificate or any other qualification in this University or elsewhere. Except where explicit reference is made to the work of others, the work contained in this thesis is my own, and is not the outcome of work done in collaboration.

Chapter 2 is based on work presented in Hajian, Viero, Addison, et al. (2012), published in the Astrophysical Journal (volume 724, page 40). I performed all the model fitting described in Section 2.5 and contributed extensively to the remainder of the paper, including the data presentation, data uncertainty calculations, and conclusions.

Chapter 3 is based on work presented in Addison, et al. (2012), published in the Astrophysical Journal (volume 752, page 120). This work was performed solely by me, with minor edits reflecting comments and suggestions from collaborators and the referee.

Chapter 4 is based on work presented in Addison, Dunkley & Spergel (2012), accepted for publication in the Monthly Notices of the Royal Astronomical Society (arXiv pre-print 1204.5927). This work was performed solely by me, with minor edits reflecting comments and suggestions from collaborators and the referee.

Chapter 5 is based on work from Addison et al. (in preparation). This work was performed solely by me, with minor edits reflecting comments and suggestions from collaborators.

Graeme E. Addison

(August 2012)

Acknowledgements

I am, first of all, indebted to my supervisor, Jo Dunkley, for her infectious enthusiasm, encouragement and unending good advice relating to all aspects of being a scientist. Whether I was writing a paper, planning a talk, applying for jobs, or just stuck on a calculation, I knew I could go to her and come away either the answer I was searching for or the means to go about finding it. Whatever I do in the future, I will not forget how fortunate I was to have been her student.

During my DPhil I have benefited from many useful discussions with colleagues both in Oxford and further afield. I would like to especially thank the members of the cosmology group in Oxford, including Pedro Ferreira, Renée Hlozek, Thibaut Louis, Joe Zuntz, Phil Bull, Doddy Marsh, Tessa Baker, and my collaborators on the Atacama Cosmology Telescope project, notably David Spergel, but also Sudeep Das, Amir Hajian, Blake Sherwin, Lyman Page, Mark Halpern, Mark Devlin, Suzanne Staggs, and others, for all kinds of help and ideas over the past three years.

I am also grateful to my high school physics teachers, whose healthy skepticism of sub-atomic physics only served to fuel my interest. Steve Barrett and Andrew Newsam, from the Universities of Liverpool and John Moores, were the first career physicists I encountered, and the summer work I did with them was the main reason I studied physics at university in the first place. I owe a great deal to several fantastic undergraduate tutors, in particular Michael Bowler, James Binney and Simon Hooker, for their dedication and enthusiasm, and to Pedro Ferreira, for an inspiring couple of cosmology courses. Throughout everything I have undertaken I have been supported and encouraged by my parents, Tricia and Cliff, to whom I dedicate this thesis. Anything I achieve has been because of opportunities I would not have had without them.

Abstract

In this thesis I construct various models to interpret measurements of the clustering of dusty star-forming galaxies through the angular power spectrum statistic. The goals of this work are, firstly, to facilitate the separation of the dusty galaxy contribution from the cosmic microwave background background (CMB) power spectrum, and, secondly, to improve our understanding of the physical properties of these galaxies.

I present analysis of the first cross-correlation of millimeter and submillimeter sky maps, using data from the Atacama Cosmology Telescope (ACT) and the Balloon-borne Large-Aperture Submillimeter Telescope (BLAST), which revealed that the dusty galaxies that dominate the submillimeter sky are, to a significant extent, those same sources that are a nuisance contaminant for CMB cosmology.

I then perform a joint fit to the ACT and BLAST power spectra as well as early results from the *Planck* Surveyor to construct a simple phenomenological template for the frequency and angular scale dependence of the contribution from clustered dusty galaxies to the total power spectrum. This template may be used to assist in extracting the CMB signal from future ACT and other data sets.

The correlation between dusty galaxies and the thermal Sunyaev Zel'dovich effect leads to an additional contribution to the measured angular power spectrum that further hampers constraining quantities of cosmological interest. I present the first physically-motivated model for this correlation, and make predictions for its frequency and scale dependence as a CMB foreground.

Finally, I combine angular power spectrum measurements from ACT, *Planck* and other instruments with deep far-infrared and submillimeter source number counts and constrain a model for the emission properties of these dusty galaxies. I demonstrate that the power spectrum carries significant constraining power and can improve our understanding of dust emission and star formation from unresolved objects at high redshift.

Contents

Chapter 1

Introduction

We are living in the extended golden age of observational cosmology. Measurements of fluctuations in the Cosmic Microwave Background (CMB), relic radiation emitted when the Universe was some four hundred thousand years old, have been central to the emergence of this discipline as a precision science. The original discovery of the CMB in the sixties (Penzias & Wilson, 1965) helped establish the Big Bang as the favoured cosmological theory, and measurements of the correlations in its temperature fluctuations now allow us to probe the composition, geometry and fate of the universe in ever-increasing detail (e.g., Wright et al., 1992; Netterfield et al., 2002; Spergel et al., 2003; Fowler et al., 2010; Keisler et al., 2011). Crucially, measurements of the CMB anisotropy are in good agreement with analysis of several other, independent, cosmological probes, including Type Ia supernovae light curves (for recent results, see Riess et al., 2011) and Baryonic Acoustic Oscillations (BAO; e.g., Percival et al., 2010) in the galaxy correlation function. These data are well-described by the now-standard ΛCDM model. The nature of the dark matter and dark energy that are such key constituents in this model remain elusive, as does a physical mechanism for inflation, the ultra-rapid expansion of the early universe, widely-accepted as the best answer to a number of cosmological questions (e.g., Guth, 1981; Linde, 1982; Albrecht & Steinhardt, 1982). The development of new techniques, instruments and theories to improve understanding of these phenomena thus continues at a great pace.

As data quality improves, we must inevitably confront obstacles to our cosmological advances that could be safely ignored in earlier studies. Astrophysical obstacles – or “foregrounds" – that hamper constraints on the primary CMB anisotropy are of interest in their own right, and indeed contemporary CMB experiments are producing a wealth of new information about, for instance, galaxy clusters, the large-scale distribution of matter through its gravitational lensing of CMB photons, and Galactic dust and synchrotron source properties (e.g., Vanderlinde et al., 2010; Marriage et al., 2011a; Das et al., 2011b; van Engelen et al., 2012; Bennett et al., 2003b; Miville-Deschênes et al., 2008).

In this thesis, I focus on one particular astrophysical obstacle – thermal emission from dust grains that enshroud young stars in distant galaxies. This extragalactic dust emission is one constituent of the cosmic infrared background (CIB; Puget et al., 1996), discovered by an instrument onboard the Cosmic Background Explorer (COBE) satellite, which also hosted the radiometer responsible for the first detection of CMB anisotropy. While the CMB tells us about the universe in its primordial infancy, the CIB was emitted later, following the collapse and virialization of bound structures and the formation of stars and galaxies (see, e.g., review by Kashlinsky, 2005). In contrast to the CMB, the CIB photons were emitted by a range of astrophysical processes over many billions of years. In the near-infrared ($\lambda \sim 1$ μm), some fraction of the CIB photons are redshifted starlight from the first galaxies (at $z \gtrsim 6$). In the far-infrared (FIR; 50 $\mu\mathrm{m} \lesssim \lambda \lesssim 350$ μm), submillimeter (350 $\mu\mathrm{m} \lesssim \lambda \lesssim 1000$ μm) and microwave ($\lambda \gtrsim 1000$ μm), the regions of the spectrum relevant to this work, the CIB is dominated by the thermal dust emission mentioned, associated with dusty galaxies at $0 \lesssim z \lesssim 4$ (with higher wavelengths being more sensitive to high-redshift objects). Material collapsing into supermassive black holes as part of an active galactic nuclei (AGN) phase also contribute some fraction of the photons. The CIB contains a wealth of information about star formation history and galaxy evolution. Extracting this information by resolving the CIB into individual sources has proved challenging. One reason for this in the FIR and longwards is source confusion, arising from the high surface density of sources compared to instrumental beam areas (e.g., Blain et al., 1998). It is not surprising that the statistic of choice for CMB temperature analysis – the angular power spectrum – has emerged as a powerful probe of CIB properties in this case, since the CMB and CIB both appear as fluctuating backgrounds with correlated anisotropies on the degree and arcminute scales to which contemporary missions are sensitive. For the CIB, these correlated anisotropies arise because the dusty galaxies are tracers of large-scale structure, and consequently cluster together rather than being distributed at random (Peebles, 1980). The central theme in this thesis is the modelling of the CIB power spectrum, with the twins goals of, firstly, facilitating its separation from the CMB power spectrum, and, secondly, extracting astrophysical information about the CIB sources themselves.

In the remainder of this introductory chapter, I discuss the cosmological constraints from current CMB temperature anisotropy analysis, and the role of the CIB in hampering this analysis. I then describe the evolution of the large-scale structure that hosts the luminous sources that contribute to the CIB and how the spatial distribution of the CIB sources and other galaxies can be associated with that of the underlying dark matter. Finally, I turn to the relation between dust emission and star-formation rate, and the role of the CIB angular power spectrum in furthering our understanding of galaxy evolution and the star formation history.

1.1 Cosmological constraints from CMB temperature anisotropy

1.1.1 The early universe and origin of the CMB

I begin by outlining the evolution of the Universe in the prevailing Big Bang theory, focussing on the aspects most relevant to the CMB and subsequent structure formation. The Universe is believed to have undergone a period of exponential expansion called inflation after around 10^{-37} seconds, during which the quantum fluctuations of the primordial universe were blown up to macroscopic scales, creating tiny anisotropies in an otherwise homogeneous energy distribution. After inflation, the Universe consisted of a plasma of quarks, gluons, and other elementary particles, and continued to expand and cool; baryons formed after around a microsecond, and electrons after a second. These particles were no longer relativistic but the total energy budget of the Universe was dominated by radiation in the form of photons and relativistic neutrinos. The energy density in radiation falls more quickly than that of non-relativistic matter (see Section 1.2.1), and the two energy densities became equal at $z \approx 3100$. The expansion of the Universe slowed sufficiently for the perturbations in the dark matter density field to begin to grow, however the majority of protons and electrons were not yet in bound systems and so continued to interact with the photons. The baryons and photons existed in a thermal equilibrium and radiation pressure prevented the perturbations in the baryon density from growing. The energy density in radiation continued to decrease until even the most energetic photons were unable to ionize hydrogen, and ‘recombination’ occurred when the Universe was 379,000 years old; most protons and electrons became locked up in hydrogen atoms and the universe rapidly became transparent to photons. The (approximately) two-dimensional surface where the final interactions between photons and baryons took place is known as the surface of last scattering, and the CMB we observe today consists of the photons that have been travelling through space largely undisturbed ever since their final interactions on this surface. After last scattering, perturbations in the baryon density were able to grow, and the dark matter and baryon perturbations eventually led to the formation of the collapsed objects and galaxies that we observe in the more recent universe, which is discussed further in Section 1.2.

1.1.2 Anisotropy in the CMB

The most important cosmological constraints from the CMB come from studying its temperature anisotropies. Consider the difference $\Delta T(\theta,\phi)$ between the CMB temperature at position (θ,ϕ) on a two-dimensional map of the sky and the mean temperature T_0. This ΔT is typically expanded in spherical harmonic functions, $Y_\ell^m(\theta,\phi)$:

$$\frac{\Delta T(\theta,\phi)}{T_0} \equiv \frac{T(\theta,\phi)}{T_0} - 1 = \sum_\ell \sum_{m=-\ell}^{\ell} a_{\ell m} Y_\ell^m(\theta,\phi); \quad T_0 \equiv \frac{1}{4\pi}\int d\Omega\, T(\theta,\phi), \tag{1.1}$$

where the reality of ΔT is ensured by requiring $(a_{\ell m})^* = a_{\ell -m}$. We assume that the universe is, on average, rotationally invariant, thus $\Delta T(\theta,\phi)$ averaged over all skies should vanish (i.e., $\int d\Omega \langle \Delta T(\theta,\phi)\rangle = 0$). This means averages over pairs of $a_{\ell m}$ are related by

$$\langle a_{\ell m} a_{\ell' m'} \rangle = \delta_{\ell,\ell'} \delta_{m,-m'} C_\ell, \tag{1.2}$$

where δ here is the Kronecker delta symbol, and C_ℓ is the angular power spectrum:

$$C_\ell = \frac{1}{4\pi}\int d\Omega\, d\Omega'\, P_\ell(\hat{\mathbf{n}}\cdot\hat{\mathbf{n}}')\, \langle \Delta T(\hat{\mathbf{n}}) \Delta T(\hat{\mathbf{n}}') \rangle, \tag{1.3}$$

where $\hat{\mathbf{n}} = (\theta,\phi)$, $\hat{\mathbf{n}}' = (\theta',\phi')$, and P_ℓ is the Legendre polynomial. It is important to note that we have no access to this C_ℓ: in a cosmic sense all our observations are made at effectively a single point in space, of a single sky. Our $C_\ell^{\rm obs}$ is averaged over m but not observing position; at each multipole, we have access to a sample of only $2\ell+1$ values of $a_{\ell m}$, drawn from the underlying distribution. Consequently, there is a fundamental limit to the accuracy of our measurements of C_ℓ, particularly relevant on large angular scales (low ℓ) – for Gaussian temperature fluctuations, this 'cosmic variance' uncertainty is given by

$$\sigma_\ell = \sqrt{\langle (C_\ell^{\mathrm{obs}} - C_\ell)^2 \rangle} = \sqrt{\frac{2}{2\ell+1}}\, C_\ell. \tag{1.4}$$

The anisotropies arising from the non-uniform nature of the last scattering surface – known as 'primary' anisotropies – are the most important cosmologically, and I briefly review their origin below. These components are shown together in Figure 1.1, taken from a review by Scott & Smoot (2006).

Sachs-Wolfe (SW) effect ($\ell \lesssim 100$)

Fluctuations in the gravitational potential cause CMB photons to be slightly redshifted or blueshifted at the point on the last scattering surface from which they are emitted. This effect is partially cancelled by the fact that the expansion rate of the universe is slowed in the vicinity of an overdensity (i.e., negative potential), meaning that the redshift of last scattering is decreased, and so photons from overdense regions lose less energy on their subsequent journey to a present-day observer. The net temperature shift is given by $\Delta T^{\mathrm{SW}}(\hat{\mathbf{n}})/T_0 \approx \delta\phi(\hat{\mathbf{n}} r_L)/3$, where r_L is the distance to the last scattering surface. The primordial density and potential fluctuations are related via the Poisson equation (see Section 1.2.2); the angular power spectrum from SW temperature fluctuations can thus be used to constrain the power spectrum of primordial density fluctuations, which simple inflationary models predict to vary with wavenumber as $P(k) \propto k^{n_s}$, with $n_s \lesssim 1$. For $n_s = 1$, the SW angular power $C_\ell^{\mathrm{SW}} \propto 1/\ell(\ell+1)$, and for this reason the CMB angular power spectrum is conventionally plotted as $\ell(\ell+1)C_\ell$ (actually $\ell(\ell+1)C_\ell/2\pi$), rather than simply C_ℓ.

CMB photons also experience gravitational redshifts and blueshifts from fluctuations in potential along their path from the last-scattering surface to our telescopes. This effect, known as the Integrated Sachs-Wolfe (ISW) effect, is expected to dominate the SW on very large angular scales (see Figure 1.1), although it has yet to be detected at a high level of statistical significance.

Acoustic peaks ($100 \lesssim \ell \lesssim 1000$)

Prior to recombination, protons, electron and photons existed in a thermalised plasma. Gravitational potentials had been growing since matter-radiation equality thanks to evolving dark matter density perturbations, and the baryons also experience the gravitational attraction, however baryonic density perturbations are prevented from growing by the photon radiation pressure. This acts as a restoring force against the gravitational attraction, and leads to oscillations in the baryon density. At recombination, these oscillations are imprinted into the temperature of the CMB photons, and manifest themselves in the CMB power spectrum as a series of peaks. The first peak corresponds to modes that have completed half an oscillation at recombination, and the position of this peak in ℓ constrains the angular diameter distance to last scattering, and thereby the geometry (curvature) of the universe for any given cosmological model. Furthermore, every other peak receives an enhancement from the baryon momentum providing an additional term in the plasma oscillation equation, meaning ratios of adjacent peaks may be used to constrain the baryon fraction, Ω_b.

Damping tail ($\ell \gtrsim 1000$)

Temperature and density anisotropies on the last scattering surface are damped on physical scales less than the mean distance travelled by photons during the recombination period. The photons diffuse from hot, dense regions to less-dense, cooler regions and drag the baryons with them (Silk, 1968). This phenomenon is known as Silk Damping and smooths out the acoustic peaks, rapidly reducing the CMB anisotropy power, for multipoles $\ell \gtrsim 1000$. It should be noted that useful cosmological constraints can still be obtained from the damping tail, even though the acoustic peaks are increasingly less pronounced (see Section 1.1.4, below).

1.1.3 CMB experiments

Before quantifying the latest cosmological constraints from CMB temperature anisotropy measurements I briefly overview several of the recent and current CMB missions.

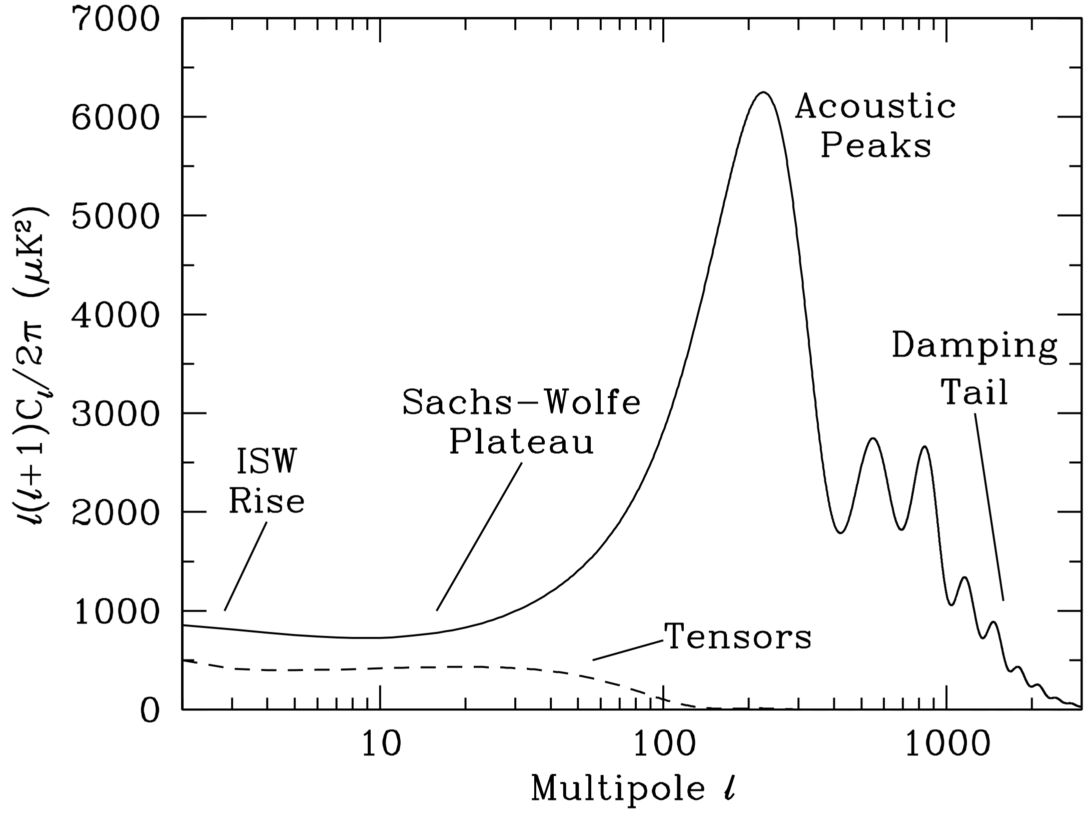

Figure 1.1: Primary anisotropies in the CMB, taken from the review by Scott & Smoot (2006). The y-axis is plotted such that the Sachs-Wolfe plateau would be flat for scale-independent initial conditions ($n_s = 1$). A theorised sub-dominant contribution from primordial tensor fluctuations is also shown. The Wilkinson Microwave Anisotropy Probe (*WMAP* – see Section 1.1.3) provides constraints on the power for $\ell \lesssim 1000$; recovering the damping tail on smaller (arcminute) scales requires an understanding of the foreground signals that contribute to the total measured anisotropy power (Sections 1.1.4 and 1.1.5).

Wilkinson Microwave Anisotropy Probe

The Wilkinson Microwave Anisotropy Probe (*WMAP*; Bennett et al., 2003a) is a satellite that was launched in 2001 and measured CMB temperature and polarisation anisotropies on angular scales of roughly ten arcminutes and larger ($\ell \lesssim 950$) across the whole sky until 2010. *WMAP* clearly detected the first three acoustic peaks in the CMB temperature anisotropy power spectrum and provided unprecedented constraints on cosmological parameters (Spergel et al., 2003, 2007; Dunkley et al., 2009; Komatsu et al., 2011). This thesis does not deal directly with *WMAP* data, since *WMAP* observes at sufficiently low frequencies ($\nu \lesssim 100$ GHz), on large enough angular scales ($\ell \lesssim 1000$), that extragalactic dust emission is not a significant contaminant, however, analysis of small-scale CMB temperature anisotropy measurements from Atacama Cosmology Telescope and South Pole Telescope data (see below) is performed in conjunction with *WMAP* data, since these ground-based instruments view smaller fractions of the sky and have limited capability to measure anisotropy on large scales (low multipoles).

Atacama Cosmology Telescope

The Atacama Cosmology Telscope (ACT; Fowler et al., 2007; Swetz et al., 2011; Dünner et al., 2012) is a 6 m telescope located in Chile's Atacama Desert. It observed the microwave sky at approximately 150 and 220 GHz with arcminute resolution between 2007 and 2011, with a total of some 900 square degrees usable for small-scale CMB power spectrum calculations (for more details, see Section 2.2.1). As well as constraining cosmological parameters using the power spectrum directly (Fowler et al., 2010; Dunkley et al., 2011), ACT's other main science goal is providing a mass-limited sample of galaxy clusters detected using the thermal Sunyaev Zel'dovich effect (see below and Marriage et al., 2011a). Such a sample can be used to test the standard cosmological model, structure formation theories and primordial non-Gaussianity, provided the cluster mass or other physical attributes can be reliably inferred from the tSZ effect (e.g., Sehgal et al., 2011; Benson et al., 2011). Numerous opportunities for cross-correlation studies are also available, particularly with optical data from the Sloan Digital Sky Survey (SDSS[a]). Several notable ACT results are mentioned in the following sections. The upcoming ACTPol survey (Niemack et al., 2010) will measure arcminute-scale anisotropies in the polarisation of CMB

---

[a] http://www.sdss.org/

photons, aiming to significantly improve constraints on CMB lensing (see below) and neutrino masses.

I am a member of the ACT team and much of this thesis (Chapters 2, 3 and 5) involves modelling the dusty galaxy contamination in the measured ACT power spectra or cross-correlations between ACT and other data sets.

South Pole Telescope

The South Pole Telescope (SPT; Carlstrom et al., 2011) is a 10 m telescope at the South Pole, which shares many science goals with ACT. The SPT-SZ survey covered 2500 square degrees, measuring the CMB temperature at 95, 150 and 220 GHz, also with arcminute resolution. An upgraded, polarisation-sensitive, camera is currently scanning the sky as part of the SPTpol survey (McMahon et al., 2009).

Planck Surveyor

The *Planck* surveyor (Tauber et al., 2010; Bersanelli et al., 2010; Lamarre et al., 2010; Planck Collaboration et al., 2011a) has observed the full sky from 100 to 857 GHz, with observations at 30 to 70 GHz still ongoing. Temperature maps and cosmological constraints are expected in early 2013. The angular resolution of the main cosmology channels of *Planck* (100, 143 and 217 GHz) is around 6 arcminutes, a factor of two improvement over *WMAP*. The other frequency channels are intended to be used for foreground removal (removing dust contamination at higher frequencies – see below – and synchotron emission at lower frequencies).

It should be noted that various other instruments, including Bolocam (Sayers et al., 2009), QUaD (Brown et al., 2009; Friedman et al., 2009), APEX-SZ (Reichardt et al., 2009b), ACBAR (Reichardt et al., 2009a), SZA (Sharp et al., 2010), BIMA (Dawson et al., 2006), and CBI (Sievers et al., 2009), have made measurements of the small-scale CMB power spectrum in recent years. Results from these instruments are not used or discussed further in this work, since ACT and SPT measurements are in excellent agreement and, in conjunction with *WMAP*, span a wider range of angular scales with far higher signal-to-noise.

1.1.4 Latest constraints from small-scale CMB temperature anisotropy

In this section, I discuss several specific examples of the cosmological constraints that are being obtained from current CMB experiments; it is to improve constraints on these quantities that we must strive to understand the small-scale foregrounds (for a recent discussion of the impact of foregrounds on parameter constraints, see Millea et al., 2012).

Primordial power spectrum

Constraining the primordial power spectrum of matter fluctuations, $P(k)$, with measurements of the Sachs-Wolfe plateau and Silk damping tail, is currently of great interest; the current best CMB-only constraint on n_s comes from joint analysis of *WMAP* and SPT data, which yielded $n_s = 0.966 \pm 0.011$ (Keisler et al., 2011), an improvement over $n_s = 0.967 \pm 0.014$ from *WMAP* alone. There is thus a $\sim 3\sigma$ preference for $n_s < 1$, and increasing the significance of this deviation from unity would provide strong support for some kind of inflation in the early universe, given the absence of alternative paradigms predicting deviations from scale-independent initial conditions.

Dunkley et al. (2011) and Keisler et al. (2011) also found a mild (almost 2σ) preference for running (scale dependence) in the spectral index, parametrized as $dn_s/d\ln k$, of -0.034 ± 0.018 and -0.024 ± 0.013, respectively. As with $n_s \neq 1$, finding $dn_s/d\ln k \neq 0$ has implications for the form of the inflationary potential (Kosowsky & Turner, 1995).

Number of relativistic species

In the standard cosmological model, the number of relativistic species in the early universe, $N_{\rm eff} = 3.046$ (three neutrino species plus an extra contribution from electron-positron annihilation; Dicus et al., 1982). Extra relativistic species would cause a reduction in power of the damping tail (Hu & White, 1996), which, as with n_s, can be constrained using ACT or SPT data in conjunction with *WMAP*: Dunkley et al. (2011) and Keisler et al. (2011) find $N_{\rm eff} = 5.3 \pm 1.3$ and 3.85 ± 0.62, respectively. Continued efforts over the coming few years should reveal whether these data really are hinting at additional relativistic species in the early universe, which would have significant cosmological and particle physics implications.

Other early-universe phenomena

ACT and SPT data have also been used to improve constraints on a number of additional, non-standard, cosmological phenomena, including early dark energy (e.g., Calabrese et al., 2011; Reichardt et al., 2012a), cosmic strings (Dunkley et al., 2011), and primordial tensor perturbations (Dunkley et al., 2011; Keisler et al., 2011).

1.1.5 Secondary anisotropies and foregrounds

The CMB blackbody peaks at a frequency of 160.4 GHz, but even at this frequency is it is far from the only signal in the sky, and correlated anisotropies from other sources come to dominate those in the CMB on small angular scales. In this section I focus on the secondary anisotropies (from interactions of CMB photons after last scattering), and foregrounds (non-CMB photons), important for $\nu \gtrsim 100$ GHz, which may prevent improvements in cosmological parameters discussed above. Figure 1.2, taken from Dunkley et al. (2011) shows how these foregrounds come to the dominate the primary CMB on small angular scales.

Gravitational lensing of CMB photons

General Relativity predicts that photons' paths should be deflected in the presence of gravitational masses, and lensing by large-scale structure affects the CMB photons collected by our telescopes, causing small deflections in their paths (see Lewis & Challinor, 2006, for a review). These deflections act to slightly smooth out the peaks in the power spectrum, particularly in the damping tail; the most significant detection of this effect on the C_ℓs has been made using *WMAP* and SPT data – Keisler et al. (2011) report a detection at the 4σ level of significance. The effect of the lensing has been detected in the cross-correlation of CMB maps with luminous tracers of the large-scale structure that is responsible for the lensing at similar significance levels (e.g., Smith et al., 2007; Bleem et al., 2012; Sherwin et al., 2012), and through calculating the angular power spectrum of the photon deflection angles (as opposed to the temperature anisotropy power spectrum; Das et al., 2011b; van Engelen et al., 2012). Future measurements of the lensing of CMB photons may help constrain cosmological parameters – particularly those relating to the growth of structure – directly, as well as improving constraints on the bias of luminous source populations (including CIB sources) through cross-correlation.

Thermal Sunyaev Zel'dovich effect

CMB photons interact with free electrons as they travel through space, most importantly the hot electrons in the intergalactic medium of massive galaxy clusters (Sunyaev & Zel'dovich, 1970). Due to the energy of these electrons the interaction is by inverse-Compton scattering, and results in an increase in photon energies along lines of sight that pass through clusters. This is known as the thermal Sunyaev Zel'dovich (tSZ) effect and it induces a frequency-dependent shift in the CMB temperature, which, if the cluster electrons are assumed to be non-relativistic, is given by

$$\frac{\Delta T_\nu^{\mathrm{tSZ}}}{T_0}(\hat{\mathbf{n}}) = g_\nu \frac{\sigma_T}{m_e c^2} \int \frac{dx}{dz} \frac{dz}{1+z} n_e(\hat{\mathbf{n}}, z)\, k_B T_e(\hat{\mathbf{n}}, z), \tag{1.5}$$

where σ_T is the Thomson cross-section, $m_e c^2$ the electron rest energy, dx the comoving line element along the line of sight, n_e the electron density, T_e the electron temperature, and the spectral function, g_ν, is given by

$$g_\nu = x \frac{e^x + 1}{e^x - 1} - 4, \tag{1.6}$$

where $x = h_P \nu / k_B T_0$. Note that $g_\nu < 0$ for $\nu \lesssim 217$ GHz. This is essentially because the tSZ effect results in a deficit of low-energy electrons. The electron temperature in massive clusters can reach $10^7 - 10^8$ K, and relativistic corrections are consequently expected to modify ΔT^{tSZ} by around ten per cent (e.g., Nozawa et al., 1998, 2006).

The tSZ contribution to the measured angular power spectrum depends on the spatial distribution and number density of galaxy clusters as a function of their electron temperature (e.g., Komatsu & Kitayama, 1999; Komatsu & Seljak, 2002). It is also dependent on any variation in the electron temperature distribution within an individual cluster, since the angular size subtended by a cluster (typically a few arcminutes) is comparable to the scales on which useful cosmological constraints can be obtained from the primary CMB damping tail, and the measured spectrum is thus somewhat sensitive to the cluster substructure. Some details of the tSZ power spectrum calculation are discussed in Chapter 4, however several points are worth making here. Firstly, if the clusters contributing to the tSZ could all be identified in the CMB maps and masked (removed) before the spectrum is calculated, the tSZ would not be relevant as a CMB foreground. This is not the case; with the sensitivity of current CMB missions, most of the tSZ power spectrum comes from unresolved clusters (e.g., Komatsu & Kitayama, 1999; Shaw et al., 2009; Marriage et al., 2011a). Secondly, the characteristic frequency dependence of the tSZ effect facilitates its separation from the primary CMB, especially because the tSZ null ($g_\nu = 0$) at around 217 GHz coincides with a window in atmospheric absorption, allowing both ground-based and satellite telescopes to observe the CMB in the virtual absence of any tSZ contamination. Lastly, the tSZ power spectrum is of cosmological interest in its own right, because it can be used as a probe of the abundance of clusters and groups. This makes it very sensitive to the cosmological parameter σ_8, the r.m.s. mass fluctuation in a sphere of radius $8h^{-1}$ Mpc; current models predict $C_\ell^{\mathrm{tSZ}} \propto \sigma_8^{\sim 8}$ (e.g., Bond et al., 2002; Komatsu & Seljak, 2002; Trac et al., 2011).

Kinematic Sunyaev Zel'dovich effect

The above discussion neglects the effect of any bulk velocity of the electrons that scatter the CMB photons. If $\mathbf{v}(\hat{\mathbf{n}}, z)$ is the bulk electron velocity relative to the CMB rest frame then an anisotropy is induced in the measured CMB temperature, given by (Sunyaev & Zeldovich, 1972, 1980)

$$\frac{\Delta T^{\mathrm{kSZ}}}{T_0}(\hat{\mathbf{n}}) = \frac{\sigma_T}{c} \int \frac{dx}{dz} \frac{dz}{1+z} n_e(\hat{\mathbf{n}}, z)\, e^{-\tau(z)}\, \hat{\mathbf{n}} \cdot \mathbf{v}(\hat{\mathbf{n}}, z), \tag{1.7}$$

where $\tau(z)$ is the optical depth to redshift z. We will refer to this anisotropy as the kinematic Sunyaev Zel'dovich (kSZ) effect, although it is also called the Ostriker-Vishniac (OV; Ostriker & Vishniac, 1986; Vishniac, 1987) effect when referring to the contribution from perturbations in the linear regime of structure formation. There is a contribution to the kSZ effect from bulk motion of electrons in massive clusters, although the majority of the kSZ angular power spectrum comes from large-scale, coherent motion in the intergalactic medium (IGM) at higher redshift ($z > 3$; see, e.g., Hernández-Monteagudo & Ho, 2009; Sehgal et al., 2010, and references therein). The kSZ anisotropy is independent of frequency, in contrast to the tSZ, and preserves the CMB blackbody. Like the tSZ effect, the kSZ effect is of cosmological interest in its own right; it seems likely that the lasting cosmological contribution from small-scale CMB temperature anisotropy measurements from ACT and SPT will be in improved SZ constraints. Upper limits on the kSZ power spectrum have already ruled out a large class of 'void' models, whereby the apparent acceleration of the universe may be explained by the fact that the local group is situated near the centre of a large underdense region or void, without requiring dark energy (Bull et al., 2012). Joint analysis of ACT and Baryon Oscillation Spectroscopic Survey (BOSS[b]) data have recently led to the first convincing detection of the kSZ effect from the large-scale motion of galaxy clusters (Hand et al., 2012). This measurement, and future improvements, have the potential to provide information about the 'missing baryon' problem, as well as constraining dark energy and modified gravity models.

The kSZ power spectrum is sensitive to fluctuations in the ionization fraction through $n_e(\hat{\mathbf{n}}, z)$. Of great current interest is the potential for kSZ measurements to constrain the epoch of reionization, in particular the duration of a possible 'patchy' reionization scenario (e.g., Knox et al., 1998; Santos et al., 2003; Iliev et al., 2006; Mesinger et al., 2012), in which ionized bubbles nucleate and then expand over time (as opposed to the universe becoming ionized more-or-less instantaneously). Measurements of the kSZ power spectrum are, at least until the next generation of 21 cm surveys, perhaps our only probe of the formation of the first stars on a global (rather than source-by-source) basis. ACT and SPT are expected to have the sensitivity required to detect the kSZ power from patchy reionization, but foreground uncertainties (in particular, the correlation between the tSZ effect and the CIB sources, which is addressed in detail in Chapter 4) mean the constraints that will be obtained are not yet certain.

Extragalactic point sources

Broadly speaking, two populations of galaxies are expected to contribute to the measured power spectrum in the microwave bands: the dust-dominated sources that are the main subject of this thesis and synchotron-dominated radio sources (e.g., White & Majumdar, 2004). In the microwave bands the observed flux of these sources depends on frequency roughly as $S_\nu \propto \nu^\alpha$ with $\alpha \sim 3.5$ for the dusty sources and $\alpha \sim -0.5$ for the radio sources (e.g., Vieira et al., 2010; Marriage et al., 2011b). Unresolved point sources contribute a Poisson shot-noise term to the total angular power spectrum (e.g., Bond, 1996; Scott & White, 1999), which is independent of ℓ for current arcminute CMB experiments because, with this resolution, these galaxies are effectively point sources (nearby galaxies may subtend an arcminute or more, but these sources can be masked by cross-referencing with existing galaxy catalogues). Of more

---

[b] http://www.sdss3.org/surveys/boss.php

concern as a CMB foreground is the contribution to the power spectrum from clustered galaxies; the clustering of dusty galaxies is addressed in more detail in Section 1.3 as well as Chapters 2, 3, and 5, and arises because the galaxies are (biased) tracers of the underlying dark matter density (Peebles, 1980). The power spectrum of density fluctuations is scale-dependent at all epochs, and many galaxy populations exhibit strong clustering behaviour, being preferentially located nearer to other galaxies than would be expected for a random spatial distribution. Clustered dusty galaxies contribute significant ℓ-dependent power to the measured C_ℓ (Hall et al., 2010; Dunkley et al., 2011; Shirokoff et al., 2011; Reichardt et al., 2012b). The contribution from the clustering of radio galaxies has been neglected in contemporary CMB analysis based on extrapolations from lower frequencies (e.g., Hall et al., 2010, and references therein), however the power from clustered dusty galaxies has been found to contribute around ten percent of the total measured power at $\ell = 3000$ for 150 GHz, and perhaps a third of the total for 220 GHz (Reichardt et al., 2012b).

The role of point sources as a CMB foreground would be greatly reduced if a significant proportion were bright enough to be identified and masked from maps prior to calculating the power spectrum. The radio sources are, on average, far brighter than the dusty sources and many are indeed resolved and masked in ACT and SPT analysis, reducing the radio source contribution to the power spectrum by as much as 90% (Hall et al., 2010; Fowler et al., 2010; Shirokoff et al., 2011). Unfortunately, the same is not true of the dusty sources, with their Poisson power contribution being reduced by around 5% from the masking of resolved objects (based on integrating the resolved counts from Vieira et al., 2010). Even if the instrumental noise in the maps could be reduced, source confusion due to the high number density of sources per beam area (e.g., Blain et al., 1998) would prevent more than a tiny fraction of objects being resolved (this fact means that the usefulness of the angular power spectrum as a statistic to probe the properties of the dusty sources is considerably increased – see Section 1.4).

The frequency dependence of the dusty galaxy power (whether Poisson or clustered) is not as straightforward as for the tSZ effect; there is no special frequency where the flux from dusty sources is minimised. The dusty source brightness decreases faster than that of the CMB in the low-frequency Rayleigh Jeans tail, but atmospheric absorption and the increasing importance of synchotron emission (both Galactic and extragalactic) means this fact cannot easily exploited, as least from the ground.

Galactic dust (cirrus)

ACT and SPT fields were chosen to minimise Galactic contamination; diffuse thermal emission from dust within the Milky Way (known as ‘cirrus’, after the diffuse clouds which have a similar appearance), contributes only at the per cent level to the angular power spectrum at 150 GHz (Hall et al., 2010; Das et al., 2011a). The cirrus power is a more significant contaminant for measurements of the dusty galaxy power spectra at submm and FIR bands (see Chapters 2 and 5). The cirrus has a strongly scale-dependent power spectrum, falling off with ℓ as $C_\ell^{\rm cirrus} \propto \ell^{-n_{\rm cirrus}}$ with $n_{\rm cirrus} \approx 2.5-3.5$ based on measurements in the far-infrared (e.g., Gautier et al., 1992; Finkbeiner et al., 1999; Miville-Deschênes et al., 2005, 2007).

Other Galactic foregrounds, including synchotron, spinning dust and free-free emission (e.g., Haslam et al., 1982; Draine & Lazarian, 1999; Bennett et al., 2003b; Miville-Deschênes et al., 2008), are important at lower frequencies, and in polarisation measurements, however they are subdominant in the ACT and SPT bands.

1.2 Large-scale structure

I now turn to the evolution of the tiny density perturbations left from inflation and how they are associated with the more complex structure – galaxies, clusters, and so forth – that formed later. Apart from the CMB at redshift $z \sim 1100$, we have no direct observations of the period of ‘dark’ structure formation that began with the onset of matter domination ($z \sim 3100$) and ended with the formation of the first stars and luminous objects (and as yet we have no observations of the first generation of these objects either). Fortunately, analytic approaches and numerical simulations present a qualitatively consistent picture of this epoch. In brief, gravitation caused the initially overdense regions (where the local density, $\rho(\mathbf{r})$, exceeds the global mean, $\bar{\rho}$) to become more overdense, and conversely the underdense regions to become more underdense. The overdense regions, starting with the very densest, eventually possess the critical depth of gravitational potential required to overcome cosmic expansion and cause matter to begin to fall together. This leads to the virialization of collapsed regions or ‘haloes’. Meanwhile, the increasingly rapid expansion of the underdense regions causes the overdense regions to become clumped together in sheets or filaments (the filamentary nature of the distribution of the matter around the large underdense volumes led to the term ‘cosmic web’). Within these filaments, potentials continue to deepen

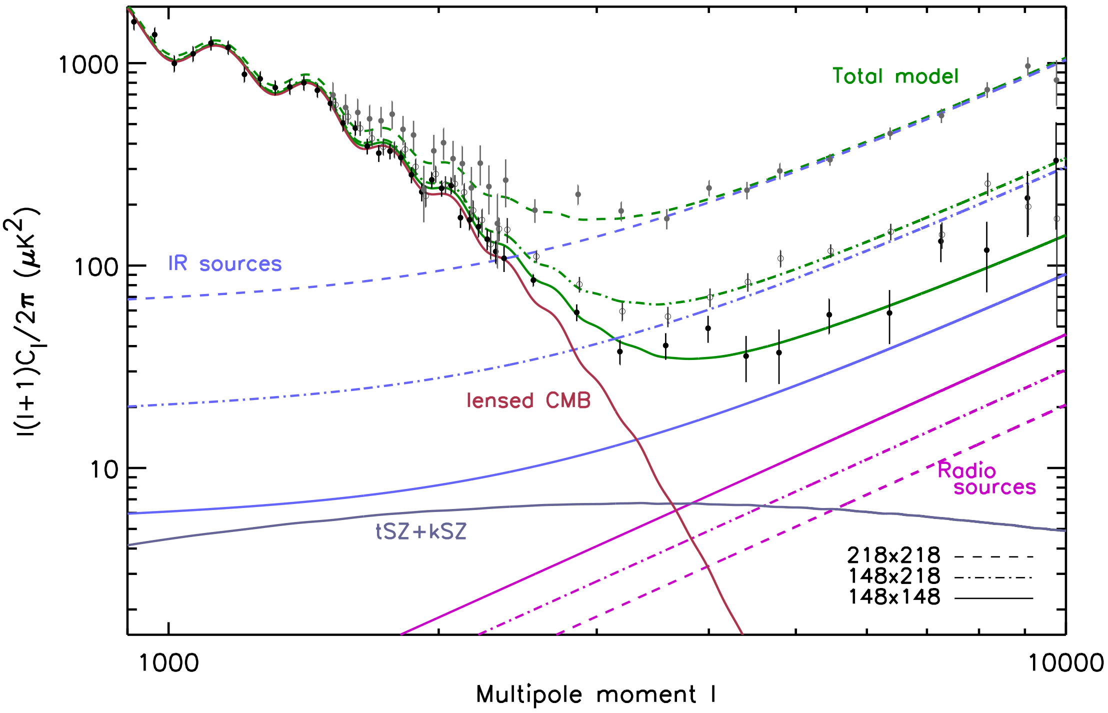

Figure 1.2: ACT power spectrum plot from Dunkley et al. (2011). The data points are the total measured anisotropy power spectrum from maps at 148 GHz, 218 GHz and from the cross-correlation of the 148 and 218 GHz maps. Infrared (IR) sources (the dusty galaxies that are the focus of this thesis), the Sunyaev Zel'dovich effect and, to a lesser extent, radio sources, dominate the primary CMB power on scales of a few arcminutes and less. These foregrounds must be understood in order to extract cosmological constraints from the small-scale CMB signal.

and more and more massive haloes are formed through the merging of existing, less massive ones. In this way, structure formation proceeds hierarchically, or 'bottom up', with low-mass objects forming initially and more massive ones following. The smaller haloes that are accreted into more massive bodies are called subhaloes, while their hosts are called primary haloes.

In the standard cosmological model, baryonic matter contributes only a sixth of the total matter density, and an understanding of structure formation can be gained even if we ignore the star formation, radiation pressure, and other complications associated with the baryons, and study only the dark matter – this is fortunate, as accounting for the baryonic behaviour remains a challenge even for state-of-the-art simulations.

1.2.1 FLRW metric

The spatial geometry of a homogeneous and isotropic universe is described by the following equation, which we will refer to as the FLRW metric, after Friedmann, Lemaître, Robertson and Walker:

$$dr^2 = a^2(t)\left[\frac{dx^2}{1-\kappa x^2} + x^2 d\Omega^2\right]. \tag{1.8}$$

Here r is the 'proper' distance, $a(t)$ is the scale factor, related to the redshift z by $1+z = a_0/a$ (we choose the present-day value $a(t=0) = a_0 = 1$ for simplicity), κ is a curvature parameter (hereafter we take $\kappa = 0$, corresponding to spatial flatness), and x is the comoving distance, which expands with the universe. General relativity tells us that the energy density of a fluid, ρ', is related to the inertial mass density ρ and the fluid pressure p by

$$\rho' = \rho + \frac{3p}{c^2}. \tag{1.9}$$

We can understand the evolution of the scale factor using the Einstein field equations, which yield

$$\frac{\ddot{a}}{a} = -\frac{4\pi G}{3}\left(\rho + \frac{3p}{c^2}\right). \tag{1.10}$$

Consider the evolution of components whose pressure and density are related by the equation of state $p = w\rho c^2$, in particular:

1. non-relativistic matter; $w = 0$ and $\rho_m \propto a^{-3}$; for a universe dominated by non-relativistic matter,

$a(t) \propto t^{2/3}$,

2. radiation or highly relativistic matter; $w = 1/3$ and $\rho_\gamma \propto a^{-4}$; if radiation dominates the energy budget $a(t) \propto t^{1/2}$, and
3. a cosmological constant with $w = -1$ and $\rho_\Lambda = \text{const.}$ – in a Λ-dominated universe, $a(t)$ grows exponentially.

Integrating equation (1.10), we have the Friedmann equation,

$$H^2 = \left(\frac{\dot{a}}{a}\right)^2 = \frac{8\pi G}{3}\left(\rho + \frac{3p}{c^2}\right), \tag{1.11}$$

where H is the Hubble parameter. For a matter-dominated universe, the present-day matter density would be $3H_0^2/8\pi G$, a quantity known as the critical density. The quantities and relations described in this section will be useful as we address perturbations to a homogeneous universe.

1.2.2 Growth in the linear regime

Perturbations at some position $\mathbf{r}$ are described in terms of their fractional overdensity, δ, given by

$$\delta(\mathbf{r},t) = \frac{\rho(\mathbf{r},t) - \bar{\rho}(t)}{\bar{\rho}(t)}, \tag{1.12}$$

where ρ is the conventional mass density and $\bar{\rho}$ the mean density. In the matter-dominated era, the evolution of perturbations satisfying $\delta \ll 1$ on scales within the horizon can be determined by considering small perturbations to Newtonian fluid equations, namely those corresponding to the conservation of mass, the Euler equation of momentum balance, and the Poisson equation for the gravitational potential, Φ. For the general case of a collisional fluid, these equations are given in proper coordinates ($\nabla = \nabla_\mathbf{r}$) by

$$\frac{\partial \rho}{\partial t} + \nabla \cdot (\rho \mathbf{u}) = 0, \tag{1.13}$$

$$\frac{\partial \mathbf{u}}{\partial t} + (u \cdot \nabla)\mathbf{u} = -\frac{\nabla p}{\rho} - \nabla \Phi, \tag{1.14}$$

and

$$\nabla^2\Phi = 4\pi G\rho, \tag{1.15}$$

where $\mathbf{u}$ is the fluid velocity, and p is the pressure (for a homogeneous fluid, $\nabla p = 0$).

We introduce perturbations: $\rho(t) \to \bar{\rho}(t)[1+\delta(\mathbf{r},t)]$, and $p(t) \to \bar{p}(t) + \delta p(\mathbf{r},t)$. Using comoving coordinates, $\mathbf{x} = \mathbf{r}/a(t)$, and neglecting quadratic and higher order terms in the perturbed quantities and their derivatives, yields the linear theory perturbation equation:

$$\ddot{\delta} + 2\frac{\dot{a}}{a}\dot{\delta} = \frac{\nabla_{\mathbf{x}}^2 \delta p}{a^2\bar{\rho}} + 4\pi G\bar{\rho}\delta, \tag{1.16}$$

where $\nabla_{\mathbf{x}} = a\nabla_{\mathbf{r}}$, and the time derivatives of δ are to be understood to be calculated at fixed $\mathbf{x}$. Taking the Fourier transform of this equation, and writing $\delta p_{\mathbf{k}}/\bar{\rho} = v_s^2\delta_{\mathbf{k}}$, where v_s is the sound speed, we have:

$$\ddot{\delta}_{\mathbf{k}} + 2\frac{\dot{a}}{a}\dot{\delta}_{\mathbf{k}} + \left(\frac{v_s^2k^2}{a^2} - 4\pi G\bar{\rho}\right)\delta_{\mathbf{k}} = 0. \tag{1.17}$$

The fate of perturbations in various regimes can be deduced by substituting the relations between a and t from Section 1.2.1 into this expression. Post-reionization, when photons and baryons are decoupled, the sound speed is negligible and the solution to this equation is $\delta_{\mathbf{k}} = Aa + Ba^{-3/2} = A't^{2/3} + B't^{-1}$; the perturbations are able to grow. When the sound speed term dominates, however, $\delta_{\mathbf{k}}$ undergoes damped oscillations, and perturbations are prevented from growing on small scales. This is why, even after the transition from radiation to matter domination, baryon density fluctuations are unable to grow prior to decoupling from photons at recombination. Growth of structure thus starts with the dark matter. If a cosmological constant dominates the energy budget of the universe, there is no sound speed but the scale factor grows exponentially, and the growth of perturbations, at least in the linear regime, is suppressed.

Assuming statistical isotropy, the primordial power spectrum of dark matter fluctuations (introduced in Section 1.1.2) is related to the primordial $\delta_{\mathbf{k}}$ by

$$\langle\delta_{\mathbf{k}}\delta_{\mathbf{k}'}\rangle = (2\pi)^3\delta^3(\mathbf{k}-\mathbf{k}')P_{\mathrm{DM}}^{primordial}(k). \tag{1.18}$$

If we assume that linear theory remains valid, the dark matter power spectrum at some later epoch can be written as the product of $P_{\rm DM}^{primordial}$, the square of a transfer function, $T(k)$, which encapsulates the scale-dependent nature of equation (1.17), and the square of the linear growth factor, $D(z)$, which describes how the competing processes mentioned above shape the evolution of perturbations over time, and is normalised to unity today:

$$P_{\rm DM}^{linear}(k,z) = P_{\rm DM}^{linear}(k,0)\,D^2(z) = P_{\rm DM}^{linear}(k)T^2(k)D^2(z). \tag{1.19}$$

While perturbations do not actually remain linear (see below), this linear matter power spectrum remains useful for interpreting galaxy clustering measurements (Section 1.3).

1.2.3 Spherical collapse model

As perturbations in the matter-dominated era grow, eventually it is no longer valid to ignore higher order terms in equation (1.16), since δ is no longer much less than unity, and a general solution becomes intractable. Some insight can be gained from considering the behaviour of a spherically symmetric overdense region, which has average overdensity $\delta_i \ll 1$, and initial radius r_i at some early time t_i. If the universe is otherwise homogeneous, flat, and matter-dominated, the background density evolves as $\bar{\rho}(t) = \bar{\rho}(t_0)/a^3(t) = 1/6\pi G t^2$ (using relations from Section 1.2.1). The mass in our overdense sphere is constant, $M = \frac{4}{3}\pi(1+\delta_i)\bar{\rho}(t_i)\,r_i^3$. We solve Newton's second equation for the evolution of the radius of the overdense region, $r(t)$, which is given parametrically as $r = \frac{1}{2}r_{\rm max}(1-\cos\eta)$, with $t = \sqrt{\frac{r_{\rm max}^3}{8GM}}(\eta - \sin\eta)$, if we assume that $r(0) = 0$, and neglect the universe's brief period of radiation domination. At $\eta = \pi$, $r = r_{\rm max}$, and the overdensity reaches its maximum spatial extent; after this time (roughly, $t_{\rm max} \simeq 1.095\,t_i/\delta_i^{3/2}$), it begins to collapse under gravity, overcoming cosmic expansion. In our simple model, the overdensity will collapse to a singularity at $t = 2t_{\rm max}$; in reality, no perturbation is spherical, and the prevailing view of collapse is that the matter will undergo violent relaxation until it virializes. If we approximate the time of this virialization by the collapse time, $t_c = 2t_{\rm max}$, we can interpret the initial overdensity of the perturbation as the critical overdensity required for a perturbation to collapse by t_c:

$$\delta_c(t_i,t_c) \simeq 1.686\left(\frac{t_i}{t_c}\right)^{2/3}. \tag{1.20}$$

The key point from this simple analysis is that regions that will collapse at some late time may be crudely identified by finding perturbations in the density field at some early time (where everything is still in the linear regime) that possess overdensity above some threshold. The usefulness of this approach is increased by the fact that the constant 1.686 depends only weakly on background cosmology and other assumptions.

1.2.4 (Extended) Press-Schechter theory and the halo mass function

The Extended Press-Schechter formalism (EPS; see Press & Schechter, 1974, and subsequent work, e.g., Bond et al. 1991) deals with how properties of collapsed, highly non-linear regions or haloes (in particular their number density as a function of mass and redshift) may be estimated by studying the statistics of peaks in the primordial density field. This beautifully simple approach has shaped the development of large-scale structure theory; while current constraints on halo properties are inferred from intensive, N-body simulations, the good agreement between early simulations and the analytic PS theory was crucial in establishing the prevailing hierarchical or 'bottom up' view of structure formation outlined at the beginning of Section 1.2, and we briefly summarise the EPS approach below, following the notation used in Binney & Tremaine (2008).

We consider primordial density perturbations in some large box of volume V at initial time t_i, whose statistics are determined by a power spectrum $P(k) \propto k^{n_s}$, and wish to examine the statistics of peaks in this initial density field. We work with the sharp k-space filter, which sets to zero all Fourier amplitudes with $k > K$, and which has an associated characteristic mass scale, given by

$$M_K = 6\pi^2 \bar{\rho} / K^3, \tag{1.21}$$

where, as in Section 1.2.2, $\bar{\rho}$ is the mean density. We imagine constructing the density field by successively adding perturbations corresponding to shells of increasing wavelength in Fourier space, that is, adding quantities of the form

$$\Delta_K = \frac{1}{V} \sum_{K \leq |\mathbf{k}| < K+dK} \delta_{\mathbf{k}} e^{i\mathbf{k}\cdot\mathbf{x}} \tag{1.22}$$

to the density contrast, $\delta(\mathbf{x})$, at position $\mathbf{x}$. Each $\delta(\mathbf{x})$ undergoes a random walk as more shells are added.

If $\delta(\mathbf{x})$ first exceeds $\delta_c(t_i,t)$ upon adding Δ_K, we deduce that x is part of a region of scale K^{-1} that will collapse at time t. If $p_K(\delta)\mathrm{d}\delta$ is the probability that, at stage K, the overdensity at a random point lies in the interval $[\delta, \delta + \mathrm{d}\delta]$, it can be shown that p_K satisfies a diffusion equation,

$$\frac{\partial p_K}{\partial \sigma_K^2} = \frac{1}{2}\frac{\partial^2 p_K}{\partial \delta^2}, \tag{1.23}$$

where σ_K^2 is the variance of δ upon inclusion of stage K. This is the key part of EPS theory. Solving this equation and accounting for the fact that, for the primary halo mass function, $\mathrm{d}n/\mathrm{d}M$, defined as the comoving number density of haloes of mass M, we want to exclude objects of mass M that are contained within a more massive halo, yields

$$\frac{\mathrm{d}n}{\mathrm{d}M}(M,t) = \bar{\rho}\frac{\delta_c/\sigma_K}{(2\pi)^{1/2}}\exp\left(-\frac{\delta_c^2}{2\sigma_K^2}\right)\left|\frac{\mathrm{d}\ln\sigma_K^2}{\mathrm{d}\ln M_K}\right|, \tag{1.24}$$

where $\delta_c(t_i,t)$ is defined as in equation (1.19). A range of fitting functions – modifications to the above equation – inferred, as stated above, from N-body simulations, are typically used for high-precision calculations involving the halo mass function (e.g., Sheth & Tormen, 1999; Jenkins et al., 2001; Warren et al., 2006; Tinker et al., 2008). Simulations are also used to constrain the nonlinear dark matter power spectrum, $P_{\mathrm{DM}}^{nonlinear}$, which matches the linear power spectrum of equation (1.18) on large scales, but includes the non-linear collapse discussed above on small scales. For a standard, ΛCDM, cosmology, the halo mass function and nonlinear power spectrum are now believed to be known to a fairly high degree of both precision and accuracy (e.g., Smith et al., 2003; Warren et al., 2006; Tinker et al., 2008; Lawrence et al., 2010; Reed et al., 2012).

1.3 Galaxy clustering

The clustering of various galaxy populations has been observed for decades (Peebles, 1980, and references therein), and clustering of CIB sources was also therefore expected (e.g., Bond 1996, and references therein; Knox et al. 2001; Negrello et al. 2007), and has been detected in *Spitzer Space Telescope* data at 160 μm (Lagache et al., 2007), by the Balloon-borne Large-Aperture Submillimeter Telescope (BLAST) and *Herschel Space Observatory* at 250, 350 and 500 μm (Viero et al., 2009; Cooray et al., 2010; Amblard et al., 2011), in the microwave sky at around 150 and 220 GHz by SPT and ACT (Hall et al., 2010; Dunkley et al., 2011; Shirokoff et al., 2011), and in early data from *Planck* (Planck Collaboration et al., 2011c). Great improvements in the quality of data relating to the clustering of CIB sources has been made in recent years, and this is reflected in the wide range of model complexity discussed in the later chapters of this thesis.

While the nature of cold dark matter remains elusive, the fact that it interacts only gravitationally means its behaviour is actually easier to simulate and understand than that of the more familiar baryons, as mentioned earlier in this section. This fact is widely exploited in interpreting the properties, in particular the clustering properties, of luminous galaxy populations.

1.3.1 Linear biasing

The simplest way to relate a galaxy population to the underlying dark matter field is to assume that fluctuations in the galaxy density are linear tracers of those of the dark matter, meaning that, along some line-of-sight $\hat{\mathbf{n}}$, at redshift z, we can say

$$\delta_g(\chi\hat{\mathbf{n}},z) = b(z)\,\delta(\chi\hat{\mathbf{n}},z), \tag{1.25}$$

where δ_g is the galaxy overdensity, $\chi(z)$ is the comoving distance, and δ is the linear-theory matter overdensity introduced in Section 1.2. The total galaxy number fluctuation at position $\hat{\mathbf{n}}$ on the sky, $g(\hat{\mathbf{n}})$, is given by the line-of-sight integral of this quantity, weighted by the galaxy redshift distribution function, Π, which is normalised such that $\int dz\,\Pi(z) = 1$:

$$g(\hat{\mathbf{n}}) = \int dz\, b(z)\Pi(z)\delta(\chi\hat{\mathbf{n}},z). \tag{1.26}$$

The angular power spectrum of galaxy fluctuations is then written, like for the CMB fluctuations (equation 1.3), as

$$C_\ell = \frac{1}{4\pi}\int d\Omega d\Omega'\, P_\ell(\hat{\mathbf{n}}\cdot\hat{\mathbf{n}}')\,\langle g(\hat{\mathbf{n}})g(\hat{\mathbf{n}}')\rangle, \tag{1.27}$$

or as an integral over comoving wavenumber, k (see, e.g., Section 8.5 of Dodelson 2003, or Section 2.6 of Weinberg 2008),

$$C_\ell = \frac{2}{\pi} \int k^2\, dk\, P_{\rm DM}^{linear}(k, z=0) \left[\int dz\, b(z)\, \Pi(z)\, j_\ell(k\chi) D(z) \right]^2 , \tag{1.28}$$

where j_ℓ is the spherical Bessel function. The power spectra considered in this thesis are from relatively small areas of sky (covering at most hundreds of square degrees), and span $\ell \geq 80$. This allows us to apply the flat-sky (Limber) approximation (Limber, 1953; Peebles, 1980; Kaiser, 1992) to remove the integral over k, and one of the redshift integrals, since $(2/\pi) \int k^2 dk\, j_\ell(k\chi) j_\ell(k\chi') \to (1/\chi^2) \delta(\chi - \chi')$ for $\ell \gg 1$, where we have used the abbreviation $\chi' = \chi(z')$. The angular power spectrum of galaxy density fluctuations is then

$$C_\ell = \int dz \left[\frac{d\chi}{dz}(z) \right]^{-1} \frac{1}{\chi^2(z)} \Pi^2(z)\, b^2(z)\, P_{\rm DM}^{linear}(k, z) \bigg|_{k=(\ell+1/2)/\chi(z)} . \tag{1.29}$$

Since we are unable to resolve the majority of the CIB sources in the FIR and at longer wavelengths, we measure fluctuations not in galaxy density directly, but in CIB surface brightness. We replace the redshift distribution function Π with dI_ν/dz (sometimes called dS_ν/dz), the CIB intensity contribution from sources at redshift z in units of Jy sr^{-1}, and the angular power spectrum, in units of Jy^2 sr^{-1}, from correlating maps of unresolved CIB sources at frequency ν_1 and ν_2 becomes (Tegmark et al., 2002)

$$C_{\ell,\nu_1\nu_2} = \int dz \left[\frac{d\chi}{dz}(z) \right]^{-1} \frac{1}{\chi^2(z)} \frac{dI_{\nu_1}}{dz}(z) \frac{dI_{\nu_2}}{dz}(z)\, b^2(z)\, P_{\rm DM}^{linear}(k, z) \big|_{k=(\ell+1/2)/\chi(z)} . \tag{1.30}$$

Equation (1.30) is for the clustered anisotropy power, arising from the correlation of the image of a source in one map used for the correlation with images of different sources in the other map. There is also a Poissonian, shot-noise term, arising from the correlation of the image of a source in one map with its own counterpart in the other map (e.g., Peebles, 1980; Bond, 1996; Scott & White, 1999), which, as discussed in Section 1.1.5, can, for our purposes, be taken to be independent of angular scale. The Poisson contribution to the angular power spectrum is given simply by the product of a source's flux in one map with its flux in the other map, summed over all sources, and is discussed further in Chapters 3 and 5.

An alternative but equivalent expression for the clustered power is given, in terms of the comoving emissivity density, j_ν, rather than dI_ν/dz, by Haiman & Knox (2000) and Knox et al. (2001), and has subsequently been used in a number of CIB source models (e.g., Hall et al., 2010; Planck Collaboration et al., 2011c; Pénin et al., 2012, also see Chapter 5).

1.3.2 Nonlinear clustering and the halo model

In writing equation (1.30), several assumptions were made, including

(i) the fluctuations in CIB source number and dark matter density are related by a single factor, b, at each redshift, and

(ii) there is no correlation between a CIB source's flux and its bias (discussion of this issue is deferred until Chapters 4 and 5).

Given that the success of the EPS formalism, and subsequent constraints from N-body simulations, a popular strategy to treat small-scale galaxy clustering, where non-linearities become relevant, is to first associate the galaxies with collapsed dark matter haloes, and then utilise the (relatively) well-known halo properties, including the mass function, and the bias of haloes with respect to the dark matter, to bypass dealing with the non-linear galaxy bias directly. The general approach of using the dark matter haloes to understand large-scale structure is known as the halo model (e.g., Peacock & Smith 2000; Scoccimarro et al. 2001; Cooray & Sheth 2002; see also earlier work, e.g., Bond 1996 and references therein), while the prescription that tells us to how to occupy the haloes with galaxies is referred to as the halo occupation distribution (H.O.D.; e.g., Berlind & Weinberg, 2002; Cooray & Sheth, 2002; Kravtsov et al., 2004). This framework has been successfully applied to interpret the clustering properties of several source populations, including local galaxies from the SDSS, luminous red galaxies (LRGs), and high-redshift Lyman-break galaxies (e.g., Zehavi et al., 2004; Ouchi et al., 2005; Blake et al., 2008; Zheng et al., 2009; Zehavi et al., 2011). It has also been extensively used to model the CIB angular power spectrum in FIR, submm and microwave bands in recent years (e.g., Righi et al., 2008; Viero et al., 2009; Sehgal et al., 2010; Amblard et al., 2011; Planck Collaboration et al., 2011c; Shang et al., 2012; Xia et al., 2012; De Bernardis & Cooray, 2012).

A framework like the halo model allows us to interpret clustering measurements in regimes where the linear clustering ansatz (equation 1.25) breaks down. The ability to connect characteristic halo mass scales with different populations of galaxies (LRGs, quasars, CIB sources, and so on) is also highly desirable, since it allows us to probe the evolution of these populations – for instance, whether the evolution is driven by the merging of haloes (a prominent feature of many models of CIB source evolution, e.g., Righi et al., 2008; Engel et al., 2010), and any transition from one population to another (e.g., active star-forming galaxies becoming old and passive).

In the halo model, galaxy clustering is dominated on large scales by pairs of sources in different dark matter haloes (the 'two-halo' term – roughly corresponding to the linear clustering regime), while on small scales galaxy pairs occupying the same halo ('one-halo' term) become dominant. To write the galaxy angular power spectrum using this formalism, $b^2 P_{\rm DM}^{linear}$ in equation (1.30) is replaced by $P_{\rm gal}$, the three-dimensional galaxy power spectrum, which consists of the sum of the one- and two-halo terms. More details of the halo model treatment of CIB power spectra, and possible issues with its application in existing work, are discussed in Chapters 4 and 5.

1.4 The FIR–SFR connection and thermal dust emission

A galaxy's star formation rate (SFR) and FIR emission are known to be strongly connected (Kennicutt, 1998), due to absorption and thermal re-emission of starlight by dusty stellar birth clouds. A simple comparison of the energy in CIB photons with infrared emission from nearby galaxies indicates that FIR emission (and thus SFR) was considerably higher in the past (e.g., Hauser & Dwek, 2001, and references therein), and extensive measurements of FIR emission have been made in order to exploit the FIR–SFR connection and understand how SFR and stellar formation environments have evolved over cosmic time. A prevailing picture is that luminous and ultra luminous infrared galaxies (LIRGs and ULIRGs; $10^{11} < L_{\rm IR}/L_{\odot} < 10^{12}$ and $10^{12} < L_{\rm IR}/L_{\odot} < 10^{13}$, respectively, where $L_{\rm IR}$ is the integrated luminosity over $8 < \lambda/\mu{\rm m} < 1000$), which are rare in the local universe, become far more important to the global SFR at higher redshift (e.g., Le Floc'h et al., 2005; Pérez-González et al., 2005; Daddi et al., 2005; Caputi et al., 2007; Magnelli et al., 2011; Lapi et al., 2011). This trend has predominantly been probed using IR luminosity functions (LFs) measured using instruments including the *Infrared Astronomical Satellite*

(IRAS; Neugebauer et al., 1984), the *Infrared Space Observatory* (ISO; Kessler et al., 1996), the *Spitzer Space Telescope* (Werner et al., 2004) and, more recently, the *Herschel* Space Observatory (Pilbratt et al., 2010).

The nature of dust-enshrouded star formation beyond $z \sim 2-2.5$ is a key question in galaxy evolution. Does the relative importance of LIRGs and ULIRGs to the global IR luminosity and star formation rate density continue to increase? Where are stars forming at redshift three or four? How does the connection between FIR luminosity and environment (for instance, depth of local gravitational potential or host dark matter halo mass) evolve? In the remainder of this section, I discuss why these questions remain unanswered, and the role of the angular power spectrum of CIB fluctuations described above in addressing them.

1.4.1 The spectral energy distribution of dusty galaxies

The flux observed at frequency ν from a source at redshift z with bolometric luminosity L is given by

$$S_\nu(L,z) = \frac{L_{\nu(1+z)}}{4\pi(1+z)\chi^2(z)}, \tag{1.31}$$

where the differential luminosity, L_ν, is related to the bolometric luminosity L and the source spectral function, ϕ_ν, via

$$L_\nu = \frac{dL}{d\nu} = L\frac{\phi_\nu}{\int d\nu' \phi_{\nu'}}, \tag{1.32}$$

where, for IR emission, the integral in the denominator of the fraction is typically taken over the range 8 μm $< c/\nu <$ 1000 μm.

Ideally, a galaxy's dust emission would be treated using some sort of radiative transfer prescription, whereby the stellar population and kinematics could be directly connected to the dust properties and FIR emission. Current data limitations mean that such analysis is impossible in the redshift range $z \gtrsim 0.5$, where the majority of the FIR, submm and microwave CIB originates (although great improvements in our understanding of dust-enshrouded star formation are expected from the arcsecond-resolution imaging that will be available through the Atacama Large Millimeter/submillimeter Array – ALMA[c]). Conse-

---

[c] http://www.almaobservatory.org/

quently, a graybody function of the form $\phi_\nu \propto \nu^\beta B_\nu(T)$, where $B_\nu(T)$ is the blackbody Planck function, has been used extensively to model FIR galaxy SEDs, where the emissivity spectral index $\beta \sim 1-2$ is related to the emission properties of the dust grains (Hildebrand, 1983). In reality, we expect each individual galaxy to contain dust with a range of temperatures and emissivity indices. Even a sum of graybodies may not be a good approximation, since this form is only appropriate in the optically thin regime, and dust self-absorption may be significant in some systems, particularly at high redshift (e.g., Benford et al., 1999; Blain et al., 2003; Draine, 2006; Hayward et al., 2012). Many galaxies selected in FIR and submm surveys host AGN, in addition to, or instead of, significant star formation (e.g., Alexander et al., 2005; Lutz et al., 2005; Yan et al., 2005; Le Floc'h et al., 2007; Sajina et al., 2012). Emission from hot (equivalent graybody $T \gtrsim 100$ K) dust associated with the AGN torus dominates the SED at wavelengths shortwards of the thermal dust graybody peak. Due to this AGN contamination, and the range of dust temperatures and opacity, modifications to a single-T graybody Wien tail are required to fit the observed galaxy SEDs (Blain et al., 2003; Hayward et al., 2012, and references therein).

Graybody dust temperatures of FIR, submm and mm selected galaxies are typically in the range of 30–60 K (e.g., Benford et al., 1999; Dunne et al., 2000; Dunne & Eales, 2001; Chapman et al., 2005; Coppin et al., 2006; Chapin et al., 2011; Greve et al., 2012), although there is also evidence for cooler components, more similar to the diffuse cirrus emission of our own Milky Way, at 15–20 K, particularly at low redshift (e.g., Planck Collaboration et al., 2011b; Elbaz et al., 2011; Planck Collaboration, 2012). Figure 1.3 shows SED measurements from a sample of *Herschel* galaxies taken from Elbaz et al. (2011), featuring the characteristic peak from thermal dust emission.

1.4.2 Dust-enshrouded star formation at high redshift

Roughly speaking, a given observing frequency can probe thermal dust emission at temperature T and redshift z only if $T/(1+z)$ lies above some threshold. If the dust is colder, or a source more distant, the SED is observed beyond the graybody peak, and the observed flux rapidly decreases (at least in the absence of an obscured AGN). In fact, this threshold is not as strong a restriction as might be expected, because the rest-frame mid-infrared (MIR) emission is observed to be fairly tightly correlated with the the total IR luminosity (e.g., Caputi et al., 2007; Bavouzet et al., 2008; Elbaz et al., 2011), which allows

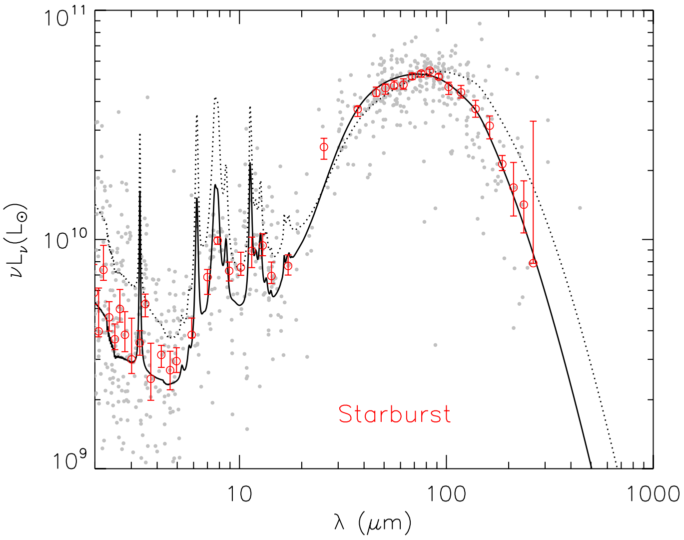

Figure 1.3: Composite SED for very actively star-forming galaxies at $0 \lesssim z \lesssim 2.5$ observed using *Herschel* in the GOODS field (taken from Elbaz et al., 2011). The grey dots are individual measurements, which are binned by (rest-frame) wavelength to give the red data points. The solid line shows an SED model fit, which consists of a thermal dust component (characterised by the broad peak) with an effective temperature $T \sim 40$ K, constructed from graybodies with a range of temperatures, $15 \lesssim T/\mathrm{K} \lesssim 50$, as well as the broadened line emission – predominantly from polycyclic aromatic hydrocarbons – that dominates at ~ 10 μm. The dotted line is a fit to a separate sample with lower MIR luminosity and lower star formation rate, shown normalised to the same bolometric infrared luminosity of 10^{11} $L_\odot$, which features dust with a somewhat cooler effective temperature of ~ 30 K.

(for instance) *Spitzer* to probe dust-enshrouded star-formation at $z \sim 2$, even though it only observes at $\lambda \leq 160$ μm. Nevertheless, probing the rest-frame thermal dust emission associated with star formation near its peak at $\lambda \sim 100$ μm at high redshift is desirable. The role of dust emission associated with AGN (see discussion above, and, e.g., Daddi et al., 2007a,b) is increasingly uncertain at $z \gtrsim 2$, and this, amongst other things, limits the reliable conversion from rest-frame MIR to total IR luminosity.

Unfortunately, resolving the CIB in the submillimeter and at longer wavelengths is increasingly hampered by source confusion, arising from the high number density of CIB sources per instrumental beam area (e.g., Dole et al., 2003; Béthermin et al., 2011). Resolved objects in maps at 250, 350 and 500 μm from *Herschel*'s Spectral and Photometric Imaging Receiver (SPIRE; Griffin et al., 2010) account for less than a fifth of the total CIB intensity (Oliver et al., 2010). Deeper constraints have been obtained with fits to the pixel flux histogram of highly-confused maps (the ‘P(D)’ approach; e.g., Scheuer, 1957; Condon, 1974; Patanchon et al., 2009; Glenn et al., 2010), although this method is unable to give us the positions of the faint sources required for follow-up observations. Stacking analyses, using observations (often from *Spitzer*) at lower wavelengths, have recovered most of the CIB shortward of $\sim 500\ \mu$m (e.g., Dole et al., 2006; Devlin et al., 2009; Marsden et al., 2009; Pascale et al., 2009; Béthermin et al., 2010, 2012b). The usefulness of this approach is limited by the fact that results are typically obtained only over small areas of the sky, and quantifying the uncertainties in the deepest counts is not straightforward. While submm-selected samples at longer wavelengths, observed using, for example, the Shared Common-User Bolometric Array (SCUBA; Holland et al., 1999) have demonstrated the importance of dust-obscured star formation at high-redshift (e.g., Smail et al., 1997; Hughes et al., 1998; Eales et al., 1999; Chapman et al., 2005; Coppin et al., 2006), our understanding is fundamentally limited if we have access to information about only the brightest objects in the population.

It is against this backdrop that the angular power spectrum of CIB fluctuations is emerging as a statistic to study dusty star formation at high redshift. The fluctuations in the CIB surface brightness are correlated across angular scales considerably larger than a beam, making source confusion largely irrelevant. Clearly, extracting information about the individual CIB sources at specific redshifts from the power spectrum alone is challenging, since the power spectrum receives contributions from all sources at all redshifts. Furthermore, to utilise the signal in the clustered power spectrum, we must be able to distinguish between the contribution from highly biased, intrinsically faint sources, and that from from less biased, intrinsically brighter objects. I show in Chapter 5, however, that the quality of power spectra from current experiments, especially *Planck* and *Herschel*, is good enough to lead to meaningful improvements in our understanding of dust emission at $z \geq 2.5$, when used in conjunction with deep *Spitzer* and SPIRE number count measurements. The angular power spectrum of CIB anisotropies can also be used to tell us about the nature of the haloes with which the CIB sources are associated (Amblard et al., 2011), and evolution in the SFR–environment relationship, via a framework like the halo model, described above (complementing other approaches discused by, e.g., Wang et al., 2012; Behroozi et al., 2012, and references therein), although investigating this is largely beyond the scope of this thesis.

It should be noted that the issue of source confusion would be alleviated if larger, higher resolution, submm telescopes could be built, but atmospheric absorption and the technical and financial challenges of deploying large telescopes in space have limited such possibilities. Observations from a ‘super *Herschel*’ space telescope, with, for example, a 20 m primary mirror, would overcome the problem of submm source confusion to a large extent, and allow us far easier access to dust-enshrouded star formation at redshift two and beyond.

1.5 Model fitting and Markov Chain Monte Carlo techniques

Constraining parametric models for various properties of the CIB sources is central to the work presented in Chapters 2, 3 and 5. In each case, the model fitting is performed using Markov Chain Monte Carlo (MCMC) analysis with the Metropolis-Hastings (e.g., Metropolis et al., 1953) sampling algorithm, using the step size and convergence criteria described by Dunkley et al. (2005). We outline the procedure below.

The posterior probability associated with a candidate model m, defined by a set of parameters with values θ, for the available data, d, is written, using Bayes' Theorem, as

$$P(\theta|d,m) \propto P(d|\theta,m)\,P(\theta|m), \tag{1.33}$$

where $P(d|\theta,m)$ is the likelihood, and $P(\theta|m)$ is the prior probability. We work with the negative log-likelihood, evaluated as (assuming Gaussian data uncertainties)

$$-2\ln\mathscr{L} = (\mathbf{M}(\theta)-\mathbf{D})^T \cdot \mathbf{C}^{-1} \cdot (\mathbf{M}(\theta)-\mathbf{D}), \tag{1.34}$$

where $\mathbf{D}$ is the vector of data points, $\mathbf{M}$ the corresponding vector of model predictions, and $\mathbf{C}$ is the covariance matrix of the data. The sampling of parameter space proceeds as follows:

(i) Generate new model parameters from values at current step using $\theta \to \theta + \Delta\theta$ for $\Delta\theta = \mathbf{L}' \cdot \mathbf{g}$, where $\mathbf{L}'$ is proportional to the Cholesky decomposition $\mathbf{L}$ of the estimated model parameter covariance matrix (the constant of proportionality is chosen based on the dimensionality; see Dunkley et al., 2005), and $\mathbf{g}$ is a vector of Gaussian random numbers with mean zero and standard deviation one.

(ii) Calculate the posterior probability for the new model parameters, including the contribution from the likelihood and model parameter priors.

(iii) If the new posterior probability is higher than that of the current parameters, always 'move' to the new point in parameter space and generate the next step from there; if it is lower, the probability of moving is given by the ratio of the posterior probabilities.

Marginalised parameter constraints can be obtained simply by calculating the mean and appropriate percentiles of lists of parameter values outputted during the chain. The results of the chain are also used to calculate an updated estimate of the model parameter covariance matrix, if needed.

The absolute goodness-of-fit of a model should, in a strictly Bayesian approach, be assessed using the evidence, $P(m|d)$, the integral of the posterior probability over all possible values of each model parameter. For a large parameter space, this calculation may be challenging, and, in the case of roughly Gaussian data uncertainties, an estimate of a model's goodness-of-fit is often made using a chi-squared test (a discussion of the validity of this approach is provided by, e.g., Marshall et al., 2006). The probability distribution function (p.d.f.) of the chi-squared distribution for ν degrees of freedom (d.o.f.) is

$$f_\nu(\chi^2) = \frac{(\chi^2)^{(\nu/2)-1}\, e^{-\chi^2/2}}{2^{\nu/2}\Gamma(\nu/2)}, \tag{1.35}$$

where Γ is the Gamma function. The minimum (best-fit) χ^2 is related to the maximum posterior probability (since $\chi^2 = -2\ln\mathscr{L} - 2\ln P(\theta|M)$), and we can associate a significance level to the extent that $\chi^2_{\rm min}$ deviates from the mean value of the chi-squared distribution, which is ν, by integrating equation (1.35).

The 'baseline' model fits presented in this work all have $\chi^2/\nu \simeq 1$ (this quantity is also called the reduced chi-squared), and the main use of the chi-squared test is to compare alternative models with different numbers of degrees of freedom. To do this, we use the fact that the p.d.f. of the difference $\Delta\chi^2$ between two chi-squared distributions with d.o.f. ν_1 and ν_2 itself follows a chi-squared distribution with $\nu = |\nu_1 - \nu_2|$. Taking the difference between the best χ^2 obtained for each model and integrating equation (1.35), we obtain the significance level at which one model is preferred over the other, which throughout this thesis is expressed as an equivalent Gaussian significance level (i.e., as a number of Gaussian standard deviations σ).

1.6 Calculating power spectra from small sky regions

This thesis largely deals with the interpretation of angular power spectrum measurements, however below we give a brief outline of how the spectra are actually calculated from maps covering small areas of the sky that may be considered flat (relevant for ACT data, and indeed all the spectra used in later chapters).

Let the temperature measured at position $\mathbf{x}$ on a two-dimensional pixelised sky map be $\tilde{T}(\mathbf{x})$. This quantity is related to the true sky temperature, $T(\mathbf{x})$, via

$$\tilde{T}(\mathbf{x}) = W(\mathbf{x}) \left[N(\mathbf{x}) + \sum_{\mathbf{x}'} b(\mathbf{x} - \mathbf{x}') T(\mathbf{x}') \right], \tag{1.36}$$

where b is the instrumental beam function, so that the summation over all pixels describes a convolution of the underlying temperature distribution with the beam, and $N(\mathbf{x})$ is the detector noise. The window function, $W(\mathbf{x})$, may contain information about the geometry of the map (for instance featuring a smooth transition from 0 to 1 near the map edges to prevent a sharp cut-off, which is undesirable when taking Fourier transforms), and the masking of particular regions (for instance, bright point sources). Taking the two-dimensional Fourier transform yields

$$\tilde{T}_{\boldsymbol{\ell}} = \sum_{\boldsymbol{\ell}'} W(\boldsymbol{\ell} - \boldsymbol{\ell}') \left[N_{\boldsymbol{\ell}'} + b_{\boldsymbol{\ell}'} T_{\boldsymbol{\ell}'} \right], \tag{1.37}$$

and the measured power spectrum, $\tilde{C}_\ell = \langle \tilde{T}_{\boldsymbol{\ell}} \cdot (\tilde{T}_{\boldsymbol{\ell}'})^* \rangle$, where the average is over coordinates satisfying $|\boldsymbol{\ell}|, |\boldsymbol{\ell}'| = \ell$, and we take $\tilde{T}_{\boldsymbol{\ell}}$ and $\tilde{T}_{\boldsymbol{\ell}'}$ from maps with independent noise properties, is then related to the underlying power spectrum we are interested in through a matrix equation (assuming statistical isotropy),

$$\tilde{C}_\ell = \sum_{\boldsymbol{\ell}'} |W(\boldsymbol{\ell} - \boldsymbol{\ell}')|^2 b_{\boldsymbol{\ell}'}^2 C_{\boldsymbol{\ell}'}. \tag{1.38}$$

The power spectra from inverting this equation are binned according to

$$C_b = \frac{\sum_\ell B_{b\ell} C_\ell}{\sum_\ell B_{b\ell}}, \tag{1.39}$$

where the binning weight function, B, is, in the simplest case, 1 for modes lying within each bin b, and

0 for modes outside. The angular size, s, of the map sets a fundamental frequency resolution in Fourier space – width of bandpower bins – $\delta\ell = 2\pi/s$, and a more coarse binning will often be used to reduce correlations between bins introduced by the window function, or if the data are particularly noisy; while the noise does not enter the expression for C_b for spectra calculated from maps with independent noise properties, it still contributes to the error on C_b (see further discussion in Chapter 2).

1.7 Thesis outline

The remainder of this thesis is structured as follows:

- Chapter 2 deals with the cross-correlation of maps from ACT and BLAST (calculation of power spectra and initial interpretation),
- in Chapter 3, I present a phenomenological template for CIB source clustered power as a foreground, for use in CMB temperature anisotropy analysis,
- Chapter 4 discusses modelling the spatial correlation of CIB sources with the tSZ effect, and
- Chapter 5 looks at the role of the angular power spectrum as a statistic to constrain the emission and clustering properties of the CIB sources.

Chapter 2

Correlations in the (sub)millimeter background with ACT and BLAST

2.1 Introduction

A range of signals contribute to mm-band microwave maps (Section 1.1.5), meaning that determining precisely the level at which unresolved dusty sources contaminate the CMB spectrum is not straightforward. Submillimeter (submm) maps, on the other hand, are dominated by the signal from dusty CIB galaxies (e.g., Devlin et al., 2009; Marsden et al., 2009; Pascale et al., 2009; Viero et al., 2009, hereafter V09). Provided there is a significant overlap in the dusty galaxies that contribute across this wavelength range, cross-frequency correlations of submm and mm maps may therefore allow us to isolate the contribution the CIB sources in the microwave sky.

Here we present the first such submm / mm cross-spectra. We use data at 1380 and 2030 μm (218 and 148 GHz) from the Atacama Cosmology Telescope (ACT; Fowler et al., 2007; Swetz et al., 2011), and at 250, 350, and 500μm (1200, 860, and 600 GHz) from the Balloon-borne Large Aperture Submillimeter Telescope (BLAST; Pascale et al., 2008), to measure both the Poisson and clustered dusty source contributions.

Throughout this thesis we use 'auto-spectrum' to refer to a power spectrum calculated by correlating two maps at the same frequency, and 'cross-spectrum' to refer to a spectrum calculated by cross-correlating maps at different frequencies. 'BLAST × ACT' is to be understood to refer to the BLAST / ACT cross-spectra, and so on.

This chapter is organized as follows: in Sections 2.2 and 2.3 we describe the data and techniques used to measure the power spectra. We present our results in Section 2.4, and interpret them using a linear clustering model in Section 2.5. Sections 2.6 and 2.7 contain a discussion and conclusions.

2.2 Instruments and observations

Below we describe the ACT and BLAST data used for the cross-correlation analysis, as well as the data used for estimating the Galactic cirrus power, which is the most significant contaminant in our analysis. While there are other significant signals in the microwave ACT maps (including the primary CMB, SZ, and radio sources), these are not expected to be strongly correlated with the dusty galaxy signal in the BLAST maps, and for the purposes of this work serve primarily to contribute noise to the cross-spectrum data points (see Appendix A).

2.2.1 ACT

ACT is a 6-meter off-axis Gregorian telescope (Fowler et al., 2007) situated at an elevation of 5190 meters on Cerro Toco in the Atacama desert of northern Chile. ACT has three frequency bands centered at 148 GHz (2.0 mm), 218 GHz (1.4 mm) and 277 GHz (1.1 mm), with angular resolutions of roughly $1\overset{\prime}{.}4$, $1\overset{\prime}{.}0$ and $0\overset{\prime}{.}9$, respectively (Hincks et al., 2010). The high-altitude site in the arid desert is excellent for mm observations due to low precipitable water vapour and stability of the atmosphere. The tropical location of ACT permits observations on both the northern and southern celestial hemispheres. Further details on the instrument are presented in Fowler et al. (2007), Swetz et al. (2011), and references therein[a].

The ACT maps used in this chapter are made from the 2008 observing season data (148 and 218 GHz only), and are identical to the maps used in Hajian et al. (2011) and Das et al. (2011a). The map projection used is cylindrical equal area (CEA), with $0.5'$ square pixels. The ACT data-set is divided into four equal subsets in time. These sub-maps each cover the same area and have similar depth but independent noise properties. The ACT maps have poorly measured modes on the largest angular scales,

---

[a] ACT Collaboration papers are archived at `http://www.physics.princeton.edu/act/`

largely due to atmospheric noise, and we filter them using a high-pass Fourier space filter, $F_c(\ell)$, which is a smooth sine-squared function:

$$F_c(\ell) = \begin{cases} 0 & : \quad \ell < \ell_{\rm min} \\ \sin^2 x(\ell) & : \quad \ell_{\rm min} < \ell < \ell_{\rm max} \\ 1 & : \quad \ell > \ell_{\rm max} \end{cases} \tag{2.1}$$

where $x(\ell) = (\pi/2)(\ell - \ell_{\rm min})/(\ell_{\rm max} - \ell_{\rm min})$. We choose $\ell_{\rm min} = 100$ and $\ell_{\rm max} = 500$, as in Fowler et al. (2010). The analyzed power spectra are corrected for this filter as well as for the effects of the beam and pixel window functions.

2.2.2 BLAST

BLAST flew from Antarctica for 11 days in December of 2006. Operating at ~ 40 km, above most of the atmosphere, BLAST observed in bands that are difficult or impossible to access from the ground. As a pathfinder for the SPIRE instrument (Griffin et al., 2003), it made observations at 250, 350 and 500 μm, of a number of Galactic and extragalactic targets. Its 1.8-m under-illuminated primary resulted in beams with FWHM of 36, 45 and 60 arcseconds. A more detailed description of the instrument is given by Pascale et al. (2008) and Truch et al. (2009)[b].

The BLAST field used in this study is an 8.6 deg^2 rectangle near the South Ecliptic Pole (SEP). Several BLAST and ACT maps of this region are shown in Figure 2.1. Further studies of the SEP field, including BLAST catalogs and ancillary 24 μm *Spitzer* maps, can be found in Valiante et al. (2010) and Scott et al. (2010).

The BLAST time-ordered data (TODs) are divided into four sets – covering the same region of the sky to the same depth – from which we make four sub-maps, as for the ACT data. The number of subsets is chosen to maximize the number of maps that can be made while maintaining uniformity in hits and providing as much cross-linking as possible. The maps are made with the iterative mapmaker, `SANEPIC` (Patanchon et al., 2009), resulting in a transfer function of unity on the scales of interest. The BLAST maps are made in tangent-plane projection (TAN), with $10''$ pixels. In order to cross-correlate with ACT,

---

[b] BLAST results and publications can be found at `http://blastexperiment.info/`

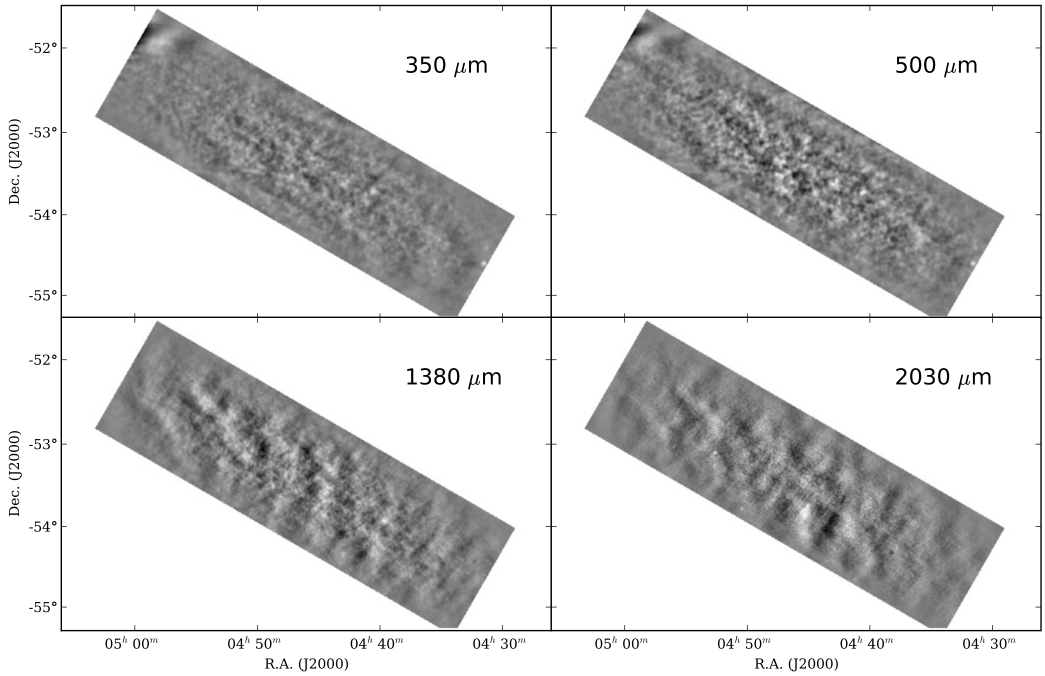

Figure 2.1: Four of the maps used in this analysis: BLAST maps at 350 and 500 μm (top panels), and ACT maps at 1380 and 2030 μm for the same region (bottom panels). Long wavelength modes in the ACT maps have been removed using the high-pass filter described in equation (2.1). All maps are multiplied by a taper to smooth the map edges, as discussed in Section 2.3.2.

the BLAST maps are re-binned to ACT resolution and reprojected to cylindrical equal-area projection (CEA) using `Montage`.[c]

2.2.3 IRIS

In the FIR and submm bands, the SED of Galactic cirrus is well-described by a graybody with $T \sim 15-20$ K and $\beta \sim 1.7-2$, peaking at $\lambda \sim 150$ μm (V09, Bracco et al., 2011). Bands closest to the peak, in our case the 250 μm BLAST band, are most susceptible to contamination.

To estimate the contribution from Galactic cirrus, we use three IRIS (Improved Reprocessing of the Infrared Astronomical Satellite – *IRAS* – Survey: Miville-Deschênes et al., 2005) HCON[d] maps at 100 μm. These maps are consistent with the Finkbeiner et al. (1999) maps used for estimating the Galactic cirrus in Das et al. (2011a), but are at a higher resolution. The IRIS power spectrum is measured for

---

[c] `http://montage.ipac.caltech.edu/`

[d] Each HCON – "Hours CONfirming" – map has independent noise properties. For more information, and publicly available maps, see `http://www.cita.utoronto.ca/~mamd/IRIS/`

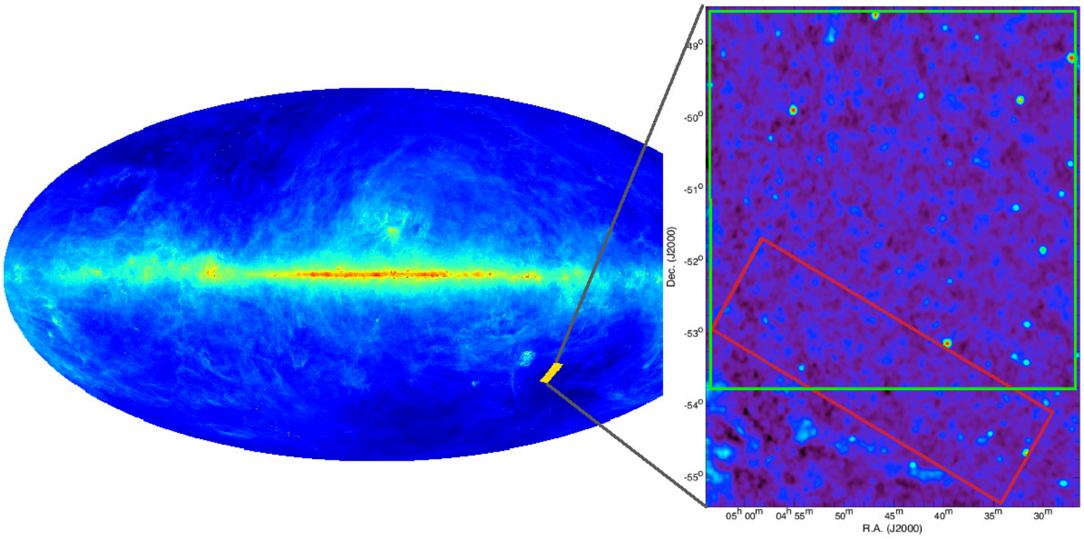

Figure 2.2: The full-sky IRIS map at 100 μm scaled logarithmically. The panel on the right shows the region around the South Ecliptic Pole used in this analysis, in CEA projection. The region clearly has low dust contamination. The red line shows the BLAST field that is used for cross-correlation with the ACT maps. The green square shows the 30 deg^2 region used for calculating the IRIS power spectrum and estimating the cirrus contribution to the BLAST and BLAST × ACT power spectra.

a 30 deg^2 field surrounding the SEP (see Figure 2.2). The power spectrum of the Galactic cirrus is computed from the average cross-spectrum of these three maps, and is corrected with a window function to account for IRAS's 4.3$'$ beam.

2.3 Measuring auto- and cross-frequency power spectra

We examine four distinct sets of power spectra: the BLAST auto-spectra, the BLAST cross-spectra, the BLAST × ACT cross-spectra, and the 100 μm IRIS auto-spectrum. Details of our power spectrum method are given below. Note that different unit conventions exist in submillimeter and microwave astronomy, and we present power spectrum results as both $P(k_\theta)$ and C_ℓ (see Appendix B).

2.3.1 Power Spectrum Method

All power spectra are computed using cross-correlations of pairs of sub-maps (described in Sections 2.2.1 and 2.2.2), since the noise in different sub-maps is uncorrelated (independent) and thus averages to zero in the cross-spectra. The power spectrum methods used in this paper closely follow those used for cross-correlating ACT and *WMAP* in Hajian et al. (2011).

The BLAST auto-spectra are computed using the average of the six cross-correlations from the four BLAST sub-maps in each band, such that

$$C_\ell = \frac{1}{6} \sum_{\alpha,\beta;\alpha<\beta}^{1\leq\beta\leq 4} C_\ell^{\alpha\beta}, \tag{2.2}$$

where α and β index the four sub-maps.

Since the noise in maps from different bands is uncorrelated, we co-add the sub-maps for each frequency before computing the BLAST × BLAST and BLAST × ACT cross-spectra. Several components contribute to the cross-spectrum uncertainties. An analytic approach to computing the uncertainties is described in Appendix A.

2.3.2 Weights and Masks

We use a flat-sky approximation for computing the power spectra, which are measured from Fourier transforms of the maps as outlined in Section 1.6. We adopt several techniques developed in Hajian et al. (2011) in order to isolate and remove or down-weight instrumental and systematic noise. This is done in two stages, in real space and in Fourier space, before the final one-dimensional angular power spectra are calculated.

We use the Slepian taper described in Das et al. (2009) to apodize the sharp edges of the ACT and BLAST maps. The gradual fall-off of this taper at the edges reduces the mode-mode coupling in the measured power spectrum. Any residual mode coupling caused by this weighting is corrected in the end by deconvolving the window function (i.e., the power spectrum of the taper function) from the measured power spectrum using the algorithm described in Hivon et al. (2002) and Das et al. (2009).

Anisotropic power in Fourier space is caused by noise and is optimally dealt with using inverse noise weighting. This is done by dividing the two-dimensional spectrum by our best estimate of the two-dimensional noise power spectrum for each map. At each frequency band, the noise spectrum is estimated from the difference between the mean two-dimensional auto- and cross-spectra for each pair of maps, as described in Hajian et al. (2011). For every cross-correlation, noise weights are computed from the inverse of the square root of the product of the two noise power spectra corresponding to the two frequency bands.

In order to be consistent with the V09 BLAST analysis, we mask all point sources that have a flux greater than 0.5 Jy in the BLAST 250 μm map (six sources), before computing the BLAST power spectra. For the BLAST / ACT cross-correlations, we instead mask just the brightest source in the BLAST maps, which happens to be a local spiral galaxy. Masking more point sources, down to the BLAST resolution limit, has no effect on the cross-spectra. We also mask the known radio galaxies (Marriage et al., 2011b) in the ACT 2030 μm map to reduce the uncertainties in the cross-spectra (see Appendix A).

2.3.3 Estimating Galactic cirrus emission

Spectra from the 100 μm IRIS maps contain three contributions – diffuse Galactic emission (cirrus), as well as the Poisson and clustered dusty CIB sources. For the purposes of this work, we are only interested in measuring the IRIS cirrus power spectrum in order to subtract it from the BLAST and BLAST × ACT spectra. Our analysis is limited to the 30 deg^2 area around the SEP (shown in Figure 2.2), since the amplitude of the cirrus power spectrum is known to vary strongly with position on the sky (e.g., Miville-Deschênes et al., 2005). To minimise the impact of bright galaxies in the IRIS map, we mask sources with $S_{100\ \mu\mathrm{m}} > 1$ Jy. The power spectrum is computed from the mean of the three cross-spectra from the three HCON maps (using one taper at resolution 1; see Das, Hajian, & Spergel, 2009, for details).

Miville-Deschênes et al. (2007) show that the power spectrum of Galactic cirrus can be approximated by a power-law,

$$P_{\mathrm{cirrus}}(k_\theta) = P_0 \left(\frac{k_\theta}{k_0} \right)^{\alpha}, \tag{2.3}$$

where k_θ is the angular wavenumber in inverse arcminutes, and P_0 is the power spectrum value at $k_0 \equiv$ 0.01 arcmin^{-1}.

We attempt to fit the data in two ways, in both cases fixing the slope of the cirrus power spectrum at $\alpha = -2.7$ (adopting the properties of region 5 from Bracco et al., 2011, whose mean flux density most resembles the SEP). The first is a two-parameter fit, where the free variables are the Poisson level and the amplitude of the cirrus power. For this we find $P_0 = (0.47 \pm 0.06) \times 10^6$ Jy^2 sr^{-1} and $\chi^2 = 21.9$ (for 29 degrees of freedom). The measured power spectrum is shown in the left panel of Figure 2.3. The power spectrum uncertainties are calculated in a manner analogous to that described in Appendix A.

The second fitting procedure uses a three-parameter fit in which the free variables are the Poisson level, cirrus amplitude and clustering amplitude of the DSFGs. The shape of the clustering component is simply that of a linear dark matter spectrum. In this case we find cirrus values $P_0 = (0.19 \pm 0.15) \times 10^6$ Jy^2 sr^{-1} and a clustering amplitude of $\sim 720\,\mathrm{Jy}^2$ sr^{-1} at $\ell = 3000$, with $\chi^2 = 18.1$ (dof $= 28$).

The two approaches yield consistent Poisson levels, but the fit with a clustered component appears to describe the data better, with $\Delta\chi^2 = 3.8$. Future studies with *Herschel*'s Photodetector Array and Camera (PACS; Poglitsch et al., 2010) should be able to measure the clustered signal to higher significance at 100 μm.

The cirrus power spectrum is estimated at the ACT and BLAST bands from the fit to the IRIS spectrum including the clustered power using the average dust emission colour $(I_{(\mathrm{sub})\mathrm{mm}}/I_{100})^2$ from model 8 of Finkbeiner et al. (1999).

We could instead have directly cross-correlated the IRIS and BLAST or ACT maps to estimate the cirrus power. We adopted the treatment described here because the BLAST and ACT maps cover a smaller area than the IRIS maps, meaning that the large-scale power, where the cirrus is dominant, is not as well-constrained in the IRIS × BLAST or ACT cross-spectra as in the IRIS auto-spectrum, which would hamper separation of the CIB and cirrus contributions.

2.4 Power spectrum results

The BLAST auto- and cross-spectra spectra and BLAST × ACT cross-spectra are shown in Figure 2.4. Raw data are shown as squares, while cirrus-subtracted points are shown as crosses with error bars. The Galactic cirrus spectra, extrapolated to our bands as described above, are shown as dashed lines in the bottom left corner of each panel (when strong enough to appear at all). Cirrus appears to have a nearly negligible effect on the power in most bands, with only a marginal contribution in the 250 μm auto-spectrum. Note that the cirrus contribution in V09 to the BLAST bands was extrapolated from 100 μm incorrectly, however, properly accounting for cirrus ultimately has little impact on our results.

The figure shows a clear cross-correlation between ACT and BLAST. There is both a significant

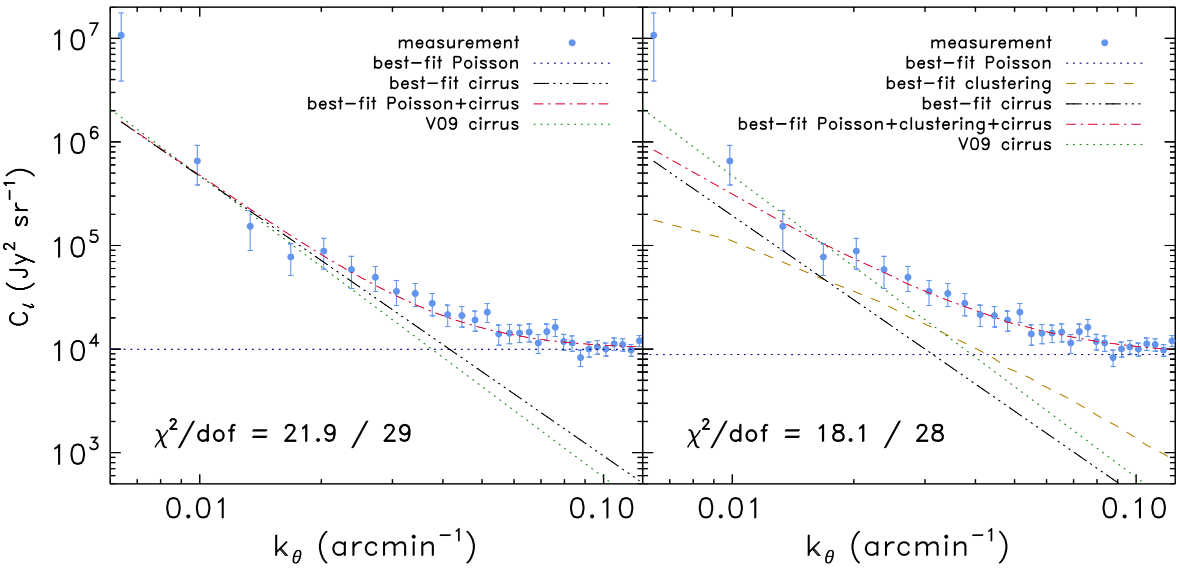

Figure 2.3: Power spectrum of the 30 deg^2 region surrounding the SEP from the 100 μm IRIS maps. A three-component fit (right panel), including a clustering term (dashed yellow line) provides a better description of the measured power spectrum than fitting just Poisson and cirrus alone (left panel), although the difference is not highly significant.

Poisson term (horizontal line) and clustering term (rising to low k_θ). This is the main result of this chapter: the unresolved BLAST background made up of dusty sources is indeed intimately related to the ACT unresolved point source background. The signal is clearest in the ACT 1380 μm correlation with the BLAST 500 and 350 μm bands, and less significant in the ACT 1380 and 2030 μm correlation with the BLAST 250 μm band.

2.5 Linear clustering model

In this section we estimate the CIB source Poisson power levels, and fit the clustered component using a simple linear model similar to that of Lagache et al. (2007), V09 and Hall et al. (2010). More extensive modelling, allowing for non-linear clustering, is described in Chapters 3 and 5. We assume here that the CIB source power spectrum is related to the linear dark matter power spectrum through a bias parameter,

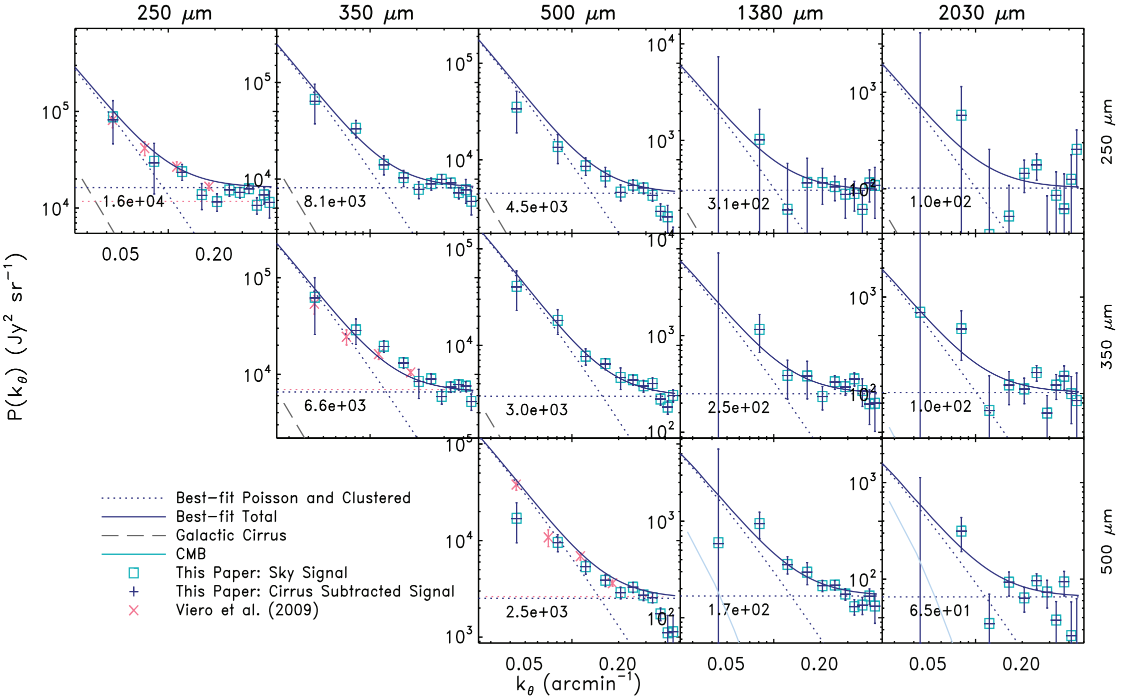

Figure 2.4: BLAST × BLAST (250–500 μm) and BLAST × ACT (1380–2030 μm) power spectra with 1σ errorbars. Squares and crosses are the data before and after cirrus removal. Red crosses and red horizontal dotted lines are power spectra and Poisson noise levels from V09. The horizontal and sloped dotted lines are the best-fit Poisson and linear clustering terms, respectively (see Section 2.5). Note that the vertical scale is different for each panel. The error bars are described in Appendix A.

$b(z)$, as described in Section 1.3.1:

$$P_{\rm gal}(k,z) = b^2(z)\, P_{\rm DM}^{linear}(k,z), \tag{2.4}$$

so that the angular power spectrum, $P^{\rm C}_{\nu_1\nu_2}(k_\theta)$, of clustered CIB sources can be written as (equation 1.30; Bond et al., 1991a; Tegmark et al., 2002)

$$P^{\rm C}_{\nu_1\nu_2}(k_\theta) = \int dz \left[\frac{dV_{\rm c}}{dz}(z)\right]^{-1} \frac{dI_{\nu_1}}{dz}(z)\frac{dI_{\nu_2}}{dz}(z)\, P_{\rm gal}(k,z)\big|_{k=\frac{2\pi k_\theta}{\chi(z)}}, \tag{2.5}$$

where $\chi(z)$ is the comoving distance, $dV_{\rm c}/dz = \chi^2 d\chi/dz$ is the comoving volume element, and dI_ν/dz is the contribution to the intensity from sources at redshift z.

We adopt dI_ν/dz from the source model of Béthermin et al. (2011; hereafter B11). Figure 2.5

shows plots of dI_ν/dz at 250 and 2030 μm for ten randomly chosen realizations provided by the B11 distribution[e]. We adopt the concordance model, a flat ΛCDM cosmology with $\Omega_{\rm M} = 0.274$, $\Omega_\Lambda = 0.726$, $H_0 = 70.5$ km s^{-1} Mpc^{-1}, and $\sigma_8 = 0.81$ (Hinshaw et al., 2009).

The linear dark matter power spectrum is calculated as described in Section 1.2.2; we adopt the fitting function for the matter transfer function $T(k)$ given by Eisenstein & Hu (1998). We treat the magnitude of the Poisson component of each of the 12 power spectra as a free parameter rather than simultaneously using the B11 model to predict the Poisson level as well as the clustering power, motivated by the fact that the B11 model does not reproduce the Poisson power equally well across the frequency range considered (see discussion in Section 2.5.1, below).

2.5.1 Estimating the bias

In principle the bias, b, is a function of scale and redshift, as well as environmental factors such as the host halo mass for the CIB sources. Here, we adopt a simple, redshift-dependent, bias of the form (Bond, Carr, & Hogan, 1991a; Hui & Parfrey, 2008)

$$b(z) = 1 + (b_0 - 1)\frac{D(z_0)}{D(z)}, \tag{2.6}$$

where $D(z)$ is the linear growth function and b_0 is an initial bias at some formation redshift, z_0. This parametrization assumes that DSFGs are members of a single population, which formed at the same epoch (z_0) and under the same conditions.

Our parameter space consists of the 12 Poisson levels plus b_0 and z_0. We find that moderate changes in z_0 (in the range $6 < z_0 < 10$) have virtually no effect on the quality of the fit or best-fit $b(z)$, and also find that b_0 and z_0 are almost degenerate. We consequently fix $z_0 = 8$, and explore the remaining 13-parameter space using a Markov Chain Monte Carlo (MCMC) method, as described in Section 1.5, with uniform priors on each parameter. We fit the BLAST × ACT data only in the range $\ell \geq 1200$ ($k_\theta \geq 0.04$ arcmin^{-1}), because the first data point in each of these spectra is extremely noisy and so will artificially improve the goodness-of-fit without meaningfully improving constraints.

We find a best-fit $\chi^2 = 107$ for 101 degrees of freedom (indicating a good quality of fit), with $b_0 =$

---

[e] `http://www.ias.u-psud.fr/irgalaxies/model.php`

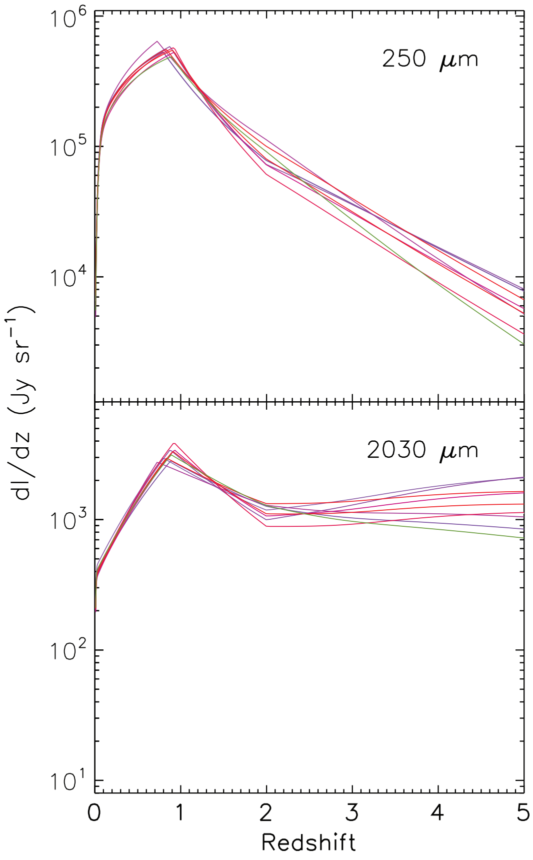

Figure 2.5: Redshift distributions of intensity, dI_ν/dz, at 250 and 2030 μm, for ten randomly chosen realizations of the B11 source model. In this model, the emission peaks around $z = 1$ for the whole range of wavelengths covered by ACT and BLAST, but there are significant contributions to the CIB flux from $z \gtrsim 2$ at mm wavelengths.

$18.2^{+2.3}_{-1.7}$, which corresponds to $b(z=1) = 5.0^{+0.6}_{-0.4}$ and $b(z=2) = 6.8^{+0.8}_{-0.5}$. This Poisson plus clustering model is preferred to the null case with no BLAST × ACT correlation at over 25σ. The best-fit clustering and Poisson levels are plotted as blue dotted lines in Figs. 2.4.

We also try fitting just the BLAST × ACT data with no clustering power. In this case we obtain a best-fit $\chi^2 = 64.3$ with 48 degrees of freedom. After adding linear clustering to the model, we find $\chi^2 = 43.6$ with 47 degrees of freedom, corresponding to $\Delta\chi^2$ of 20.7 (with one fewer degree of freedom), so that the model including clustering is preferred to one with only Poisson and cirrus at greater than 4σ.

Lastly, we try fitting a single-value bias, independent of redshift, to the entire range of power spectra. We find a best-fit single-value bias of 5.0 ± 0.4 with $\chi^2 = 110.8$ for 101 degrees of freedom; worse than a redshift-dependent bias by $\Delta\chi^2 = 3.8$. The single-value bias thus still provides a good fit to the BLAST × ACT data, however when we include the measured 2030 μm (148 GHz) and 1380 μm (218 GHz) clustered power measurements from Dunkley et al. (2011) in the likelihood calculation, we find the redshift-dependent bias is preferred at $\sim 2\sigma$. The ACT clustering measurements are reproduced well with the redshift-dependent bias, but under-predicted with the single-value bias.

Figure 2.6 shows $b(z)$ calculated using equation 2.6 for three representative realizations of the B11 model. The bias appears high compared to the linear bias estimates in V09 (who adopted the Lagache et al., 2004, model), although given the spread in $b(z)$ from different realizations of the B11 model, it is not clear that the measurements are inconsistent.

Our choice of source model may be affecting $b(z)$. The B11 model contains two distinct classes of IR sources, "normal" and "starburst," with substantially different luminosities, which is not accounted for in our $b(z)$ parametrization. Also, the B11 model does not match observational constraints equally well across the whole wavelength range probed by ACT and BLAST; for instance it under-predicts Poisson power and number counts compared to BLAST and SPT measurements at 500 and 1360 μm (see Section 5.6 of B11). An under-prediction of dI_ν/dz would result in a higher bias to compensate.

Additionally, our $b(z)$ constraint is likely affected by the fact that our simple model does not account for non-linear clustered power; the fact that linear-only clustered power is capable of providing a good to fit is probably an indication of the fact that the data considered lack the constraining power required to distinguish the linear and non-linear contributions (see Chapter 3).

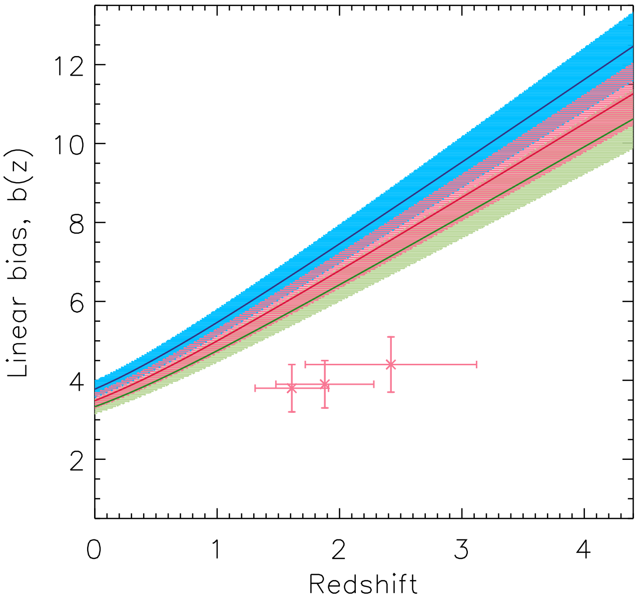

Figure 2.6: Best-fit redshift-dependent linear bias $b(z)$ for three realizations of the B11 model with 1σ error bounds estimated from our MCMC analysis. Also shown are the single-value linear biases found by V09 for the BLAST 250, 350, and 500 μm auto-spectra, plotted at median redshifts $z = 1.61$, 1.88, and 2.42, respectively.

2.6 Discussion

The Poisson and clustered power amplitudes are plotted as a function of effective wavelength, defined as $\lambda_{\rm eff} = \sqrt{\lambda_1 \lambda_2}$, in Figure 2.7. Also included are measurements made by the following experiments: *AKARI* at 90 μm (Matsuura et al., 2011); *Spitzer* at 160 μm (Lagache et al., 2007); BLAST at 250, 350, and 500 μm (Viero et al., 2009); ACT at 1380, 1673, and 2030 μm (Dunkley et al., 2011); SPT at 1363, 1629, and 1947 μm (Hall et al., 2010); and the measured Far Infrared Absolute Spectrophotometer (FIRAS; Fixsen et al., 1998) graybody, with $T = 18.5$ and $\beta = 0.64$, which is shown as a dotted line.

The degree of correlation between widely spaced wavelengths is of interest both for determining the redshift distribution of sources, and for modelling the CIB source power as a CMB contaminant. To assess the correlation, the geometric means at each effective cross-band wavelength, defined as $\sqrt{C_{\ell,\lambda_1} \cdot C_{\ell,\lambda_2}}$, are shown as a downward pointing arrows. Since we do not measure $C_{\ell,\lambda}$ at $\lambda = 1380$ and $2030\,\mu$m, we rely on measurements by Dunkley et al. (2011) for those bands when calculating the geometric means. The ratios of the measurements to the geometric means, $C_{\ell,\lambda_1\lambda_2}/(C_{\ell,\lambda_1} \cdot C_{\ell,\lambda_2})^{1/2}$, then represent the levels of cross-correlation between bands. Correlation is seen between all the frequencies, and does not fall significantly as a function of increased band separation, suggesting significant overlap in the source redshift distributions. This behaviour is consistent with the findings of Hall et al. (2010) and Dunkley et al. (2011) that the $1000-2000\ \mu$m bands are correlated at close to the 100% level, and extends the range of wavelengths probed.

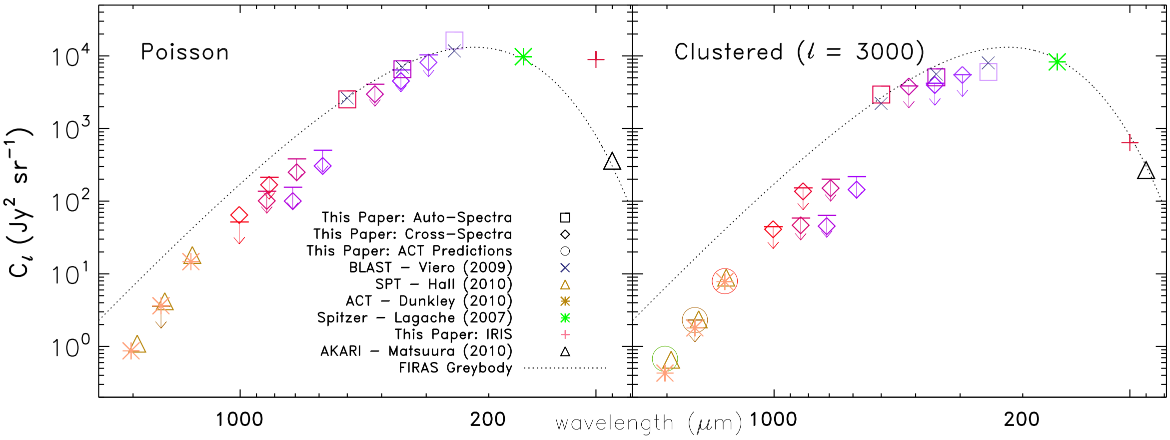

Figure 2.7: C_ℓ versus wavelength for observations and models. From left to right, the actual or effective wavelengths, $\lambda_{\rm eff} = \sqrt{\lambda_1\,\lambda_2}$, (in μm) are: 2030, 1673, 1380, 1007, 843, 831, 712, 695, 587, 500, 418, 354, 350, 296, 250, 160, 100, and 90. Best-fit Poisson (left panel) and clustered (at $\ell = 3000$, right panel) C_ℓ from measurements are shown as squares (auto-spectra) and diamonds (cross-spectra), respectively, and our measurement of IRIS galaxies are shown as red crosses. Open circles represent the prediction for the clustered power at the ACT wavelengths from the best-fit, redshift-dependent bias model. Uncertainties are omitted for visual clarity, but are generally smaller than the size of the symbols due to the large dynamic range in C_ℓ. The geometric mean of the cross-band spectra, defined as $\sqrt{C_{\ell,\lambda_1}\cdot C_{\ell,\lambda_2}}$, are shown as downward-pointing arrows. Measurements from other experiments are: ACT (Dunkley et al., 2011, yellow asterisks); BLAST (Viero et al., 2009, blue exes); *Spitzer* (Lagache et al., 2007, green asterisk); SPT (Hall et al., 2010, yellow triangles); *AKARI* (Matsuura et al., 2011, black triangle). The FIRAS modified blackbody ($T = 18.5, \beta = 0.64$) is plotted as a dotted line. As was found by Hall et al. (2010, Figure 5), FIRAS describes the data short of $500\,\mu$m, but over-predicts the measurements at millimeter wavelengths. The ratio of the measurement (diamonds) to the geometric mean (downward-pointing arrows) represents the level of cross-correlation between bands.

2.7 Conclusion

We have presented measurements of the cross-correlations of BLAST (250, 350 and $500\,\mu$m) and ACT (1380 and $2030\,\mu$m) maps. We find significant levels of correlation between the two sets of maps, indicating that the same CIB sources that produce the angular fluctuations in the BLAST maps are also present in the ACT maps. Furthermore, we confirm previous BLAST analysis (Viero et al., 2009) for a different field and with an independent pipeline, and extend the analysis by including BLAST × BLAST cross-frequency correlations.

We fit Poisson and clustered terms in each spectrum simultaneously using a MCMC analysis, adopting a model for the sources (Béthermin et al., 2011), and assuming a parametrized form for the z-dependent bias. Using this model, we detect a clustered signal at at a significance level of over 4σ, in addition to a Poisson component.

Though we find convincing evidence for correlated Poisson and clustered power from dusty CIB sources, the levels of precision needed to robustly remove these signals from CMB power spectra demand better measurements still. This is particularly true of the clustering term, whose contribution to the power spectrum in $\ell(\ell+1)C_\ell$ peaks at a similar region in ℓ-space to that typically targeted in searches for the SZ power spectrum (e.g., Dunkley et al., 2011). Future studies, combining *Herschel*-SPIRE data with ACT, SPT, and *Planck*, are needed to solidify this much-needed measurement (see Chapters 3 and 5).

Appendix A: power spectrum uncertainties

The BLAST × ACT cross-spectrum variance for bandpower b can be written as the sum of three terms (Fowler et al., 2010):

$$\sigma^2(C_b^{B\times A}) = \frac{2}{n_b}\left(C_b^{B\times A}\right)^2 + \frac{C_b^{B\times A}(N_b^B + N_b^{A,\mathrm{eff}}) + N_b^B N_b^{A,\mathrm{eff}}}{n_b} + \frac{\sigma_P^2}{f_{\mathrm{sky}}}. \tag{2.7}$$

Here, the superscripts A and B label the ACT and BLAST maps, n_b is the number of Fourier modes measured in bin b (i.e., the number of pixels falling in the appropriate annulus of Fourier space), f_{sky} is the patch area divided by the full-sky solid angle, and $C_b^{B\times A}$ is the binned cross-spectrum. The first term arises from sample variance due to limited sky coverage. The second term is from noise in the individual maps. For the purposes of this analysis, the effective ACT noise power spectrum, $N_b^{A,\mathrm{eff}}$, is actually the sum of the instrumental and atmospheric noise spectrum, N_b^A, as well as the contribution from signals that do not correlate strongly with the CIB sources in the BLAST maps:

$$N_b^{A,\mathrm{eff}} = N_b^{\mathrm{A}} + C_b^{\mathrm{CMB}} + C_b^{\mathrm{RG}}, \tag{2.8}$$

where C_b^{CMB} and C_b^{RG} are the power spectra of the primary and secondary CMB anisotropies, and radio galaxies, respectively. The third term in equation (2.7) arises from the distribution of discrete unresolved objects the map (e.g., galaxies or galaxy clusters). This contribution is essentially a measure of how unrepresentative the finite sample of such objects lying in this particular field may be of the global average; σ_P^2 is given by the non-Gaussian part of the four-point function of the map (equation 10 of Fowler et al., 2010). For this analysis, as in Fowler et al. (2010), this term is subdominant to the noise term over the range of angular scales probed.

The uncertainties on the BLAST × BLAST power spectra are computed using a similar analytic estimate, using equation (9) of Fowler et al. (2010) with $n_w = 6$ cross-spectra per map.

We compare our analytic estimate of the error bars with the standard deviation of the power spectra computed from different regions (patches) of the map. We divide the data into four patches of equal area and with them compute four independent cross-power spectra. We use the variance of the measurements of each bandpower bin as a measure of the error on the power spectrum. This method agrees well with the analytic estimate of the errors, however, due to the small area of the sky used in this analysis, both analytic and patch-variance estimates of the error bars are, themselves, somewhat uncertain. Thus, we conservatively use the greater of the analytic and patch-to-patch variances as an estimate of the uncertainty on the power spectrum bandpowers.

We ignore all off-diagonal, bin-to-bin correlations in this analysis; a combination of the noise term being dominant and the coarse ℓ-binning mean these contributions are negligible (as in Das et al., 2011a).

Appendix B: unit conversion

The flux density unit conventionally used in infrared, submillimeter, and radio astronomy is the Jansky, defined as

$$\mathrm{Jy} = 10^{-26}\frac{\mathrm{W}}{\mathrm{m^2\ Hz}}, \tag{2.9}$$

and is obtained by integrating over the solid angle of the source. Surface brightness is given in Jy sr^{-1}, and the angular power spectrum then has units of $\mathrm{Jy}^2\ \mathrm{sr}^{-1}$.

When dealing with microwave CMB data, the signal is conventionally reported as δT_{CMB}, the deviation from the 2.725 K blackbody. We convert from δT_{CMB} in μK to Jy sr^{-1} at frequency ν using (e.g., Fixsen, 2009):

$$\begin{aligned} \delta T_\nu &= \left(\frac{\delta B_\nu}{\delta T}\right)\delta B_\nu, && (2.10)\\ \text{where } \frac{\delta B_\nu}{\delta T} &= \frac{2k}{c^2}\left(\frac{kT_{\mathrm{CMB}}}{h}\right)^2\frac{x^2e^x}{(e^x-1)^2} = \frac{98.91\ \mathrm{Jy\ sr^{-1}}}{\mu\mathrm{K}}\frac{x^2e^x}{(e^x-1)^2}, && (2.11)\\ \text{and}\quad x &= \frac{h\nu}{k_\nu T_{\mathrm{CMB}}} = \frac{\nu}{56.79\ \mathrm{GHz}}, && (2.12) \end{aligned}$$

Lastly, the CMB power spectrum is conventionally reported as a function of multipole ℓ, while in the submillimeter the convention is to report the power spectrum as a function of angular wavenumber, k_θ, typically with units of arcmin^{-1}. In the small-angle approximation the two are related by $\ell = 2\pi k_\theta$ (so that $k_\theta/\mathrm{arcmin}^{-1} = \ell/21600$).

Chapter 3

Power-law template for CIB point source clustering

3.1 Introduction

In this chapter we combine large- and small-scale power spectra from *Planck* with the BLAST and BLAST × ACT spectra presented in Chapter 2 to estimate the frequency and scale dependence of the angular power spectrum of clustered CIB sources. We present a simple power-law template to model the clustered source contribution that may be marginalized over when estimating cosmological parameters from foreground-contaminated CMB maps as in, for instance, Hall et al. (2010), Dunkley et al. (2011), and Keisler et al. (2011).

Previous ACT and SPT results (Dunkley et al., 2011; Shirokoff et al., 2011) have found that the parameters extracted from their CMB spectra are not particularly dependent on the model adopted for the CIB source clustered power (see also Sehgal et al., 2010; Fowler et al., 2010). The ACT and SPT data sets are not yet complete; the final data will include more sky coverage as well as measurements from additional frequency channels. Millea et al. (2012) find that modeling the CIB point source clustering incorrectly for the final combined *Planck* and ACT / SPT data sets could introduce a significant bias in cosmological parameters (they estimate a 1σ bias in n_s based on the discrepancy between two different CIB clustering models). It is therefore important to understand the scale and frequency dependence of the clustered power in preparation for this future analysis. Improving constraints on CIB clustering will also help constrain the SZ power spectrum (Section 1.1.5).

In this chapter we are primarily concerned with the CIB sources as a contaminant in CMB maps. While the physical properties of this high-redshift star-forming population are important for understanding the star formation history and galaxy evolution (reviewed briefly in Section 1.4), in this analysis we do not attempt to extract information about, for example, the redshift distribution of the sources or the dark matter haloes they occupy.

In Section 3.2 we describe the data we use for our fitting, in Section 3.3 we explain our assumptions and methods, results are presented in Section 3.4 and a conclusion follows in Section 3.5.

3.2 Data

We use the BLAST 250, 350 and 500 μm auto-spectra, 250 × 350, 250 × 500 and 350 × 500 μm cross-spectra, and BLAST 250, 350 and 500 μm × ACT 148 and 218 GHz cross-spectra from Chapter 2, and *Planck* 857, 545, 353 and 217 GHz auto-spectra from Planck Collaboration et al. (2011; hereafter P11) to construct the template. We take the quadrature sum of the statistical and beam systematic uncertainties in Table 4 of P11 as the error on each *Planck* data point, neglecting any possible correlation in the beam uncertainty across different angular scales. We find that allowing such a correlation has minimal effect on our results (Section 3.4.1). The BLAST and ACT beam uncertainties are subdominant to the statistical (noise) uncertainty across the range of angular scales covered by the BLAST and BLAST × ACT data and so we likewise neglect any correlation in the errors on these spectra. The temperature to flux conversion factors given in Table 4 of P11 assume a source SED that varies as $I(\nu) \propto \nu^{-1}$; a correction is then applied to convert to the real flux units (see Sections 5.5 of P11 and 7.4.2 of Planck HFI Core Team et al., 2011b).

We subtract the Galactic dust emission (cirrus) component in the BLAST and BLAST × ACT spectra as described in Section 2.3.3, assuming that the cirrus contribution varies with angular scale as $\ell^{-2.7}$. As discussed in Chapter 2, these spectra are not very sensitive to the details of the cirrus treatment, since they are from a relatively cirrus-free patch of sky (see also Das et al., 2011a). We assume that any contribution to the power spectra other than that from the dusty galaxies (for instance, radio–CIB or tSZ–CIB correlations) is negligible. Removal of power in the *Planck* spectra that is not from unresolved CIB sources is described in Sections 2 and 3 of P11.

The *Planck* and BLAST auto-spectra are presented in Figure 3.1. We also show the 218 GHz ACT power spectrum from Das et al. (2011a) and the 220 GHz SPT spectrum from Shirokoff et al. (2011). A *WMAP*-7 best-fit ΛCDM CMB power spectrum (Komatsu et al., 2011) has been subtracted from these points; we have not subtracted any power from radio point sources or the kinematic Sunyaev-Zel'dovich effect, as these contributions are likely to be subdominant (Dunkley et al., 2011; Shirokoff et al., 2011). All the spectra show similar angular scale dependence despite spanning a broad range of frequencies and almost two decades in angular scale. Note that a color correction to account for the different bandpass filters is required to make the Planck and BLAST spectra directly comparable - see Section 3.4 for details.

The *Planck*, BLAST and ACT maps are calibrated using comparisons to various measurements including the orbital CMB dipole, Far-InfraRed Absolute Spectrophotometer (FIRAS; Mather et al., 1993) data and planetary temperature. Uncertainty in these calibrations must be accounted for in order to perform joint fits to the power spectra extracted from the different maps. The absolute photometric calibration uncertainties are 7% for the *Planck* 857 and 545 GHz maps, 2% for the *Planck* 353 and 217 GHz maps (see P11 and Planck HFI Core Team et al., 2011b), 9.5, 8.7 and 9.2% for the BLAST 250, 350 and 500 μm maps (Truch et al., 2009), 7% for the ACT 218 GHz map and 2% for the ACT 148 GHz map (Hajian et al., 2011). Furthermore, the uncertainties in the BLAST calibrations are highly correlated; this is because the dominant source of uncertainty is the spectral energy distribution (SED) of the star used for the calibration of all three bands (Truch et al., 2009).

3.3 Power-law clustering template

In the halo model formalism, introduced in Section 1.3, the two-point function of galaxy clustering is dominated on large scales by pairs of sources in different dark matter haloes (two-halo term), while on small scales galaxy pairs occupying the same halo (one-halo term) become dominant. Although these two components have different scale dependence (see Cooray & Sheth, 2002, for a detailed review), an angular correlation function varying as $w(\theta) \propto \theta^{-\delta}$ with $\delta \sim 0.8$ (Peebles, 1980, corresponding to clustering power $C_\ell^{\mathrm{C}} \propto \ell^{-1.2}$) has been found to adequately describe the clustering of, for instance,

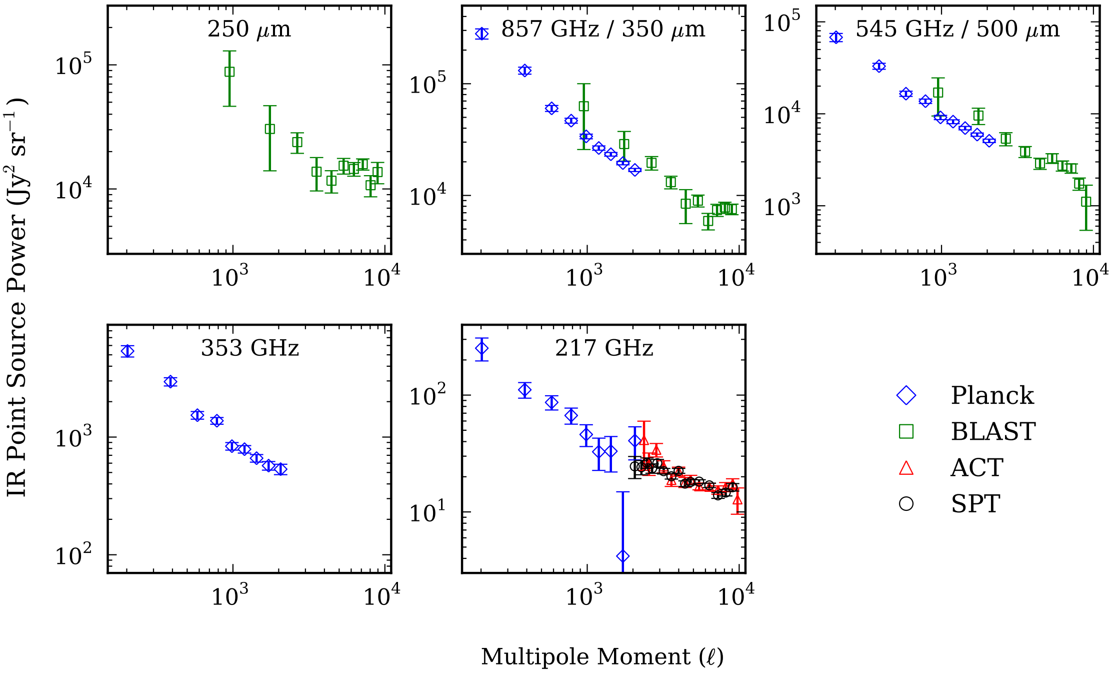

Figure 3.1: *Planck* (857, 545, 353 and 217 GHz) and BLAST (250, 350 and 500 μm) CIB source power spectra. The spectra include both shot-noise and clustered components. While these data span a broad range of frequency and angular scale there is a notable similarity in the angular scale dependence. The *Planck* error bars include both the statistical uncertainties and estimates of the systematic beam uncertainty given in Table 4 of Planck Collaboration et al. (2011c). Data points at $\ell \gtrsim 2000$ from ACT at 218 GHz (Das et al., 2011a) and SPT at 220 GHz (Shirokoff et al., 2011) have been included for comparison with the *Planck* 217 GHz spectrum. We have subtracted a *WMAP*-7 best-fit ΛCDM CMB component from these spectra. No corrections for the different bandpass filter profiles have been applied; when the different filters and photometric calibration uncertainties are accounted for the *Planck* and BLAST data are in good agreement (Section 3.4).

Lyman Break galaxies at $z \sim 3$ (Giavalisco et al., 1998) and local SDSS galaxies (Zehavi et al., 2002). Significant deviations from power-law behaviour have however been observed in analyses of more recent and comprehensive SDSS data (e.g., Zehavi et al., 2004, 2005; Blake et al., 2008), as well as in high-redshift galaxies (Ouchi et al., 2005; Lee et al., 2006; Coil et al., 2006; Wake et al., 2011). For a recent discussion of the physical origins of power-law galaxy correlation functions see Watson et al. (2011).

P11 and Amblard et al. (2011) find that a power law provides an adequate fit to the existing *Planck* and *Herschel*-SPIRE CIB anisotropy spectra (see Tables 6 and S1 in those papers, respectively). This would suggest that CIB spectra are not yet of sufficient quality to reveal deviations from power-law clustering behaviour, and we therefore also adopt a power law for the clustering component in this work.

We model the total CIB source power spectrum from correlating maps at frequency ν_1 and ν_2 ($\nu_1 = \nu_2$ for the auto-spectra) as

$$C_{\ell,\nu_1\nu_2} = A^{\mathrm{C}}_{\nu_1\nu_2}\left(\frac{\ell}{\ell_0}\right)^{-n} + C^{\mathrm{P}}_{\nu_1\nu_2}, \tag{3.1}$$

where ℓ is the multipole moment, A^{C} and n are the clustering amplitude and index, C^{P} is the Poisson shot-noise, and $\ell_0 = 3000$ is the pivot scale. This differs from the form adopted by Amblard et al. (2011) only in the choice of pivot ℓ_0. Unlike P11 we model the clustering and shot-noise as separate, independent components rather than modelling their sum as one power law. Motivated by the apparent uniformity in angular scale dependence across the different spectra (see Figure 3.1) we fit for a single, frequency-independent, value of n. We fit for a separate shot-noise level in each of the 16 *Planck*, BLAST and BLAST×ACT spectra (see Section 3.2).

The SED of the CIB, over the range of frequencies considered, has been found to be well-described by a graybody of the form (e.g., Fixsen et al., 1998; Lagache et al., 1999; Gispert et al., 2000):

$$I^{\mathrm{CIB}}_{\nu} \propto \nu^{\beta} B_{\nu}(T_{\mathrm{eff}}). \tag{3.2}$$

In reality, the sources making up the CIB lie at a range of redshifts, with a variety of luminosities and dust temperatures (see Section 1.4 and, e.g., Haiman & Knox, 2000; Knox et al., 2001; Coppin et al., 2008; Pascale et al., 2009; Hwang et al., 2010, and Chapter 5). Equation (3.2) is thus an approximation to the true CIB SED, which consists of the sum of many different (approximately) graybody spectra, and the quantities β and T_{eff} are not to be interpreted as physical parameters.

P11 found that the SED of the CIB *anisotropies* measured by *Planck* is also well-described by the Gispert et al. (2000) modified blackbody with emissivity spectral index $\beta = 1.4 \pm 0.2$ and effective temperature $T_{\mathrm{eff}} = 13.6 \pm 1.5$ K. We assume the *clustering power* SED can also be described in this form, and parametrize the frequency dependence of the auto-spectrum clustering power amplitude as $A^{\mathrm{C}} = (I^{\mathrm{C}})^2$ where

$$I^{\mathrm{C}}_{\nu} = I_0 \left(\frac{\nu}{\nu_0} \right)^{\beta} B_{\nu}(T_{\mathrm{eff}}), \tag{3.3}$$

with a single emissivity index and effective temperature.

Different frequencies are sensitive to CIB sources at different redshifts, with the importance of higher-redshift sources increasing at lower frequencies (e.g., Haiman & Knox, 2000; Knox et al., 2001; Chapin et al., 2009; Marsden et al., 2009). As a result we would not expect there to be 100% correlation between the CIB sources in different bands (particularly between the widely spaced ACT and BLAST bands) and we therefore include a clustering correlation factor f^{corr} as a free parameter for each cross-spectrum. The cross-spectrum clustering amplitude is then $A^{\mathrm{C}}_{\nu_1 \nu_2} = f^{\mathrm{corr}}_{\nu_1 \nu_2} I^{\mathrm{C}}_{\nu_1} I^{\mathrm{C}}_{\nu_2}$.

3.3.1 Poisson shot-noise

The auto-spectrum shot-noise is given by (e.g., Scott & White, 1999)

$$C^{\mathrm{P}}_{\nu} = \int dz \int_0^{S_{\mathrm{cut}}} dS_{\nu}\, S_{\nu}^2 \frac{d^2 N}{dS_{\nu}\, dz}(S_{\nu}, z), \tag{3.4}$$

where S_{cut} is the flux cut applied to the map and $d^2N/dS_{\nu}\, dz$ are the differential source counts.

In P11 the shot-noise levels were fixed using the IR galaxy evolution model of Béthermin et al. (2011 – hereafter B11, introduced in Chapter 2). This model parametrizes the evolution of the galaxy luminosity function and is fit to number counts over a wide range of wavelengths. While the model broadly fits the available data, there are discrepancies. The model underpredicts by ~40% the shot-noise levels measured at 500 μm by BLAST (Viero et al., 2009) and 220 GHz by SPT (Hall et al., 2010). We do not apply any priors on the shot-noise levels when constructing our template. We may, however, expect a considerable degeneracy between the shape of the clustering component and size of the shot-noise for the *Planck* data, because *Planck* is not able to probe the small scales where the shot-noise becomes dominant. As a result, we consider the effect of adopting the B11 model predictions as priors on the *Planck* shot-noise levels in Section 3.4.1.

In terms of the source flux and $S_{\rm cut}$ we can write the clustering power as (e.g., Bond et al., 1991a; Tegmark et al., 2002, see discussion in Section 1.3)

$$C^{\rm C}_{\ell,\nu_1\nu_2} = \int dz \left[\frac{d\chi}{dz}(z)\right]^{-1} \frac{1}{\chi^2(z)} \frac{dI_{\nu_1}}{dz}(z) \frac{dI_{\nu_2}}{dz}(z) P_{\rm gal}(k,z)\big|_{k=(\ell+1/2)/\chi(z)}. \tag{3.5}$$

where χ is the comoving distance, $P_{\rm gal}$ the three-dimensional CIB galaxy power spectrum, and the redshift-distribution of the flux, dI_ν/dz, is given by

$$\frac{dI_\nu}{dz}(z) = \int_0^{S_{\rm cut}} dS_\nu\, S_\nu \frac{d^2N}{dS_\nu\, dz}(S_\nu, z), \tag{3.6}$$

The factor of S_ν^2 in equation (3.4), compared to $(dI_\nu/dz)^2$ in equation (3.5), suggests that the removal of the highest-flux sources will have much less impact on the clustered power than on the shot-noise. The B11 model predicts that, for instance, applying a flux cut of 250 mJy (the cut applied to the BLAST 350 μm map in Chapter 2) to the *Planck* 857 GHz map would result in a $\sim$10% reduction in the shot-noise level compared to the *Planck* flux cut of 710 mJy, but that $(dI_\nu/dz)^2$ would be reduced by $< 1\%$ at $z \sim 0.2$ and virtually unaffected for $z > 1$. We allow for the dependence of the shot-noise levels on flux cut by fitting separate shot-noise levels for each spectrum, as described in the next section. We assume that the effect on the clustering power from applying different flux cuts is negligible for the data considered. Studies using higher-resolution *Herschel* maps are required to investigate the dependence of the clustering power on flux cut in more detail (see Chapter 5 for further discussion).

3.3.2 MCMC fitting

We perform a simultaneous fit to the seven auto-spectra (four *Planck* and three BLAST) plus the nine cross-spectra (three BLAST × BLAST and six BLAST × ACT). The model spectra are binned for comparison to each data spectrum, with log-likelihood

$$-2\ln\mathscr{L}(d|\theta) = \sum_{i=1}^{16}[\mathbf{C}_i^{\mathrm{data}} - \mathbf{C}_i^{\mathrm{model}}(\theta)]^2/\sigma_i^2, \tag{3.7}$$

for model parameters θ, data vector $\mathbf{C}_i^{\mathrm{data}}$ for the ith spectrum, and binned model spectra $\mathbf{C}_i^{\mathrm{model}}(\theta)$. Covariances between the sixteen spectra are neglected.

We find that the clustering SED parameters I_0, β and T_{eff} (equation 3.3) are highly degenerate. Only two of these parameters are really independent and so we fix T_{eff} to the best-fit value, 9.7 K. We choose $\nu_0 = 530$ GHz to minimise the degeneracy between I_0 and β.

We therefore fit for 37 parameters: n, the clustering index, I_0, β, 16 shot-noise levels (one for each spectrum), nine cross-spectrum correlation factors (one for each cross-spectrum) and nine photometric calibration parameters (one for each *Planck*, BLAST and ACT band). For each calibration factor we enforce a Gaussian prior centered at unity, with spread given by the nominal uncertainty listed in Section 3.2. The covariance between the BLAST calibration factors from Truch et al. (2009) is included. Apart from the calibration factors, all priors are uniform.

Given the high dimensionality, we estimate the posterior probability distribution using Markov Chain Monte Carlo (MCMC; see Section 1.5) analysis (Metropolis et al., 1953), using the sampling methods and convergence test described in Dunkley et al. (2005). Chains used for analysis are about 10^6 steps in length, and are used to calculate one-dimensional marginalized parameter values and errors.

To judge the goodness-of-fit of the model, we are also interested in the maximum likelihood. However, the peak of the likelihood distribution occupies only a small part of this high-dimensional parameter space, so the minimum χ^2 sampled in a chain of about a million steps is significantly larger than the true value ($\Delta\chi^2 \sim 10$ for a simulated 37-dimensional Gaussian distribution). There are numerous statistical methods to find the true peak of a distribution. We adopt a simple modification to the Metropolis algorithm in which chains start from the best-fitting point and then make a step in parameter space only when the posterior is improved, using a reduced trial step size. We have tested this prescription on simulated Gaussian distributions, and the peak is found to within $\Delta\chi^2 = 0.1$ in $\sim 2\times10^4$ steps for 37 dimensions. We emphasize that this modified code is used only to assess the global goodness-of-fit, not to estimate the marginalized parameter distributions.

To estimate the model spectra at each frequency, it is not sufficient to use the nominal values of ν for the BLAST and ACT bands in equation (3.3), due to the finite width of each filter. The correct effective ν values depend on the SED of the emission mechanism. The clustering SED is estimated iteratively by repeating the MCMC fitting; each time the best-fit clustering SED is integrated through the BLAST and ACT filter profiles and an improved estimate of the effective ν values obtained. We found that after three iterations the SED converged, with effective frequencies of 1248, 829 and 607 GHz (effective wavelengths 240, 362 and 494 μm) for the nominal BLAST 250, 350 and 500 μm bands, and 220 and 150 GHz for the ACT 218 and 148 GHz bands. While the clustering SED is rising steeply at the ACT bands, the shift from nominal frequency is reduced by the narrowness of the ACT filters. For the *Planck* data the nominal frequencies are used, because the temperature-to-flux conversion factors provided in P11 are given such that the flux is correct at the nominal frequencies.

3.4 Results

The model fits the data well. We find a best-fit χ^2 of 132 for 122 degrees of freedom (150 data points minus 28 parameters; we have not counted the calibration parameters since they are strongly constrained by priors), giving reduced-$\chi^2 = 1.08$. The marginalized mean values of the clustered CIB template parameters are given in Table 3.1. No errors are given for $T_{\rm eff}$, ν_0 or ℓ_0 since these parameters are fixed as described in Section 3.2. Figure 3.2 shows the best-fit clustered CIB source power for each of the bands included in the fit. The best-fit shot-noise levels have been subtracted. The χ^2 contribution from each individual spectrum is also shown; in addition to the total χ^2 being good we find that there are no spectra which are not individually well-fit by the model.

We plot the BLAST 350 and 500 μm spectra on the same axes as the *Planck* 857 and 545 GHz spectra. The BLAST spectra are color-corrected to account for the difference in the bandpass filters by taking the ratio of our clustering power predictions for the relevant *Planck* and BLAST band. We find these color correction factors to be 1.07 and 0.63 for the 350 and 500 μm BLAST spectra, respectively. P11 found values of 1.05 and 0.7 by integrating the SED of Gispert et al. (2000) through the BLAST and *Planck* filters. These values differ slightly because our best-fit clustering SED is slightly different – see Figure 3.3 for a comparison.

Table 3.1: Power-law clustering template

Parameter	Value
$n^\dagger$	1.25 ± 0.06
I_0 (Jy sr^{-1})†	$(2.43 \pm 0.16) \times 10^{-9}$
β	2.20 ± 0.07
$T_{\rm eff}$ (K)	9.7
ν_0 (GHz)	530
ℓ_0	3000
χ^2/d.o.f.	132/122

†A strong (89%) anti-correlation exists between n and I_0

The clustering power at $\ell = 3000$ is shown as a function of frequency in Figure 3.3. Also shown is the scaled Gispert et al. (2000) SED (dashed line), which was fit to measurements of the CIB intensity spectrum from COBE's FIRAS and Diffuse InfraRed Background Experiment (DIRBE; Hauser et al., 1991) instruments. It falls off more slowly with decreasing frequency than our clustering SED. Some difference between the CIB mean and anisotropy SED may be expected, since the contribution of a source to the anisotropy SED depends on its clustering as well as spectral properties.

CIB clustering power predictions at $\ell = 2000$ and 3000, calculated from our template for several *Planck*, ACT and SPT bands, are given in Table 3.2. The conversion from flux to temperature units was calculated in each case by integrating $I^{\rm C}$ from equation (3.3) through the relevant bandpass filter. The effective frequencies (i.e., single frequency value that gives the same clustering amplitude as integrating through the filter) are also given. Since the CIB clustering amplitude is rising strongly with frequency at the CMB bands (see Figure 3.3), the different filter profiles lead to significant differences in the clustering power even for bands with closely-spaced nominal frequencies. The amplitude of the clustered power may vary by a factor of 10 across a single filter, as shown in Figure 3.3.

The predictions at $\ell = 3000$ can be compared to the ACT results from Dunkley et al. (2011) and SPT results from Shirokoff et al. (2011). ACT find a best-fit clustering amplitude of 4.6 ± 1.1 and 54 ± 13 μK^2 at 148 and 218 GHz, respectively (we have calculated these uncertainties by adding their statistical and systematic error estimates in quadrature). SPT find 6.1 ± 0.8 and 57 ± 8 μK^2 at 150 and 220 GHz, respectively, for their base-line model, which includes a power-law CIB clustering component with index $n = 1.2$. Our predictions are in excellent agreement with these results. Figure 3.4 shows

Table 3.2: CIB clustering predictions from our template – $\ell(\ell+1)C_\ell^{\rm clust}/2\pi$ (μK^2)

Band	$\nu_{\rm eff}$ (GHz)	$\ell = 2000$	$\ell = 3000$
Planck 100 GHz	104	0.49 ± 0.07	0.67 ± 0.09
Planck 143 GHz	146	2.9 ± 0.3	3.9 ± 0.4
Planck 217 GHz	226	45 ± 4	61 ± 6
ACT 148 GHz	150	3.2 ± 0.4	4.4 ± 0.5
ACT 218 GHz	220	36 ± 3	49 ± 4
SPT 95 GHz	99	0.38 ± 0.05	0.51 ± 0.07
SPT 150 GHz	156	4.1 ± 0.4	5.5 ± 0.6
SPT 220 GHz	221	37 ± 3	50 ± 5

ACT and SPT data at 220 GHz with our clustering template predictions over-plotted, along with an CIB shot-noise component and a ΛCDM CMB power spectrum.

We also make predictions for the spectral index α of the clustered component. At the CMB frequencies the clustering SED can be approximated as a power law, $I_\nu^{\rm C} \propto \nu^\alpha$, however, the CMB bands do not lie strictly in the Rayleigh-Jeans limit of the modified blackbody adopted in our model. Consequently the equivalent power-law slope at 150 GHz differs from that at 220 GHz: we find $\alpha_{150} = 3.78 \pm 0.07$ and $\alpha_{220} = 3.56 \pm 0.07$. We also calculate an effective spectral index between 150 and 220 GHz, $\alpha_{150-220} = 3.68 \pm 0.07$. This result is consistent with ACT and SPT findings of 3.69 ± 0.14 and 3.58 ± 0.08, respectively.

We have considered only the frequency dependence of the CIB clustering component, not the shot-noise. Investigating shot-noise frequency dependence is more difficult, due to stronger flux cut dependence and the fact that the *Planck* data are limited to large scales; modelling the shot-noise power is considered in more detail in Chapter 5.

3.4.1 Validating assumptions

While our single-index power-law clustering model provides a good fit to the data in terms of χ^2, in this section we attempt to further validate our assumptions regarding the scale and frequency dependence of the clustered power.

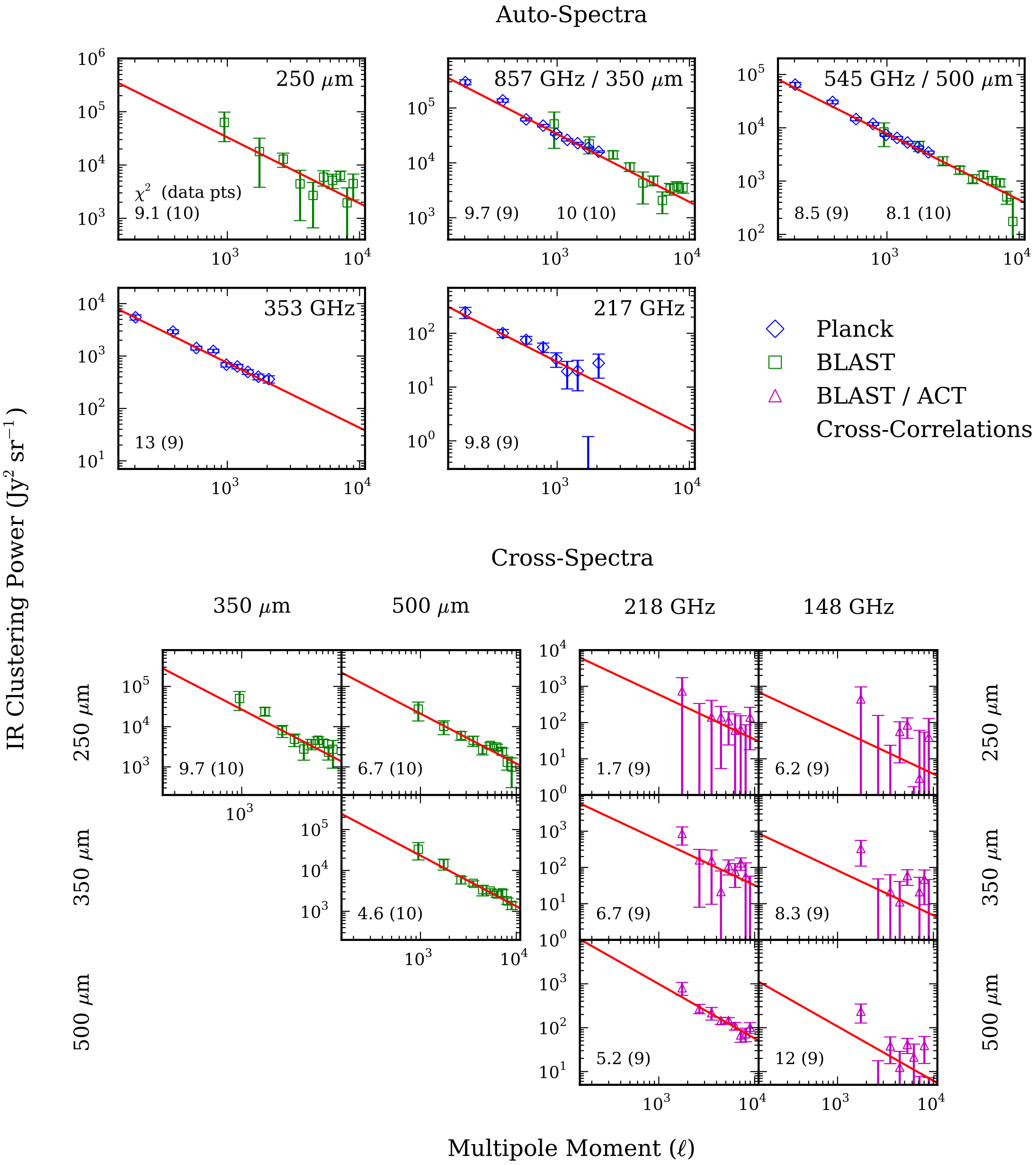

Figure 3.2: CIB point source clustering power spectra from *Planck* (diamonds), BLAST (squares) and BLAST / ACT cross-correlations (triangles). The solid lines are the best-fit power law with scale dependence $C_\ell^{\mathrm{C}} \propto \ell^{-n}$ – we find $n = 1.25 \pm 0.06$. The frequency dependence of the clustering SED is described by a modified blackbody (see equation 3.3 and Table 3.1). Poisson shot-noise has been subtracted for each panel (shot-noise levels from our fitting are given in Table 3.3). For the combined fit the χ^2/degree of freedom is 132/122. The contribution to the total χ^2 from the individual spectra is included in each panel. Color correction factors of 1.07 and 0.63 have been applied to the BLAST 350 and 500 μm spectra so they are directly comparable with the *Planck* 857 and 545 GHz spectra, respectively, as described in the text.

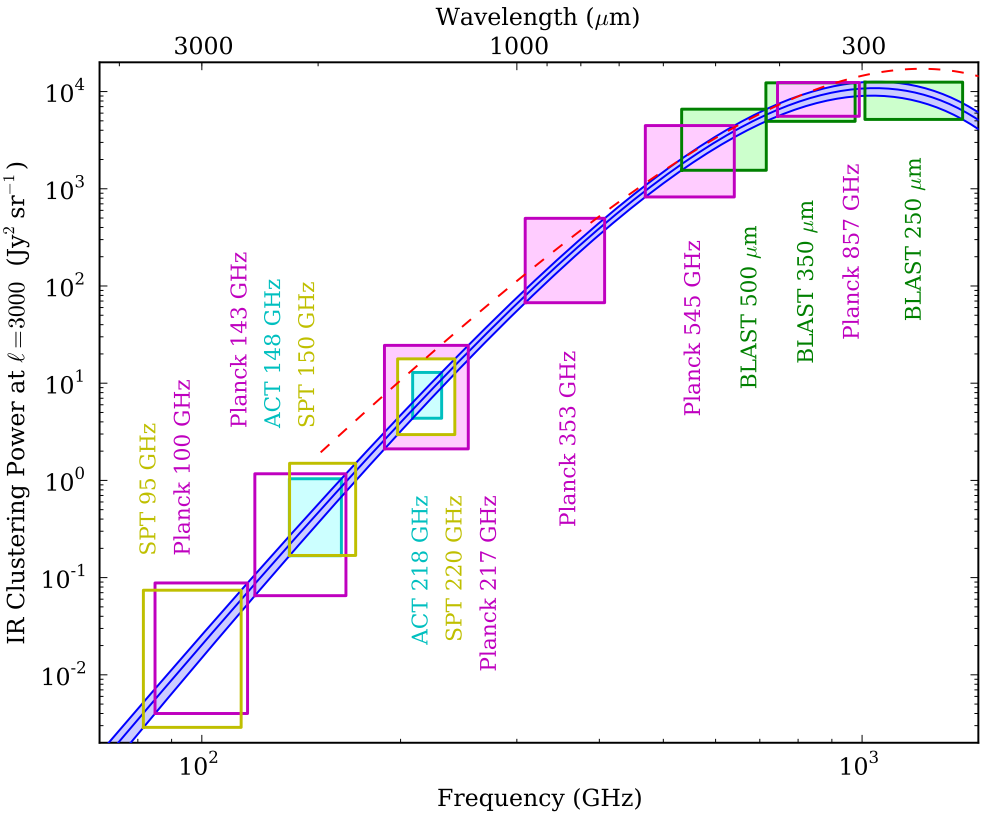

Figure 3.3: Frequency dependence of CIB point source clustering power at $\ell = 3000$. We assume this frequency dependence can be described by a modified blackbody: $C^{\mathrm{C}}_{\ell=3000}(\nu) \propto \left[\nu^{\beta} B_{\nu}(T_{\mathrm{eff}})\right]^2$. The solid lines show the best-fit and 1-σ uncertainties from our fitting; parameter values are given in Table 3.1. The dashed line is the SED of Gispert et al. (2000), which has been scaled for comparison. The rectangles show the *Planck*, BLAST, ACT and SPT bandpass filters FWHM values in the horizontal direction. The vertical extent of the rectangles shows the variation of the clustering power across each filter; in some cases this variation is a factor of 10 or more due to how steeply the clustering SED rises with frequency. The shaded rectangles show the bands that were used for the fitting in this paper. Spectra from the other bands are either not yet available or were not used, due to the risk of biasing results by assumptions regarding the separation of the CMB and other components from the CIB contribution.

Shot-noise

Table 3.3 shows the 1-D marginalized values of the shot-noise levels from our MCMC chains (C^{P} from equation 3.1). It should be noted that, as expected, the *Planck* shot-noise levels and the clustering index n are highly correlated. The shot-noise predictions for each auto-spectrum from the B11 model are given for comparison. Our values are consistent with the model within 1.5σ in all cases. We repeated the MCMC analysis described in Section 3.2 using the B11 model predictions as Gaussian priors on the *Planck* shot-noise levels and found a best-fit $\chi^2/\text{d.o.f.} = 139/122$, an increase of $\Delta\chi^2 = 7$ compared to the case with uniform priors. There was minimal change in the clustering template parameters (e.g., $n = 1.24 \pm 0.03$ with the shot-noise prior). This suggests that uncertainty in the *Planck* shot-noise levels is not having a significant impact on our results.

Table 3.3: 1-D marginalized shot-noise levels

Band	Marginalized Value ($\mathrm{Jy}^2\ \mathrm{sr}^{-1}$)	Béthermin et al. (2011) ($\mathrm{Jy}^2\ \mathrm{sr}^{-1}$)
Planck 857 GHz	2200 ± 2500	5920 ± 370
Planck 545 GHz	1700 ± 700	1150 ± 90
Planck 353 GHz	210 ± 60	138 ± 22
Planck 217 GHz	16 ± 6	12 ± 3
BLAST 250 μm	11600 ± 2300	11600 ± 2100
BLAST 350 μm	5200 ± 1200	5050 ± 1080
BLAST 500 μm	1300 ± 390	1680 ± 480
250 μm × 350 μm	5700 ± 1400	
250 μm × 500 μm	1830 ± 690	
350 μm × 500 μm	820 ± 490	
250 μm × 218 GHz	240 ± 130	
250 μm × 148 GHz	90 ± 70	
350 μm × 218 GHz	240 ± 70	
350 μm × 148 GHz	110 ± 40	
500 μm × 218 GHz	66 ± 30	
500 μm × 148 GHz	55 ± 20	

Photometric calibration

The marginalized values for the photometric calibration parameters from our MCMC chains are shown in Table 3.4 along with the nominal uncertainties. We would expect the calibration parameters to be consistent with unity within the nominal uncertainty. If this were not the case it could indicate that the modified blackbody spectrum in equation (3.3) was not a suitable description for the frequency dependence of the clustering amplitude, however all are consistent with the nominal values.

Table 3.4: 1-D marginalized calibration parameters

Band	Marginalized Value	Nominal Uncertainty
Planck 857 GHz	1.05 ± 0.06	7%
Planck 545 GHz	0.99 ± 0.04	7%
Planck 353 GHz	1.01 ± 0.02	2%
Planck 217 GHz	1.00 ± 0.02	2%
BLAST 250 μm	1.05 ± 0.08	9.5%
BLAST 350 μm	1.03 ± 0.07	8.7%
BLAST 500 μm	1.02 ± 0.07	9.2%
ACT 218 GHz	1.03 ± 0.07	7%
ACT 148 GHz	1.00 ± 0.02	2%

***Planck* beam uncertainty**

As stated in Section 3.2, we neglected any possible correlation in the *Planck* beam uncertainty across different angular scales. We re-ran the MCMC chain enforcing a 100% correlation in the beam uncertainty in different ℓ-bins for each *Planck* spectrum (introducing off-diagonal elements in the likelihood – equation 3.7) and found minimal change in the marginalized parameter values ($< 0.3\sigma$ in all cases). While the *Planck* beam uncertainties at $\ell \sim 2000$ are comparable to or larger than the statistical uncertainties, the template parameters are primarily constrained by the large-scale *Planck* data (where the beam uncertainties are sub-dominant) and the BLAST data.

Comparison with broken power law

We assumed that the scale dependence of the clustering power can be described using a single index n. In this section we consider fitting the scale dependence with a broken power law of the form

$$C_\ell^{\mathrm{clust}} \propto \begin{cases} \ell^{-n_1} \text{ if } \ell \leq \ell_{\mathrm{b}} \\ \ell^{-n_2} \text{ if } \ell > \ell_{\mathrm{b}}, \end{cases} \tag{3.8}$$

where n_1, n_2 and ℓ_b are free parameters. When we repeat the fit to the *Planck*, BLAST and BLAST × ACT spectra with this new scale dependence we find $n_1 = 1.24 \pm 0.06$, $n_2 = 1.2 \pm 0.2$ and $\ell_b = 1100 \pm 300$ with a best $\chi^2/\mathrm{d.o.f.} = 131/120$. This is an improvement of only $\Delta\chi^2 = 0.9$ with two additional fitted parameters. For the fit with priors on the *Planck* shot-noise levels from the B11 model the improvement is only $\Delta\chi^2 = 0.4$. We conclude that the data do not show a significant preference for a broken power law.

Keisler et al. (2011) adopted a template of the form given in equation (3.8) with $n_1 = 2.0$, $n_2 = 1.2$ and $\ell_\mathrm{b} = 1500$ to model the CIB clustered power when extracting cosmological information from the small-scale SPT 150 GHz CMB power spectrum. We find that this form is not a good fit to the *Planck* data, with $\chi^2/\mathrm{d.o.f.} = 22/7$ when we fit to the *Planck* 217 GHz spectrum with n_1, n_2 and ℓ_b fixed to the above values and using uniform priors on the clustering amplitude and shot-noise.

Comparison with linear bias model

In the analysis described in Chapter 2, we found that the BLAST and BLAST × ACT data are well-fit by assuming the CIB galaxy power spectrum in equation (3.5) is given by

$$P_\mathrm{gal}(k,z) = b^2 P_\mathrm{DM}^{linear}(k,z), \tag{3.9}$$

where b is the linear bias factor, using the B11 predictions for the redshift-distribution of the flux, dI_ν/dz. P11 also found that the *Planck* data from each band are well-fit by this model (also using the B11 dI_ν/dz) if no prior is enforced on the shot-noise levels. The bias levels are not consistent; when fitting for a single, redshift-independent value of b, we found $b = 5.0 \pm 0.4$ in Chapter 2, whereas P11 found $b = 2.18 \pm 0.11$ for the *Planck* 545 GHz spectrum.

The linear bias model is strongly rejected by the combined *Planck* and BLAST data even without any shot-noise prior. Fitting a linear bias model with single-value bias to the *Planck* 857 GHz and BLAST 350 μm spectra together, using the B11 dI_ν/dz and multiplying the BLAST data points by a color correction factor of 1.07 (see Section 3.4), yields $\chi^2/\mathrm{d.o.f.} = 39/16$. For a joint fit to the *Planck* 545 GHz and BLAST 500 μm spectra we find $\chi^2/\mathrm{d.o.f.} = 43/16$. This result is driven by the shape of the linear matter power spectrum rather than the choice of dI_ν/dz: we repeated the fitting using the

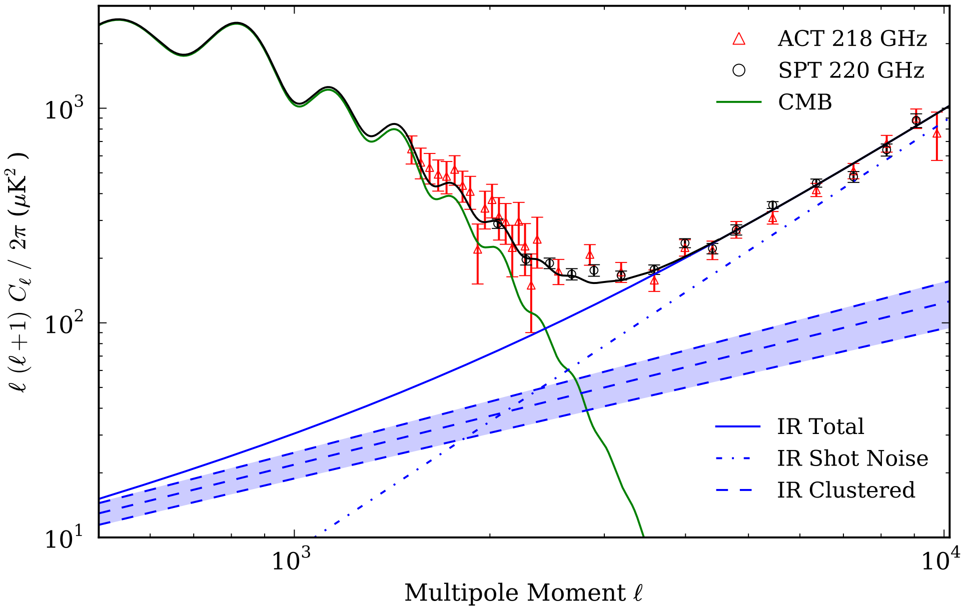

Figure 3.4: The angular power spectra at 220 GHz measured by ACT (Das et al., 2011a) and SPT (Shirokoff et al., 2011), with a theoretical model for CMB and infrared point sources over-plotted. The clustered CIB component is given by the power-law model fit to *Planck*, BLAST and BLAST × ACT data in this analysis (see equations 3.1 and 3.3 and Table 3.1 for parameter values). The upper and lower dashed lines correspond to 1σ error bounds. The lensed CMB spectrum is that of the ΛCDM model with parameters derived from *WMAP* (Komatsu et al., 2011). A CIB shot-noise component of size $\ell(\ell+1)C_{\rm P}/2\pi|_{\ell=3000} = 78\ \mu{\rm K}^2$ (consistent with ACT and SPT measurements) has also been plotted. Additional radio source and kinematic SZ power are subdominant at this frequency and are not included.

predictions of Marsden et al. (2011) rather than B11 and found χ^2/d.o.f. of 36/16 and 42/16 for the 857 GHz / 350 μm and 545 GHz / 500 μm spectra respectively. Neither the *Planck* nor BLAST data alone were able to rule out the linear bias model without a shot-noise prior because of the limited angular scales probed. Shirokoff et al. (2011) similarly found that the linear bias model could not be ruled out using only SPT data from $\ell \gtrsim 2000$.

3.4.2 Cross-correlations

Table 3.5 shows the marginalized degree of clustering correlation, $f^{\rm corr}$, for each cross-spectrum included in our fitting, along with the separation $\Delta\nu$ between the two bands. The BLAST × BLAST cross-spectra are consistent with 100% correlation. Our conclusions regarding the degrees of correlation between the

ACT and BLAST bands are limited by the data quality. A decrease in correlation with increasing band separation would be consistent with the sources lying at a range of redshifts, with the higher-redshift sources being of greater relative importance at the longer wavelengths (e.g., Haiman & Knox, 2000), however the current data are not of sufficient quality to confirm this.

Two of the marginalized mean $f_{\rm corr}$ values lie more than 1σ above unity, while none lie more than 1σ below. Measuring $f_{\rm corr} > 1$ may indicate that the angular scale dependence of the cross-spectra clustering power is not described by the same single-index power law as the auto-spectra clustering, since there is no physical explanation for a correlation in excess of 100%. This could be the case even with no worsening of the χ^2, due to the limited angular scales probed by the BLAST × ACT data. To test that this is not having a significant effect on our clustering template, we repeated the MCMC fitting described in Section 3.2 using only the auto-spectrum data. We found that the values of n, β and I_0 change by $< 0.5\sigma$ compared to the fit with the cross-spectra included. We conclude that, while the data may be hinting that the cross-spectrum clustering power has a different shape to the auto-spectrum clustering, this is not significantly biasing our template. A more sophisticated CIB source model, described in Chapter 5, predicts a high degree of submm / mm correlation, consistent with the results in Table 3.5.

Further submm / mm cross-correlation studies (e.g., *Herschel* × ACT / SPT) are clearly required to provide more insight into the distribution of the sources with redshift, to constrain the angular scale dependence of the cross-spectrum clustering, and to investigate how the clustering shape changes with increasing band separation.

Table 3.5: Degree of clustering cross-correlation, $f^{\rm corr}$

Band 1	Band 2	$\Delta\nu$ (GHz)	Marginalized Value
250 μm	350 μm	340	0.98 ± 0.30
250 μm	500 μm	600	1.23 ± 0.31
350 μm	500 μm	260	1.41 ± 0.28
250 μm	218 GHz	982	0.66 ± 1.09
250 μm	148 GHz	1052	0.30 ± 1.83
350 μm	218 GHz	642	0.64 ± 0.56
350 μm	148 GHz	712	0.39 ± 1.05
500 μm	218 GHz	382	1.82 ± 0.47
500 μm	148 GHz	452	0.79 ± 0.87

3.5 Conclusions

We have found that a power-law model for the CIB source clustering is adequate to simultaneously fit *Planck*, BLAST and cross-correlated BLAST / ACT power spectrum data over a broad range of frequency ($150 < \nu < 1200$ GHz) and angular scale (multipole moment $100 < \ell < 9000$). We find the clustering power varies with angular scale as ℓ^{-n} with $n = 1.25 \pm 0.06$ and that the SED of the clustering can be described as a modified blackbody with emissivity index $\beta = 2.20 \pm 0.07$ and effective temperature $T_{\mathrm{eff}} = 9.7$ K. Our work does not rely on any assumptions regarding the physical properties of the CIB sources (host haloes, redshift distribution, etc.).

As well as providing a simple template for use in CMB foreground subtraction, we have established that the *Planck* and BLAST / BLAST × ACT data sets appear compatible when bandpass filters, flux cut and calibration are accounted for, as described in Sections 3.2 and 3.3. We make predictions for the CIB clustering power for the *Planck*, ACT and SPT CMB bands; our predictions for the ACT and SPT bands at around 150 and 220 GHz are fully consistent with existing measurements (Dunkley et al., 2011; Shirokoff et al., 2011).

There is uncertainty in the *Planck* shot-noise levels because *Planck* does not probe small enough scales for the shot-noise to become dominant. We find reasonable consistency between the shot-noise levels from our fitting and the predictions of the parametric IR galaxy evolution model of Béthermin et al. (2011). We repeated our fitting using this model's predictions as priors on the *Planck* shot-noise levels and found there was minimal effect on the scale or frequency dependence of the clustering power.

Upcoming data from *Herschel*, *Planck*, ACT, SPT, and cross-correlations will allow us to look for any variations in the clustering angular scale dependence with frequency. Understanding this scale dependence in the mm CMB bands is important not only for extracting unbiased estimates of cosmological parameters, but also for constraining other components of the measured spectrum, such as the thermal and kinematic SZ effect, and any cross-component correlations, for instance tSZ-CIB (see Chapter 4).

Over the range of angular scales considered we would expect to be probing both the linear and non-linear clustering regimes. This is supported by the fact that the combined *Planck* and BLAST data strongly reject a linear bias clustering model (Section 3.4.1). The linear and non-linear components have different scale dependence, with the linear component dominating on large scales and the non-linear on small scales. The fact that our study has found that a power-law scale dependence provides a good fit to the *Planck* and BLAST CIB point source clustering power is not inconsistent with this picture; instead it suggests that the sum of the linear and non-linear components is sufficiently close to a power law that the current data are unable to reveal any deviations. We can draw a comparison to measurements of the angular correlation function, $w(\theta)$, of luminous red galaxies and galaxies in the main SDSS sample, which have revealed deviations from power law behaviour (e.g., Zehavi et al., 2004, 2005; Blake et al., 2008) whereas earlier studies of galaxy clustering were unable to do so (e.g., Zehavi et al., 2002). We may expect similar deviations to be detected in future CIB source power spectra, in particular with *Herschel*-SPIRE data, which will yield higher quality data than BLAST out to smaller scales with its improved angular resolution.

The correlation function of resolved sub-mm sources (e.g., Cooray et al., 2010; Maddox et al., 2010) provides complementary information to the power spectra of unresolved sources considered in this work. Current data is limited; Guo et al. (2011) measure $\xi(r) \propto r^{-\gamma}$ with $\gamma \sim 2$, corresponding to $C_\ell^{\mathrm{C}} \propto \ell^{-1}$, for low-redshift ($z < 0.5$) *Herschel*-ATLAS galaxies, although their result is consistent with ours within errors. The full *Herschel*-ATLAS survey (Eales et al., 2010) will cover 30 times more sky and provide far tighter constraints. Discrepancies between the C_ℓ^{C} and $\xi(r)$ or $w(\theta)$ measurements would indicate differences in clustering properties of the bright sub-mm galaxies compared to the fainter population, and thus both statistics are important for constraining models of galaxy clustering and evolution.

Chapter 4

Modelling the correlation of the thermal Sunyaev Zel'dovich effect with the cosmic infrared background

4.1 Introduction

A natural application of the halo model is to understand the correlation between two different source populations, each tracing the underlying dark matter but having different dependence on host halo properties (e.g., Cooray & Sheth, 2002). In this chapter, I present such a treatment for the angular power spectrum arising from the correlation between unresolved clusters contributing to the thermal Sunyaev Zel'dovich effect (tSZ; Sunyaev & Zel'dovich, 1970), and the dusty sources that make up the cosmic infrared background (CIB; e.g., Puget et al., 1996). Along with radio sources, these two populations are currently of interest as foregrounds in Cosmic Microwave Background (CMB) temperature anisotropy analysis (see brief discussion in Section 1.1.5 and, e.g., White & Majumdar, 2004; Righi et al., 2008). As discussed in Chapter 1, the tSZ effect arises from the Compton scattering of CMB photons by hot electrons in massive galaxy clusters, while the CIB sources are understood to be mostly high-redshift ($z \sim 1-4$) galaxies undergoing active, dust-enshrouded star formation (e.g., Bond et al., 1986, 1991a; Hughes et al., 1998; Blain et al., 1999; Draine, 2003). Absorption of the starlight by the dust grains and subsequent thermal re-emission leads to strong rest-frame far-infrared emission, and cosmic expansion stretches these photons' wavelengths so they are detected in the mm-bands of contemporary CMB missions including ACT, SPT, and *Planck* (Planck Collaboration et al., 2011c), as discussed in Chapter 1.

The size of the tSZ×CIB cross-correlation provides physical information about the extent to which the CIB sources are associated with the clusters that contribute to the tSZ signal. Understanding how and why star formation in massive systems has evolved over cosmic time (e.g., Chapman et al., 2005; Pannella et al., 2009; Magnelli et al., 2011) is key to understanding galaxy evolution. In addition, Reichardt et al. (2012 – hereafter R12) have recently found that uncertainty in the tSZ×CIB power significantly degrades constraints on the kinematic Sunyaev Zel'dovich effect (kSZ) from SPT data. The kSZ arising from peculiar motion of galaxy clusters has recently been detected (Hand et al., 2012), however improving constraints on the kSZ power from patchy reionization – in which CMB photons scatter off electrons in expanding ionized gas bubbles (Knox et al., 1998) – is of great interest for constraining the duration of reionization and thus star formation in the early universe. For these reasons, a model for the tSZ×CIB power is required, and we choose a halo model framework since, as stated, it provides a natural basis for relating two different tracers of the matter field, and, furthermore, it has already been used to study the tSZ and CIB anisotropies.

We note that a similar halo model approach has recently been used to model the cross-correlation of the tSZ effect with the integrated Sachs–Wolfe effect (Taburet et al., 2011), and the distribution of galaxy clusters (Fang et al., 2012).

In Section 4.2 we collate the halo model equations for the tSZ and CIB power spectra and present expressions describing the tSZ×CIB cross-correlation. In Sections 4.3 and 4.4 we combine recent models for the tSZ and CIB and calculate the tSZ×CIB contribution as a function of frequency and angular scale. The uncertainties in current models and the role of upcoming data sets are discussed in Section 4.5 and conclusions follow in Section 4.6.

For the results presented in Section 4.4 we adopt a flat, ΛCDM cosmology, with $h = H_0/100$ km s^{-1} Mpc^{-1} $= 0.70$, $\Omega_{\rm m} = 0.27$, $\Omega_{\rm b} = 0.045$, and $\sigma_8 = 0.80$, consistent with *WMAP*-7 results (Komatsu et al., 2011).

4.2 Model

Analysis of mm CMB data is typically performed using thermodynamic temperature units, while in the submm, where the CIB is dominant, it is more natural to work with units of flux density. The equations in this section contain a mix of units, however the plots in Section 4.4 are made in either flux or temperature units. The conversion from thermodynamic temperature to flux density requires multiplying by $\partial B_\nu(T)/\partial T|_{T=T_{\rm CMB}}$, where

$$\frac{\partial B_\nu}{\partial T}(T) = \frac{2k_{\rm B}\nu^2}{c^2}\frac{x^2 e^x}{(e^x-1)^2}, \tag{4.1}$$

with $x = h_{\rm p}\nu/k_{\rm B}T$ and the present-day CMB temperature $T_{\rm CMB} = 2.725$ K. Note that converting between units requires an integral across the bandpass filter for the finite bands of real experiments.

4.2.1 CIB power

The angular power spectrum of unresolved CIB sources at multipole moment ℓ from correlating two maps at frequency ν_1 and ν_2 may be written as

$$C^{\rm CIB}_{\ell,\nu_1\nu_2} = C^{\rm CIB-C}_{\ell,\nu_1\nu_2} + C^{\rm CIB-P}_{\nu_1\nu_2}. \tag{4.2}$$

where the clustered component, $C_\ell^{\rm CIB-C}$, arises from the correlation of images of different sources in the two maps, while the Poissonian shot noise component, $C^{\rm CIB-P}$, is due to the finite number of sources in any given observed field, and may be thought of as arising from the correlation of images of the same source in the two maps (Bond, 1996). For the range of angular scales considered (∼arcminute and larger), the CIB sources are effectively point sources, and so the CIB shot noise is scale-independent.

We use equation (3.5) for the CIB clustered power,

$$C^{\rm C}_{\ell,\nu_1\nu_2} = \int dz \left[\frac{dV_{\rm c}}{dz}(z)\right]^{-1} \frac{dI_{\nu_1}}{dz}(z)\frac{dI_{\nu_2}}{dz}(z)\, P_{\rm gal}(k,z)|_{k=(\ell+1/2)/\chi(z)}, \tag{4.3}$$

where $dV_c/dz = \chi^2 d\chi/dz$ is the comoving volume element per steradian, and write $P_{\rm gal}$ as the sum of one- and two-halo terms, corresponding to the contribution from pairs of sources lying in the same dark matter halo, and different haloes, respectively (Cooray & Sheth, 2002):

$$P_{\mathrm{gal}}(k,z) = P_{\mathrm{gal}}^{\mathrm{1h}}(k,z) + P_{\mathrm{gal}}^{\mathrm{2h}}(k,z), \tag{4.4}$$

where

$$P_{\mathrm{gal}}^{\mathrm{1h}}(k,z) = \int dM \, \frac{dn_{\mathrm{h}}}{dM}(M,z) \frac{\langle N_{\mathrm{gal}} \left(N_{\mathrm{gal}} - 1 \right) \rangle}{n_{\mathrm{gal}}^2(z)} u_{\mathrm{gal}}^2(k,M,z) \tag{4.5}$$

and

$$P_{\mathrm{gal}}^{\mathrm{2h}}(k,z) = P_{\mathrm{DM}}(k,z) \left(\int dM \, \frac{dn_{\mathrm{h}}}{dM}(M,z) \, b_{\mathrm{h}}(k,M,z) \frac{\langle N_{\mathrm{gal}} \rangle}{n_{\mathrm{gal}}(z)} \, u_{\mathrm{gal}}(k,M,z) \right)^2 . \tag{4.6}$$

The integrals are over halo mass; dn_{h}/dM is the halo mass function, $N_{\mathrm{gal}}(M,z)$ the number of CIB sources hosted by a halo, u_{gal} the Fourier transform of the spatial distribution of the sources within their halo, and b_{h} the halo bias relative to the dark matter power spectrum, P_{DM}, such that the halo and dark matter power spectra are related by

$$P_{\mathrm{h}}(k,M,z) = b_{\mathrm{h}}^2(k,M,z) \, P_{\mathrm{DM}}(k,z). \tag{4.7}$$

The comoving CIB source number density, n_{gal}, is given by

$$n_{\mathrm{gal}}(z) = \int dM \, \frac{dn_{\mathrm{h}}}{dM}(M,z) \langle N_{\mathrm{gal}} \rangle, \tag{4.8}$$

and the angled brackets denote averaging over all haloes of mass M at redshift z.

As stated in Section 1.3, equation (4.3) assumes that the spectral properties of the CIB sources are not dependent on properties of their host haloes. To make our approach more general, and to facilitate writing down the tSZ×CIB cross-correlation term later, we allow the CIB flux from a source at a given redshift to depend on halo mass (as in, e.g., Righi et al., 2008; Sehgal et al., 2010; Shang et al., 2012). This requires weighting each integral over halo mass with the mean source flux, $\langle S_\nu(M,z) \rangle$, yielding (omitting dependence on angular scale, redshift and halo mass for brevity)

$$P_{\mathrm{gal},\nu_1\nu_2}^{\prime\mathrm{1h}} = \int dM \, \frac{dn_{\mathrm{h}}}{dM} \frac{\langle S_{\nu_1} \rangle \langle S_{\nu_2} \rangle \langle N_{\mathrm{gal}} \left(N_{\mathrm{gal}} - 1 \right) \rangle}{s_{\nu_1} s_{\nu_2}} u_{\mathrm{gal}}^2 \tag{4.9}$$

and

$$P'^{\rm 2h}_{{\rm gal},\nu_1\nu_2} = P_{\rm DM} \int dM_1 \, \frac{dn_{\rm h}}{dM_1} \, b_{\rm h} \frac{\langle S_{\nu_1} \rangle \langle N_{\rm gal} \rangle}{s_{\nu_1}} \, u_{\rm gal} \int dM_2 \, \frac{dn_{\rm h}}{dM_2} \, b_{\rm h} \frac{\langle S_{\nu_2} \rangle \langle N_{\rm gal} \rangle}{s_{\nu_2}} \, u_{\rm gal}, \tag{4.10}$$

where

$$s_\nu(z) = \int dM \, \frac{dn_{\rm h}}{dM}(M,z) \langle S_\nu(M,z) \rangle \langle N_{\rm gal} \rangle. \tag{4.11}$$

Substituting into equation (4.3), and recognizing that $dI_\nu^{\rm CIB}/dz = s_\nu dV_{\rm c}/dz$, gives

$$C^{\rm CIB}_{\ell,\nu_1\nu_2} = C^{\rm CIB-1h}_{\ell,\nu_1\nu_2} + C^{\rm CIB-2h}_{\ell,\nu_1\nu_2} + C^{\rm CIB-P}_{\nu_1\nu_2}, \tag{4.12}$$

with the following expressions for the one- and two-halo terms:

$$C^{\rm CIB-1h}_{\ell,\nu_1\nu_2} = \int dz \frac{dV_{\rm c}}{dz} \int dM \, \frac{dn_{\rm h}}{dM} \, \langle S_{\nu_1} \rangle \, \langle S_{\nu_2} \rangle \langle N_{\rm gal} \left(N_{\rm gal} - 1 \right) \rangle \, u^2_{\rm gal}, \tag{4.13}$$

and

$$C^{\rm CIB-2h}_{\ell,\nu_1\nu_2} = \int dz \frac{dV_{\rm c}}{dz} P_{\rm DM} \int dM_1 \, \frac{dn_{\rm h}}{dM_1} \, b_{\rm h} \, \langle S_{\nu_1} \rangle \, \langle N_{\rm gal} \rangle \, u_{\rm gal} \int dM_2 \, \frac{dn_{\rm h}}{dM_2} \, b_{\rm h} \, \langle S_{\nu_2} \rangle \, \langle N_{\rm gal} \rangle \, u_{\rm gal}. \tag{4.14}$$

The CIB shot noise contribution is given by (e.g., Scott & White, 1999)

$$C^{\rm CIB-P}_\nu = \int dS_\nu \frac{dN}{dS_\nu} S^2_\nu, \tag{4.15}$$

so in terms of the halo model quantities defined above we have

$$C^{\rm CIB-P}_{\nu_1\nu_2} = \int dz \frac{dV_{\rm c}}{dz} \int dM \, \frac{dn_{\rm h}}{dM} \, \langle S_{\nu_1} S_{\nu_2} \rangle \langle N_{\rm gal} \rangle. \tag{4.16}$$

Note that the shot noise depends on $\langle S_{\nu_1} S_{\nu_2} \rangle$ whereas the one-halo power depends on $\langle S_{\nu_1} \rangle \langle S_{\nu_2} \rangle$. If the framework described here is to be used to perform joint fits to the shot noise and clustered power, the distribution of CIB source flux at fixed M and z must therefore be considered.

Further modifications to these equations, such as distinguishing between the first, ‘central’, source occupying a halo and subsequent, ‘satellite’, sources (e.g., Berlind et al., 2003; Kravtsov et al., 2004;

Zheng et al., 2005; Tinker et al., 2010b), may easily be made.

The CIB intensity (one-point function), $I_\nu^{\rm CIB}$, is simply the integral of $dI_\nu^{\rm CIB}/dz$, and is therefore given by

$$I_\nu^{\rm CIB} = \int dz \frac{dV_{\rm c}}{dz} \int dM \, \frac{dn_{\rm h}}{dM} \langle S_\nu \rangle \langle N_{\rm gal} \rangle. \tag{4.17}$$

Note that the clustered power, shot noise and CIB intensity may all have quite different redshift dependence, due to the different factors appearing in the integrals in these equations. This point is demonstrated in Section 4.4.

4.2.2 tSZ power

In the halo model, the tSZ angular power spectrum from correlating two maps at frequency ν_1 and ν_2 is

$$C_{\ell,\nu_1\nu_2}^{\rm tSZ} = C_{\ell,\nu_1\nu_2}^{\rm tSZ-1h} + C_{\ell,\nu_1\nu_2}^{\rm tSZ-2h}. \tag{4.18}$$

We follow previous studies (e.g., Komatsu & Seljak, 2002; Shaw et al., 2009; Battaglia et al., 2010) in treating each dark matter halo as hosting a single, extended source (electron population) for the purposes of contributing to the tSZ power. Unlike for the CIB sources, the one-halo term and the Poisson shot noise are then the same thing (which we will refer to as the one-halo term). The inter-cluster two-halo term has been neglected in existing mm-band CMB analysis, since, due to the scarcity of massive clusters, it is important only for $\ell \lesssim 300$ (Komatsu & Kitayama, 1999), and on these scales the primary CMB anisotropy is completely dominant.

Again invoking the small-sky approximation, we write the one- and two-halo tSZ components as (Komatsu & Kitayama, 1999; Komatsu & Seljak, 2002):

$$C_{\ell,\nu_1\nu_2}^{\rm tSZ-1h} = g_{\nu_1} g_{\nu_2} T_{\rm CMB}^2 \int dz \frac{dV_{\rm c}}{dz}(z) \int dM \, \frac{dn_{\rm h}}{dM}(M,z) \, \tilde{y}_\ell^2(M,z) \tag{4.19}$$

and

$$C_{\ell,\nu_1\nu_2}^{\rm tSZ-2h} = g_{\nu_1} g_{\nu_2} T_{\rm CMB}^2 \int dz \frac{dV_{\rm c}}{dz}(z) \, P_{\rm DM}\big|_{k=(\ell+1/2)/\chi(z)} \left(\int dM \, \frac{dn_{\rm h}}{dM}(M,z) \, b_{\rm h}(k,M,z) \, \tilde{y}_\ell(M,z) \right)^2, \tag{4.20}$$

where g_ν is the spectral function of the tSZ effect, given, neglecting relativistic corrections, by

$$g_\nu = \left(x\frac{e^x+1}{e^x-1} - 4 \right), \text{ with } x = \frac{h_\mathrm{p}\nu}{k_\mathrm{B}T_\mathrm{CMB}}, \tag{4.21}$$

and $\tilde{y}_\ell$ is the two-dimensional Fourier transform of the Compton Y-parameter, y_3D (Komatsu & Seljak, 2002):

$$\tilde{y}_\ell = \frac{4\pi r_\mathrm{s}}{\ell_\mathrm{s}^2}\int dx x^2 y_\mathrm{3D}(x)\frac{\sin(\ell x/\ell_\mathrm{s})}{\ell x/\ell_\mathrm{s}}; \tag{4.22}$$

here $x = r/r_\mathrm{s}$, where r is radius from the centre of the (assumed spherically symmetric) halo, r_s is a scale radius, and $\ell_\mathrm{s} \equiv D_A/r_\mathrm{s}$, with $D_A = \chi/(1+z)$ the angular diameter distance to redshift z.

Note that $g_\nu < 0$ for $\nu \lesssim 217$ GHz. This means that, for certain choices of ν_1 and ν_2, the tSZ power is *negative*. This can also be the case for the tSZ×CIB contribution.

The integrated Compton Y-parameter from a single cluster (integrated over the projected area of the cluster on the sky) is given by

$$Y_\mathrm{SZ} = \frac{4\pi r_\mathrm{s}^3}{D_A^2}\int dx x^2 y_\mathrm{3D}(x). \tag{4.23}$$

Summing the contribution to the total tSZ intensity from all clusters we then have

$$I_\nu^\mathrm{tSZ} = g_\nu T_\mathrm{CMB}\int dz \frac{dV_\mathrm{c}}{dz}\int dM \frac{dn_\mathrm{h}}{dM} Y_\mathrm{SZ}. \tag{4.24}$$

4.2.3 tSZ×CIB power

We now apply the halo model to describe the tSZ×CIB cross-correlation. There is a one-halo term arising from the correlation of CIB sources with the tSZ from their host halo, but there is also a two-halo term arising from the correlation between the CIB sources in one halo and the tSZ from another. Even if we consider the extreme limit in which there is no star formation and no CIB sources in those haloes massive enough to make a non-negligible contribution to the tSZ, this second term would still exist, provided there was some overlap between the redshift distribution of the CIB sources and tSZ haloes. This is a key prediction of this work. On large angular scales, where the two-halo term dominates, the tSZ×CIB power is therefore relatively insensitive to the astrophysical processes that affect star formation in massive haloes.

We write the total tSZ×CIB power as

$$C_{\ell,\nu_1\nu_2}^{\mathrm{tSZ\times CIB}} = C_{\ell,\nu_1\nu_2}^{\mathrm{tSZ\times CIB-1h}} + C_{\ell,\nu_1\nu_2}^{\mathrm{tSZ\times CIB-2h}}. \tag{4.25}$$

In terms of the quantities defined in Sections 4.2.1 and 4.2.2, the one- and two-halo terms are

$$C_{\ell,\nu_1\nu_2}^{\mathrm{tSZ\times CIB-1h}} = T_{\mathrm{CMB}} \int dz \frac{dV_{\mathrm{c}}}{dz} \int dM \, \frac{dn_{\mathrm{h}}}{dM} \, \tilde{y}_\ell \left(g_{\nu_1} \langle S_{\nu_2} \rangle + g_{\nu_2} \langle S_{\nu_1} \rangle \right) \langle N_{\mathrm{gal}} \rangle \, u_{\mathrm{gal}} \tag{4.26}$$

and

$$C_{\ell,\nu_1\nu_2}^{\mathrm{tSZ\times CIB-2h}} = T_{\mathrm{CMB}} \int dz \frac{dV_{\mathrm{c}}}{dz} P_{\mathrm{DM}} \int dM_1 \, \frac{dn_{\mathrm{h}}}{dM_1} \, b_{\mathrm{h}} \, \tilde{y}_\ell \int dM_2 \, \frac{dn_{\mathrm{h}}}{dM_2} \, b_{\mathrm{h}} \left(g_{\nu_1} \langle S_{\nu_2} \rangle + g_{\nu_2} \langle S_{\nu_1} \rangle \right) \langle N_{\mathrm{gal}} \rangle \, u_{\mathrm{gal}}. \tag{4.27}$$

The fact that, in the non-relativistic limit, the tSZ spectral dependence is not coupled to redshift or halo mass leads to these cross-terms being simpler than would in general be the case for two source populations. While equations 4.26 and 4.27 include the tSZ and CIB contributions from both ν_1 and ν_2, an interesting case to consider is that of two widely spaced frequencies, such that one of the two terms in parentheses in equations 4.26 and 4.27 is negligible due to the different frequency dependence of the tSZ and CIB. Constraints from cross-spectra at widely-spaced frequencies may actually provide the best opportunity for detecting and constraining the tSZ×CIB term. This idea is discussed further in Sections 4.4.2 and 4.5.2.

Using this formalism, the tSZ×CIB cross-correlation power requires no additional functions or parameters over those used to characterize the tSZ×tSZ and CIB×CIB power individually. This is an advantage of the halo model approach over the template-based approach used to describe the tSZ and CIB power in R12, which requires the inclusion of a correlation coefficient ξ to specify the tSZ×CIB cross-power. Furthermore, the frequency and angular scale dependence of ξ may not be negligible, meaning fitting a single correlation coefficient may not be sufficient to describe the tSZ×CIB power (see Section 4.4.5).

4.3 Example calculation

Having laid out an analytic halo model framework for the tSZ×CIB power, we now use recent models for the CIB and tSZ to perform calculations at frequencies probed by current arcminute-resolution mm and submm telescopes: ACT, SPT, *Planck*'s High Frequency Instrument (HFI), and *Herschel*'s SPIRE instrument. We focus on 150 GHz as the band primarily used to constrain small-scale CMB anisotropy power by ACT and SPT (e.g., Hall et al., 2010; Fowler et al., 2010; Keisler et al., 2011; Dunkley et al., 2011), and cross-correlations with higher frequencies as an opportunity to potentially improve constraints on the tSZ×CIB amplitude and angular scale dependence. Specifically, we perform calculations using bandpass filters from the following frequency channels: SPT's 150 GHz (2100 μm), *Planck*'s 857, 545, 353 and 217 GHz (350, 550, 840 and 1380 μm), and SPIRE's 1200 GHz (250 μm). Predictions are also made for the ACT 148 and *Planck* 143 GHz channels.

4.3.1 CIB model

For the CIB clustering power we use the model of Xia et al. (2012 – hereafter X12). This work uses the CIB source model developed in Granato et al. (2004) and Lapi et al. (2011 – hereafter L11). Three populations of sources are considered: spiral galaxies, starbursts (these two populations contribute to the CIB for $z \lesssim 2$), and proto-spheroids (the dominant CIB sources at high redshift, which do not exist at $z < 1$). X12 perform a joint fit to angular power spectra from *Herschel*-SPIRE (Amblard et al., 2011), *Planck* (Planck Collaboration et al., 2011c) and SPT (Shirokoff et al., 2011), using a simple HOD model based on Zheng et al. (2005). There are two free parameters in the model: a minimum halo mass for hosting a proto-spheroid source, $M_{\rm min}$, and the power-law index, $\alpha_{\rm sat}$, which describes the occupation of massive haloes with additional proto-spheroids. The results in Section 4.4 are shown for $\log(M_{\rm min}/M_{\odot}) = 12.24$ and $\alpha_{\rm sat} = 1.81$, the means of the marginalized parameter distributions obtained by X12. We find that the statistical uncertainty from varying these two parameters is not significant compared to other uncertainties in the tSZ×CIB power (see Section 4.5.1).

Note that the X12 model does not include any dependence of CIB source spectral properties (luminosity, SED, etc.) on host halo mass. Consequently, the angular power spectrum is evaluated simply using equation (4.3) and the $dI_{\nu}^{\rm CIB}/dz$ predictions from L11.

4.3.2 tSZ model

For the tSZ we use the model described in Efstathiou & Migliaccio (2012 – hereafter EM12), which is based on the halo model of Komatsu & Seljak (2002), but with the empirical electron pressure profiles from recent X-ray measurements of the representative XMM-Newton cluster structure survey (REXCESS; Böhringer et al., 2007) cluster sample (Arnaud et al., 2010). The model has two free parameters: an overall amplitude, A (such that $C_\ell^{\rm tSZ} \propto A$), and an evolution parameter, ε, which describes departures from self-similar evolution of the electron pressure profile with redshift. For the calculations in Section 4.4 we fix $A = 0.95$ and $\varepsilon = 0$, which, for our choice of halo properties and bright cluster removal (see below), corresponds to $\ell(\ell+1)C_\ell^{\rm tSZ}/2\pi|_{\ell=3000} = 4\ \mu{\rm K}^2$ at 150 GHz. This is consistent with recent ACT and SPT measurements (Dunkley et al. 2011; R12). The effect of introducing departures from self-similar redshift-evolution in the electron pressure profile is discussed in Section 4.5.1.

4.3.3 Halo definition

We follow X12 in using the halo mass function from Sheth & Tormen (1999), and the associated large-scale halo bias from Sheth et al. (2001). This mass function approximates the number density of haloes as a function of halo virial mass, $M_{\rm vir}$. The electron pressure profiles of Arnaud et al. (2010) and the EM12 model are expressed not in terms of $M_{\rm vir}$, but M_{500}, defined as the mass of the region within which the mean overdensity is 500 times the critical background density at that redshift. When calculating $\tilde{y}_\ell$ we must therefore first calculate M_{500} as a function of $M_{\rm vir}$ and redshift (see, e.g., Section 2.1 of Komatsu & Seljak, 2002).

Again following X12, we set $P_{\rm DM} = P_{\rm DM}^{linear}$, and we assume that the galaxy density profile, $u_{\rm gal}$, equals that of the dark matter in an NFW halo, $u_{\rm DM}$, and that haloes are truncated at the virial radius, $r_{\rm vir}$, for the purposes of hosting CIB sources. As in EM12, however, contributions to the Compton Y-parameter are allowed out to $4r_{\rm vir}$. The effect of halo truncation radius on the tSZ and clustered CIB power spectra is not negligible (e.g., Komatsu & Seljak, 2002; Viero et al., 2009), and it is not clear that these assumptions are reasonable over the range of source populations and redshifts considered. In Section 4.5.1 we consider the effect of forcing the CIB sources to lie at least some minimum distance from the centre of their host haloes, motivated by evidence that galaxies at the centers of groups and clusters are typically undergoing less-active star formation than those lying further out (e.g., Kennicutt 1983, Hashimoto et al. 1998, Bai et al. 2006, Bai et al. 2007; see also Boselli & Gavazzi 2006 and references therein).

4.3.4 Source removal

Analyses of tSZ and CIB statistics are sensitive to the level of removal of bright resolved objects (clusters and point sources) from maps. Removal of objects down to the resolution limits of current instruments like *Herschel*-SPIRE, *Planck*, ACT and SPT has some effect on the tSZ one-halo power (e.g., Komatsu & Kitayama, 1999; Shaw et al., 2009) and the CIB shot noise (e.g., Béthermin et al., 2011), and will also affect the clustered CIB power to a lesser extent (see Section 3.3.1).

As stated, X12 use the L11 CIB source model, accounting for removal of bright CIB sources by ignoring contributions to dI_ν^{CIB}/dz from sources with flux above some threshold S_{cut}, corresponding to the resolution limit of the relevant band (50 mJy for SPIRE bands, 6.4 mJy for the SPT 150 GHz band, and various values for *Planck* – see Table 3 of Planck Collaboration et al. 2011). X12 also, somewhat arbitrarily, discount contributions to the clustered CIB power spectrum from $z < 0.25$. We do likewise for the clustered CIB and tSZ×CIB power; for the angular scales relevant for constraining the kSZ effect ($\ell \gtrsim 3000$), the effect of this truncation is probably negligible, although this may not be the case on larger angular scales (see Section 4.4.3).

We remove the brightest 0.1 clusters per square degree in our model, roughly corresponding to a level of cluster detection currently achieved in deep ACT and SPT maps (Staniszewski et al., 2009; Marriage et al., 2011b; Benson et al., 2011). We do this to eliminate the effect of any massive, highly extended cluster at $z \simeq 0$ (which, should it exist, would surely be masked in any real power spectrum analysis). The exact level of cluster removal has little effect on the tSZ×CIB power, especially for $\ell \gtrsim 3000$ (see Section 4.5.1). We define cluster brightness as the tSZ decrement integrated over the cluster's projected area. Due to effects such as the instrument beam and map filtering, this is not exactly the quantity that is measured in real maps, however, a more sophisticated treatment is beyond the scope of this work.

4.4 Results

In this section we use the equations of Section 4.2 and the tSZ and CIB models described in Section 4.3 to calculate several quantities: the redshift-dependence of the tSZ and CIB intensity, the angular power spectrum of the tSZ, clustered CIB and tSZ×CIB components for a range of frequencies, the redshift-dependence of the tSZ, clustered CIB and tSZ×CIB power, and the tSZ×CIB correlation coefficient ξ used by R12.

4.4.1 Redshift-distribution of intensity, dI_ν/dz

Figure 4.1 shows the redshift-distribution of the tSZ and CIB intensity, plotted as $d\ln I_\nu/dz$. We obtained $d\ln I_\nu^{\rm tSZ}/dz$ using equation (4.17). In these units the tSZ intensity is independent of frequency. While the tSZ effect integrated over the projected area of a cluster is independent of the cluster redshift (neglecting redshift-evolution in halo concentration), the scarcity of massive haloes at high redshift results in $z < 2$ clusters contributing the majority of the tSZ intensity.

The CIB intensity redshift-distribution is shown for two recent models (Béthermin et al. 2011 – B11, and Lapi et al. 2011 – L11) and two frequencies. Increasing ν and moving into the submm results in an increase in the relative importance of low-redshift sources as well as an increase in the total CIB intensity (not shown in Figure 4.1). This behaviour is common to other recent CIB source models (including Lagache et al., 2003; Negrello et al., 2007; Marsden et al., 2011), and arises from the thermal dust emission from CIB sources resembling a modified blackbody peaked at a rest-frame wavelength of $\sim 100\ \mu$m. In the L11 model, the peak in $dI_\nu^{\rm CIB}/dz$ at $z \simeq 1.5$ is due to starburst galaxies, whose contribution decreases rapidly at higher redshift such that for $z > 2$ the proto-spheroids are the sole contributors. The structure in the $dI_\nu^{\rm CIB}/dz$ curves arises from summing the contributions from the spiral, starburst and proto-spheroid sources; the L11 1200 GHz curve in Figure 4.1 is the sum of the three 250 μm curves plotted in Figure 3 of X12.

The overlap between the tSZ and CIB curves on this plot give some indication of the size of the tSZ×CIB cross-correlation, although, as shown in equations 4.26 and 4.27, the cross-power also depends on other factors, for instance the extent to which bright CIB sources occupy massive haloes for the one-halo term, and the effective redshift window function introduced by $P_{\rm DM}$ for the two-halo term.

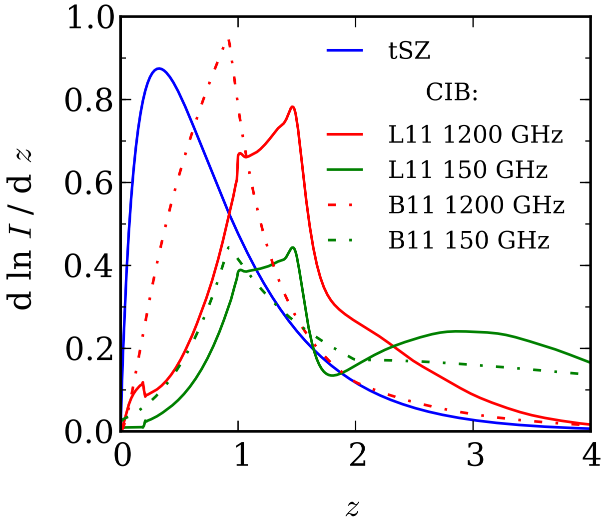

Figure 4.1: Redshift-distribution of tSZ and CIB intensity. The tSZ intensity distribution is calculated from the model of Efstathiou & Migliaccio (2012) and, in these units, is independent of frequency. We show the CIB intensity distribution at 150 and 1200 GHz predicted by Béthermin et al. (2011 – B11) and Lapi et al. (2011 – L11). The overlap between the tSZ and CIB curves gives an indication of the size of the tSZ×CIB cross-correlation. The degree of correlation increases for higher CIB frequencies because $dI_\nu^{\rm CIB}/dz$ becomes increasingly concentrated to low redshift.

Consider cross-correlating a map at a fixed frequency where the tSZ makes a significant contribution (e.g., 150 GHz) with maps at higher frequencies. Figure 4.1 suggests that the degree of tSZ×CIB cross-correlation will *increase* as the frequency of the second map increases (at least up to 1200 GHz). However, the degree of CIB×CIB correlation will *decrease* as $dI_\nu^{\rm CIB}/dz$ in the second map becomes more concentrated to low redshift. We therefore expect the importance of the tSZ×CIB contribution relative to the cross-spectrum CIB power to increase as the separation of the two map frequencies increases. This is illustrated in Section 4.4.2, below.

The Béthermin et al. (2011) CIB model predicts far more low-redshift flux than that of L11. The results in Section 4.4 follow X12 and use the L11 predictions, however we consider the effect of redistributing some of the high-redshift flux to lower redshift on the tSZ×CIB power in Section 4.5.1.

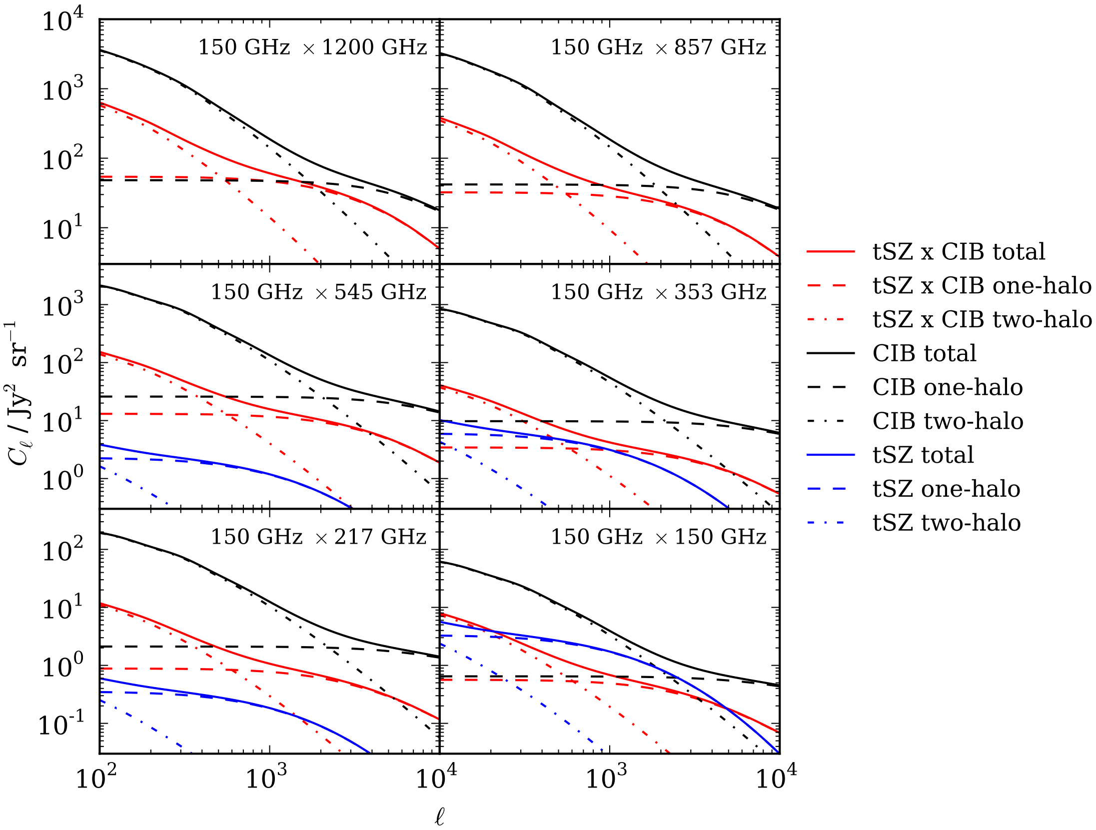

Figure 4.2: Angular power spectrum from the tSZ×CIB correlation predicted for cross-correlating a map at 150 GHz with maps at various other frequencies using the model described in Sections 4.2 and 4.3. The CIB power here is clustered CIB power only (the Poisson shot noise power is not shown). Note that the tSZ×CIB cross-power component is negative for each case shown here, while the tSZ power is negative in each case except 150 × 150 GHz. The importance of the tSZ×CIB contribution increases relative to the CIB contribution as the frequency separation increases because the CIB becomes more concentrated to low redshift at higher frequencies, increasing the overlap with the tSZ clusters (see Figure 4.1). The tSZ×CIB component is uncertain by a factor of two to three; to avoid cluttering the figure we do not show uncertainty estimates here, but see discussion in Section 4.5.1.

4.4.2 tSZ×CIB angular power spectrum

Figure 4.2 shows the clustered CIB, tSZ and tSZ×CIB contributions to the angular power spectra from cross-correlating a 150 GHz map with maps at a range of higher frequencies. Note that the CIB Poisson shot noise is not shown because it is not yet well-constrained by data for the widely-spaced bands. Several features are apparent in these plots. Firstly, as expected, the size of the tSZ×CIB power relative to the clustered CIB power generally increases as the frequency separation of the maps increases. The 150×353 and 150×150 GHz spectra are exceptions to this trend because both terms in parentheses in equations 4.26 and 4.27 are significant (in the other spectra, one of the two terms is highly sub-dominant). In the 150×353 GHz spectrum, the contribution from the tSZ in the 353 GHz map correlating with the CIB sources in the 150 GHz map acts to 'fill in' around 10% of the 150 tSZ × 353 CIB power, since the tSZ effect in the two maps has opposite signs. In the 150×150 GHz spectrum, the significant presence of both tSZ and CIB fluctuations in the map acts constructively and leads to a larger tSZ×CIB component (relative to clustered CIB).

All three components shown in Figure 4.2 consist of one- and two-halo terms. As stated earlier, the scarcity of massive clusters means the two-halo tSZ power is sub-dominant over the whole range of angular scales shown (although masking more bright clusters would increase the relative importance of the two-halo term). For the X12 CIB clustering model, the tSZ×CIB one-halo power dominates the two-halo power at significantly larger scales than for the clustered CIB. This is mainly because:

(i) the low-redshift spirals and starbursts responsible for two thirds of the tSZ×CIB cross-correlation power (compared to a third or less of the CIB power) are hosted in low-mass, and hence low-bias, haloes (reducing the two-halo power – see equation 4.27), and

(ii) there is no mechanism to limit the star formation or CIB source emissivity in massive haloes in the X12 model, possibly leading to an overestimation of the one-halo tSZ×CIB power.

The relationship between CIB source emissivity and halo mass, and the modelling of the CIB clustering, are the largest sources of uncertainty in our tSZ×CIB power calculation (see Section 4.5.1).

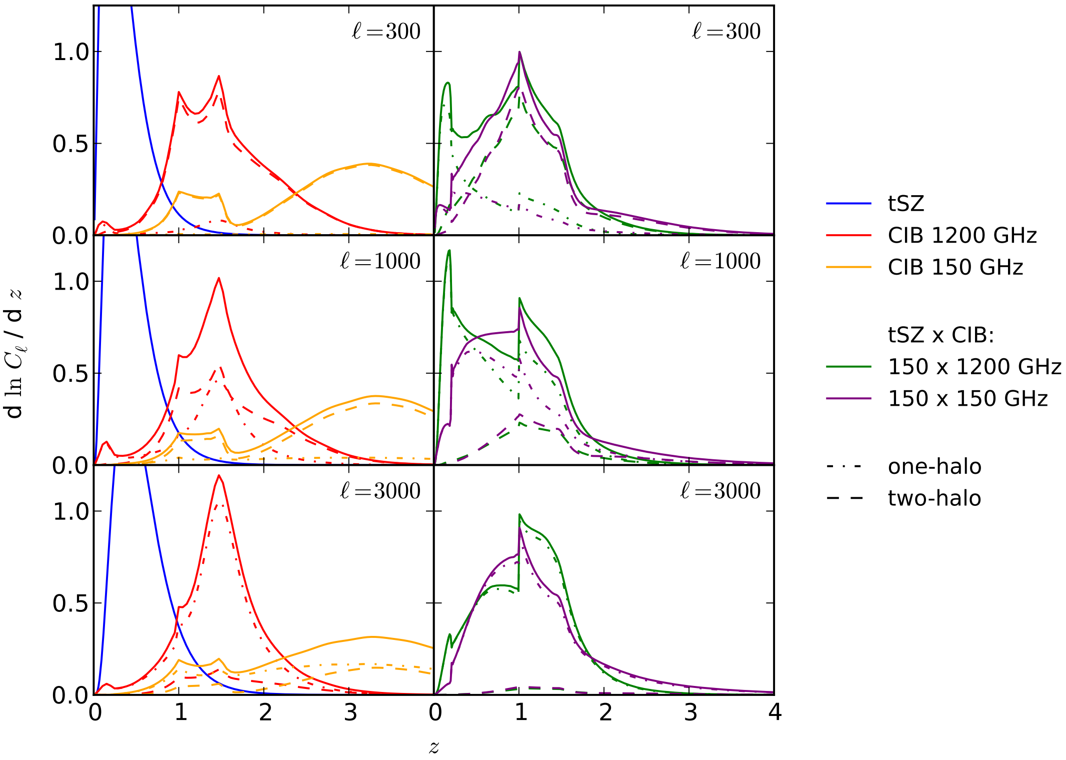

Figure 4.3: Redshift-distribution of the angular power spectrum, $d\ln C_\ell/dz$, for the tSZ and clustered CIB components (left panels; compare with $d\ln I/dz$ in Figure 4.1) and the tSZ×CIB component (right panels). While the redshift-distribution of clustered CIB power changes significantly from 1200 to 150 GHz, that of the tSZ×CIB power is fairly similar. The complex structure in $d\ln C_\ell^{\mathrm{tSZ}\times\mathrm{CIB}}/dz$ is due to the existence of three different populations of CIB sources in our adopted CIB source model (Lapi et al., 2011). Xia et al. (2012) find that the clustering properties of the $z < 1$ CIB sources, which make a significant contribution to the tSZ×CIB power, are not constrained by angular power spectra of CIB fluctuations from *Herschel*-SPIRE, *Planck* and SPT, meaning that the low-z tSZ×CIB power is highly uncertain (see Section 4.5.1).

4.4.3 Redshift-distribution of power, dC_ℓ/dz

Figure 4.3 shows the redshift-distribution of power, plotted as $d\ln C_\ell/dz$, for the tSZ, clustered CIB and tSZ×CIB components. Comparing the left-hand panels with Figure 4.1, the tSZ power and intensity have similar redshift distributions, as do the clustered CIB power and CIB intensity at 1200 GHz. The distribution of clustered CIB power at 150 GHz (particularly the two-halo power) is concentrated to higher redshifts than the intensity, with only a small contribution from the peak in dI/dz at $z \leq 1$. In the X12 model, the proto-spheroid sources that contribute all the CIB at $z > 2$ are hosted in massive haloes, which at these redshifts are highly biased (increasing the importance of these sources for contributing to the two-halo CIB power but not the intensity).

The redshift-distribution of the tSZ×CIB power shows considerably less frequency dependence than that of the clustered CIB power. This is because most tSZ clusters lie at $z < 2$ where, according to the Lapi et al. (2011) model, the CIB sources are predominantly starbursts, and the shape of dI_ν^{CIB}/dz is fairly similar for the range of frequencies considered here (Figure 4.1). The peak at $z \simeq 0.15$ in the right-hand panels of Figure 4.3 is due to local spiral galaxies in the Lapi et al. (2011) model. The sharp step at $z = 1$ occurs because the high-redshift proto-spheroid population comes into existence discontinuously; while unrealistic, this feature does not affect our analysis because the power spectrum remains smooth and the redistribution of sources required to achieve a gradual transition in dC_ℓ/dz will induce a small change in the tSZ×CIB power compared to other modelling uncertainties (see Section 4.5).

4.4.4 Comparison to primary CMB and other foregrounds

Figure 4.4 shows the most recent 150 GHz ACT and SPT power spectra (Das et al. 2011; R12), with contributions from primary and secondary CMB temperature anisotropies and foregrounds overplotted. The tSZ×CIB power is a sub-dominant component but may be comparable to the kSZ at $\ell \gtrsim 3000$. Note that the kSZ power shown in the figure includes the contribution from bulk electron motion in galaxy clusters and the intergalactic medium but assumes instantaneous reionization; including the effect of patchy reionization would increase this signal. Since the tSZ×CIB power is negative for the principal CMB channels of ACT, SPT and *Planck*, we would expect uncertainty in the tSZ×CIB power to degrade constraints on the upper limit of the kSZ.

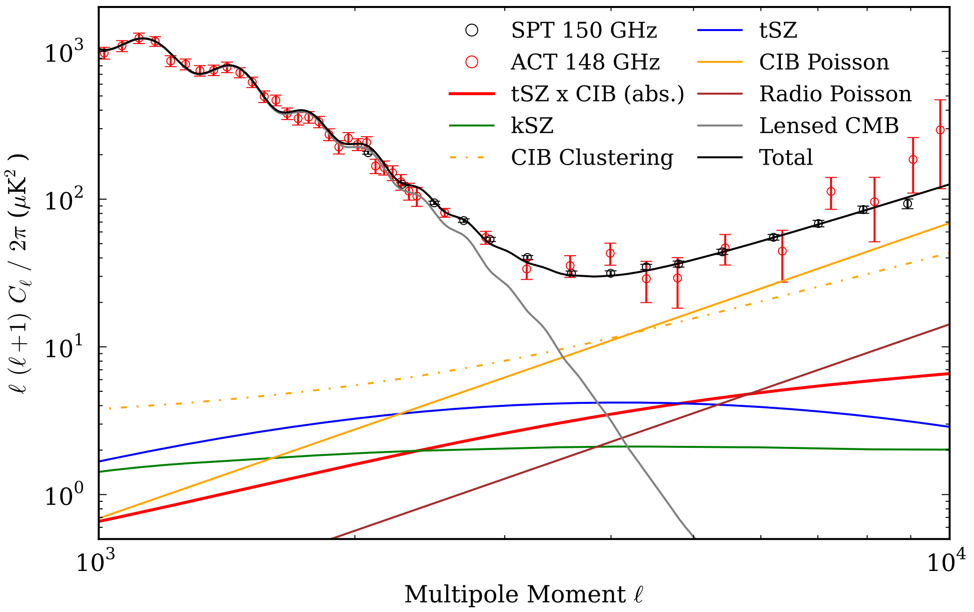

Figure 4.4: Comparison of power spectra of primary and secondary CMB temperature anisotropies and foregrounds at 150 GHz. The data points are the latest SPT (Reichardt et al. 2011; R12) and ACT (Das et al., 2011a) measurements; we simply overplot the various power spectrum components here rather than performing a fit to these data. The CIB clustering power was reproduced from the model of Xia et al. (2011; X12), as described in Section 4.3.1. The tSZ power spectrum was obtained from the model described in Efstathiou & Migliaccio (2012; EM12), fixed to have $\ell(\ell+1)C_\ell^{\rm tSZ}/2\pi|_{\ell=3000} = 4\ \mu{\rm K}^2$ (see Section 4.3.2), and the tSZ×CIB power, which is negative at 150 GHz, was calculated by combining the X12 and EM12 models, as described in Sections 4.2 and 4.3. We show the kSZ power calculated in Sehgal et al. (2010). Radio and CIB point source shot noise levels were taken from R12 and X12 respectively (the ACT data points have been corrected to account for the difference in radio source shot noise levels due to more sources being masked by SPT). The primary lensed CMB power was calculated assuming a standard ΛCDM cosmology consistent with *WMAP*-7 constraints (Komatsu et al., 2011).

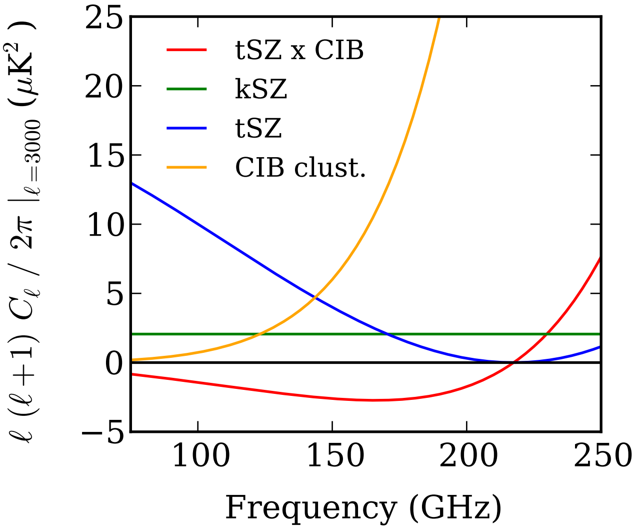

Figure 4.5: Frequency dependence of the tSZ×CIB and kSZ power. The frequency dependence of the tSZ and clustered CIB power are shown for comparison; these signals are individually easy to distinguish from a blackbody but the tSZ×CIB power has a frequency scaling that is very similar to that of the blackbody kSZ over the range of frequencies probed by ACT and SPT.

In principle, the tSZ×CIB and kSZ components could be separated on the basis of their frequency dependence, however, we find that the frequency dependence is actually very similar across much of the frequency range probed by ACT and SPT. Figure 4.5 shows the frequency dependence of the tSZ, clustered CIB, tSZ×CIB and kSZ power. The tSZ and clustered CIB power are – individually – easily distinguishable from a blackbody, however the tSZ×CIB closely resembles a blackbody (horizontal line) for $\nu < 200$ GHz. This will further worsen kSZ constraints, and indeed R12 find that the kSZ upper limit is increased by more than a factor of two when the tSZ×CIB correlation is allowed, despite using data from all three SPT channels.

To assist in the analysis of small-scale CMB data, we have made the tSZ×CIB curve from Figure 4.4 available to download[a].

4.4.5 Correlation coefficient

While, as mentioned, an advantage of the halo model approach is that there is no need for introducing a cross-correlation parameter into our model, quantifying the size of the tSZ×CIB cross-correlation

---

[a] http://www.physics.ox.ac.uk/users/AddisonG/

as a function of frequency and angular scale with such a parameter is worthwhile for the purposes of comparison with other models. R12 and Zahn et al. 2012 (2012, hereafter Z12) define a correlation coefficient, ξ_ℓ, as

$$\xi_\ell = \frac{C_{\ell,\nu_1\nu_2}^{\mathrm{tSZ}\times\mathrm{CIB}}}{\sqrt{C_{\ell,\nu_1\nu_1}^{\mathrm{tSZ}} C_{\ell,\nu_2\nu_2}^{\mathrm{CIB}}} + \sqrt{C_{\ell,\nu_2\nu_2}^{\mathrm{tSZ}} C_{\ell,\nu_1\nu_1}^{\mathrm{CIB}}}}. \tag{4.28}$$

Note that $C_{\ell,\nu_1\nu_2}^{\mathrm{CIB}}$ here includes both the Poisson and clustered CIB components. When any ℓ-dependence is neglected, R12 find $\xi = -0.18 \pm 0.12$ using SPT data at 95, 150 and 220 GHz. Z12 combine the tSZ model of Shaw et al. (2010) with the various CIB source models presented in Shang et al. (2012), and find $-0.02 > \xi_{3000} > -0.34$, with ξ_ℓ decreasing on larger angular scales (see Figure 3 in Z12).

Table 4.1 lists the values of ξ_ℓ at ℓ of 1000, 3000, 5000 and 9000 predicted from the X12 and EM12 models for cross-correlating a 150 GHz map with maps at the other frequencies shown in Figure 4.2. For the CIB Poisson shot noise levels, we follow X12 and use values of 6106, 4931, 1425, 175, 11 and 0.72 $\mathrm{Jy}^2\ \mathrm{sr}^{-1}$ at 1200, 857, 545, 353, 217 and 150 GHz, respectively. We do not attempt to quantify the uncertainty in ξ_ℓ (but see discussion of power spectrum uncertainties in Section 4.5.1). The $\sim$20% correlation obtained for 150×150 and 150×217 GHz is consistent with the findings of R12, and suggests that ξ_ℓ is not strongly dependent on frequency across the ACT and SPT bands. Physically this arises because the CIB is highly coherent at mm wavelengths, meaning that $C_\ell^{\mathrm{tSZ}\times\mathrm{CIB}}$ and $\sqrt{C_\ell^{\mathrm{CIB}}}$ in equation (4.28) have a very similar frequency scaling.

It seems doubtful that a single correlation coefficient is sufficient to parametrize the tSZ×CIB power for joint fitting to mm×mm and mm×submm spectra. Table 4.1 shows an increase in ξ_ℓ of up to a factor of two for 150×1200 GHz compared to 150×150 GHz, which arises because the CIB redshift-distribution changes, becoming more concentrated to low-redshift, in the submm bands (Figures 1 and 3).

Including the Poisson, as well as clustered, CIB power in equation (4.28) is unsatisfactory since rare, bright CIB sources may make a significant contribution to the Poisson power but be almost wholly irrelevant for the tSZ×CIB. This could be the case in the mm bands if, for instance, much of the Poisson power comes from the luminous proto-spheroids predominantly in $M \sim 10^{12.5-13}\ \mathrm{M}_\odot$ haloes at $z \gtrsim 1.5$ (as in Lapi et al., 2011). Table 4.2 shows our predictions for ξ_ℓ if we take C_ℓ^{CIB} in equation (4.28) to be the clustered CIB power only, as in Shirokoff et al. (2011). Unfortunately, due to the different ℓ-dependence

Table 4.1: Degree of tSZ×CIB cross-correlation, ξ_ℓ, for cross-correlating a 150 GHz map with maps at various frequencies

ℓ	SPIRE 1200 GHz	*Planck* 857 GHz	*Planck* 545 GHz	*Planck* 353 GHz	*Planck* 217 GHz	150 GHz[†]
1000	-0.27	-0.20	-0.14	-0.09	-0.11	-0.12
3000	-0.34	-0.26	-0.20	-0.14	-0.15	-0.17
5000	-0.35	-0.28	-0.22	-0.16	-0.16	-0.18
9000	-0.33	-0.28	-0.24	-0.17	-0.17	-0.18

[†] calculated with SPT 150 GHz bandpass filter; multiply values in this column by 1.1 or 1.15 for ACT 148 and *Planck* 143 GHz bands respectively

Table 4.2: As Table 4.1 but with excluding the Poisson shot noise CIB power in equation (4.28) – considering only clustered CIB

ℓ	SPIRE 1200 GHz	*Planck* 857 GHz	*Planck* 545 GHz	*Planck* 353 GHz	*Planck* 217 GHz	150 GHz
1000	-0.30	-0.22	-0.15	-0.10	-0.12	-0.13
3000	-0.44	-0.36	-0.27	-0.18	-0.22	-0.23
5000	-0.51	-0.43	-0.33	-0.23	-0.26	-0.26
9000	-0.60	-0.52	-0.40	-0.28	-0.30	-0.29

of the tSZ, clustered CIB and tSZ×CIB power, this leads to an increase in the ℓ-dependence of ξ_ℓ.

Our results suggest that the frequency and angular scale dependence of ξ may not be negligible, although further work is required to assess the extent to which fitting for a single correlation coefficient may bias other parameters.

4.5 Discussion

4.5.1 Sources of uncertainty in tSZ×CIB power

Numerous sources of uncertainty in the tSZ×CIB power are discussed below. Overall, we find that the contribution to the total tSZ×CIB amplitude uncertainty is around a factor of two from uncertainties in the CIB modelling, tens of per cent from the tSZ treatment, and 10% or less from other uncertainties.

CIB modelling

Two key assumptions in the X12 model are that (i) there is no connection between halo mass and CIB source spectral properties, and (ii) the clustering of CIB sources can be described by the following parameters: $\{M_{\rm min}$, $M_{\rm sat}$, $\sigma(\log_{10}M)$,$\alpha_{\rm sat}\}$, the parameter space that has been used to perform fits to angular correlation function measurements of (for instance) LRGs and SDSS galaxies (Zheng et al., 2005; Zehavi et al., 2011). What kind of uncertainty could be introduced in our tSZ×CIB calculation if these assumptions are incorrect? This is a difficult question to answer without re-fitting to the angular power spectra used by X12 with different assumptions and parameters. Here we attempt to quantify the uncertainty with several simple examples, focussing on the 150×150 GHz spectrum on angular scales of $\ell \simeq 3000$, most relevant for attempts to constrain the kSZ power.

Firstly, we note that 60% of the tSZ×CIB power comes from haloes of mass over $10^{14}\ M_\odot$, compared to only 10% of the clustered CIB×CIB. If star formation and far-infrared dust emission in these massive haloes is strongly suppressed compared to in less dense environments then the one-halo tSZ×CIB power could be lower by a factor of two with little impact on the clustered CIB power.

Secondly, X12 find $\alpha_{\rm sat} = 1.81 \pm 0.04$ for the proto-spheroid sources that dominate the clustered CIB power spectra; a preference for $\alpha_{\rm sat} > 1$ has also been reported in previous (similar) CIB clustering analyses (e.g., Amblard et al., 2011; Planck Collaboration et al., 2011c), corresponding to the number of sources occupying a massive halo somehow increasing faster than the mass of the halo. This relation is not generally supported by simulations or analyses of clustering properties of other source populations, which favour $\alpha_{\rm sat} \leq 1$ (e.g., Kravtsov et al., 2004; Zheng et al., 2005; Reid & Spergel, 2009; White et al., 2011; Zehavi et al., 2011). We consider the possibility that the HOD parameters used for the CIB analyses, while capable of yielding a good fit to the angular power spectra, do not actually describe the true source properties, and that in fact $\alpha_{\rm sat} \simeq 1$. Setting $\alpha_{\rm sat} = 1$ causes the clustered CIB power to *increase* by ~30%, but the tSZ×CIB power to *decrease* by 20%, because reducing $\alpha_{\rm sat}$ for fixed $dI_\nu^{\rm CIB}/dz$ leads to more of the CIB contribution (both intensity and power) coming from low-mass haloes. This suggests that an inaccurate or incomplete HOD model may, potentially, be causing an overestimate of the tSZ×CIB at the tens of per cent level.

The results in Section 4.4 assume that CIB sources trace the dark matter density distribution in their host haloes within one virial radius (with the first, 'central', source sitting at the very centre of the halo), as in X12. If we force all the CIB sources to lie at radii r satisfying $0.5 < r/r_{\rm vir} < 1.0$ (though still tracing the dark matter), the clustered CIB×CIB power at $\ell = 3000$ decreases by only a few percent compared to 16% for the tSZ×CIB power. With a more extreme exclusion of CIB sources from the central parts of haloes, such that $1.0 < r/r_{\rm vir} < 2.0$, the clustered CIB×CIB power decreases by 15% and the tSZ×CIB power by almost 60%.

As shown in Figure 4.1, there is significant scatter in the low-redshift CIB flux predicted by current CIB source models. We find that increasing the L11 low-redshift spiral and starburst flux by 50% (with a rescaling of the proto-spheroid flux such that the 150 GHz clustered CIB power at $\ell = 3000$ is unchanged) leads to a 30% increase in the tSZ×CIB power. If the low-redshift source flux contribution is instead doubled (again with a rescaling of the proto-spheroid flux), the tSZ×CIB power increases by some 60%.

We finally note that X12 treat the spiral and starburst sources (SS) and the proto-spheroid (PS) sources completely independently. In fact, since both populations exist for $1 < z < 2$ (see Figure 3 of X12), with a significant overlap mass-wise in their host haloes, there should also be SS×PS contributions to both the one- and two-halo clustered CIB power, which X12 do not include in their fitting.

tSZ modelling and data

The amplitude of the measured tSZ power spectrum is currently uncertain at the 10–30% level, depending on what is assumed about, for instance, the kSZ component (Dunkley et al., 2011, R12). This corresponds to a smaller uncertainty in the amplitude of the tSZ×CIB power, which is subdominant to the CIB modelling uncertainty discussed above.

As stated, the parameter ε in the EM12 model describes departure from self-similar redshift evolution of the cluster electron pressure profile. Planck Collaboration et al. (2011d) find $\varepsilon = 0.66 \pm 0.52$ for a combined sample of clusters from *Planck* and the Meta-Catalogue of X-ray detected Clusters (MCXC) at $z < 1$ (see their equation 8 and Table 6, and also Section 2 of EM12). Holding the amplitude of the tSZ power at $\ell = 3000$ fixed, we find a reduction in $C_{\ell=3000}^{\rm tSZ\times CIB}$ of $\sim$15 and 30% for $\varepsilon = 0.5$ and 1.0 respectively, compared to the $\varepsilon = 0$ case. Note that holding $C_{\ell=3000}^{\rm tSZ}$ fixed requires setting the amplitude parameter $A = 1.24$ and 1.58 for $\varepsilon = 0.5$ and 1.0 respectively. This redshift-evolution uncertainty is probably the largest source of uncertainty in our tSZ×CIB model after the CIB modelling discussed above.

The results in Section 4.4 are shown with the brightest 0.1 deg^{-2} clusters removed. For our adopted cosmology and halo definitions, this level of removal mainly affects power on large angular scales, with a negligible effect in the tSZ and tSZ×CIB power at $\ell \geq 3000$ (consistent with the findings of Shaw et al., 2009). We investigate the effect of removing ten times more clusters (1.0 deg^{-2}) and find that, while the tSZ×tSZ power is reduced by almost a factor of two at $\ell = 3000$, $C_\ell^{\text{tSZ}\times\text{CIB}}$ decreases by only $\sim$10%. As might be expected, removing more bright clusters increases the size of the tSZ×CIB power compared to the tSZ.

Other uncertainties

(i) Relativistic corrections and bulk motion of cluster electrons are expected to modify the tSZ power by $\sim$10% (e.g., Nozawa et al., 1998, 2006), and will have a reduced effect on the tSZ×CIB power.

(ii) Statistical uncertainty in proto-spheroid clustering parameters from X12 contributes a 10% uncertainty at $\ell = 3000$ in the clustered CIB power (inducing an uncertainty of $\sim$5% in the tSZ×CIB power), mainly due to the measured power spectra becoming dominated by shot noise on small scales. This measurement uncertainty is currently significantly smaller than the CIB modelling uncertainty discussed above.

(iii) Uncertainty in ΛCDM cosmological parameters: the tSZ effect depends very strongly on σ_8 – $C_{\ell=3000}^{\text{tSZ}} \propto \sigma_8^{\sim 8}$ in our model ($C_{\ell=3000}^{\text{tSZ}\times\text{CIB}} \propto \sigma_8^{\sim 6}$); we find that changing σ_8 by 0.03 (corresponding to the 1σ *WMAP*-7 uncertainty; Komatsu et al., 2011) leads to a $\sim$20% change in the tSZ×CIB amplitude, however, if the tSZ amplitude is held fixed, $C_{\ell=3000}^{\text{tSZ}\times\text{CIB}}$ changes by $< 10\%$. If a standard cosmology is assumed, uncertainty in cosmological parameters is not currently a dominant source of tSZ×CIB uncertainty.

(iv) We have not investigated varying halo properties (e.g., mass function, concentration, or introducing scale-dependent or stochastic halo bias). We postpone assessing the impact of uncertainties in these quantities on the tSZ×CIB power to future work given the size of the CIB modelling uncertainties discussed above.

4.5.2 Future data

Angular power spectra from mm and submm maps

Our results show that the contribution of the tSZ$\times$CIB power relative to the clustered CIB plus tSZ power increases for cross-correlating mm and submm maps with widely-spaced frequencies (Figure 4.2). Cross-correlating ACT and Balloon-borne Large-Aperture Submillimeter Telescope (BLAST; observations at 600, 860 and 1200 GHz) maps of an 8.6 deg^2 area of sky near the south ecliptic pole revealed a significant detection of cross-spectra clustered CIB power (Chapter 2), however the small sky area means these data are unable to provide constraints on the tSZ$\times$CIB power. Imminent *Herschel*-SPIRE observations, also at 600, 860 and 1200 GHz, will provide $\sim$100 deg^2 of overlap with existing ACT[b][c] and SPT[d] fields (as well as upcoming ACTPol and SPTpol fields), which should allow us to improve constraints on the CIB and tSZ$\times$CIB correlations.

In Section 4.4 we showed results calculated using the SPT 150 GHz bandpass filter. Since the CIB intensity and clustered power amplitude are falling off very steeply with decreasing frequency in the mm-bands (e.g. Fixsen et al., 1998; Planck Collaboration et al., 2011c), the contribution to the power spectrum from clustered CIB sources is $\sim$20% lower in the ACT 148 GHz channel (Table 3.2). This means that the tSZ$\times$CIB power in the ACT 148 GHz $\times$ SPIRE cross-spectra will be around 10% larger relative to the CIB$\times$CIB contribution compared to in SPT 150 GHz $\times$ SPIRE. The SPT 95 GHz channel is also potentially well-suited to constraining the tSZ$\times$CIB signal; the ratio of the tSZ$\times$CIB to the CIB power in SPT 95 GHz $\times$ SPIRE spectra will be some five times larger than for SPT 150 GHz $\times$ SPIRE, based on the frequency scaling of the tSZ and clustered CIB (see Chapter 3 and R12). Cross-correlations of mm and submm *Planck* High- and Low-Frequency Instrument channels (e.g., 70$\times$857 GHz, 100$\times$857 GHz) may also be of use for constraining the tSZ$\times$CIB power for $\ell \lesssim 2500$. Which channels give the best constraints in practice will also depend on the amount of noise in the maps and the size of the Poisson CIB power.

---

[b] http://herschel.esac.esa.int/Docs/AO2/GT2_accepted.html#GT2_mviero_1

[c] http://herschel.esac.esa.int/Docs/AO2/OT2_accepted.html#OT2_mviero_2

[d] http://herschel.esac.esa.int/Docs/AO1/OT1_accepted.html#OT1_jcarls01_3

Other statistics

The angular power spectrum of mm and submm maps is not the only statistic with the ability to explore the connection between clusters and CIB sources. Other measurements that may also provide insight include:

(i) cross-correlations of CIB-dominated maps with X-ray cluster maps (either stacking analyses or power spectrum based),

(ii) targeted imaging of clusters in submm bands (using, e.g., *Herschel*, Submillimetre Common-User Bolometer Array-2 – SCUBA-2[e] – and ALMA) – this will improve constraints on the spatial distribution of CIB sources within massive haloes, which enters into our modelling through $u_{\rm gal}$, and

(iii) cross-correlations of CIB maps with catalogues of objects at well-measured redshifts (e.g., LRGs, quasars) – this will improve constraints on $dI_\nu^{\rm CIB}/dz$, particularly at $z < 1$, most relevant for the tSZ×CIB power; ACT, *Herschel*, ACTPol and *Planck* (as well as, e.g., IRAS at higher frequencies) have – or will have – the overlap with optical surveys required for these studies.

4.6 Conclusions

We have presented equations describing the contribution to the angular power spectrum from the correlation of tSZ clusters and CIB sources in a halo model framework. We then used these equations to calculate the tSZ×CIB power spectrum at 150 GHz and for a range of cross-spectra using recent tSZ and CIB halo models. We find that:

(i) The tSZ×CIB is a sub-dominant component of the angular power spectrum at 150 GHz, contributing approximately $-2\ \mu{\rm K}^2$ at $\ell = 3000$; uncertainty in the tSZ×CIB power will degrade kSZ constraints, as found in recent SPT analysis (R12, Z12), due to the similarity in their frequency dependence.

---

[e] http://www.roe.ac.uk/ukatc/projects/scubatwo/index.html

(ii) The size of the tSZ×CIB power relative to the clustered CIB power increases if we correlate mm and submm maps with increasing frequency separation (at least up to 1200 GHz, the highest frequency *Herschel*-SPIRE channel).

(iii) Uncertainty in the amplitude of the tSZ×CIB power is currently a factor of two or three, with the uncertainty dominated by uncertainty in modelling of the clustering of CIB sources (although there are other significant sources of uncertainty, including possible evolution in cluster electron pressure profiles with redshift).

The framework laid out in Section 4.2 may be used to perform joint fitting to ACT, SPT, *Herschel*, *Planck* and other data sets. The halo model and HOD formalisms are not without their complications, and work remains in order to find the best way to parametrize the connection between CIB sources and their haloes; it seems essential that a thorough exploration of modelling assumptions accompany future analysis.

Detection of the tSZ×CIB power in mm×submm cross-spectra may enable us to constrain the tSZ effect from unresolved clusters in spectra that are free from the signal of the primary CMB (although the CMB fluctuations will still exist as noise in the mm maps). Whether this can lead to improved tSZ constraints over mm-band data alone will depend on the true size of the tSZ×CIB signal and future improvements in the modelling of the CIB sources.

We finally remark that the tSZ×CIB power may be a significant contaminant for detection of signals beyond the kSZ, for example, detection of the Integrated Sachs-Wolfe effect by cross-correlating mm-band CMB maps with tSZ or CIB maps (Taburet et al., 2011; Ilić et al., 2011).

Chapter 5

Constraining the properties of dusty, star-forming galaxies with the angular power spectrum of cosmic infrared background anisotropies

5.1 Introduction

In this chapter, we perform a joint fit to deep differential number counts from *Herschel*-SPIRE at 250, 350 and 500 μm (1200, 860 and 600 GHz), counts from the Multiband Imaging Photometer for Spitzer (MIPS; Werner et al., 2004) at 70 and 160 μm (4300 and 1900 GHz), and angular power spectra covering degree to arcminute scales from 250 μm to 1.4 mm (1200 to 220 GHz) from SPIRE, *Planck*, ACT and SPT. We simultaneously constrain the bolometric dust luminosity function and its evolution, the source spectral energy distributions (SEDs), and the source clustering properties of dusty CIB galaxies. We require that our model successfully reproduces not only the clustered power in the power spectrum, but also the Poisson, shot-noise, power. Thanks to this joint analysis, we are able to demonstrate the ability of the angular power spectrum to provide constraints on the SEDs of the numerous, faint, unresolved CIB sources, in addition to developing a model with considerable predictive power.

Many recent dusty galaxy anisotropy analyses have interpreted angular power spectra using the halo model in conjunction with a parametric halo occupation distribution (H.O.D.; see Section 1.3 and Chapter 4) prescription (Viero et al., 2009; Amblard et al., 2011; Planck Collaboration et al., 2011c; Shang et al., 2012; Xia et al., 2012; De Bernardis & Cooray, 2012). In this approach, all CIB sources inhabit collapsed dark matter haloes, and the clustered source contribution to the angular power spectrum arises from correlations between objects in the same halo ('one-halo' term, dominant on small angular scales) or different haloes ('two-halo' term, dominant on large angular scales). The abundance and bias of these haloes, typically inferred from large N-body simulations, is used to calculate the contribution of the clustered dusty sources to the angular power spectrum, rather than directly dealing with the dusty source bias. The analyses listed above make a number of assumptions, including:

(i) the halo bias (relative to the linear theory dark matter power spectrum) may be taken as independent of scale when calculating the two-halo term, and

(ii) the spatial distribution of the dusty sources within their host halo follows the halo mass density profile, truncated at the virial radius.

Cooray & Sheth (2002) suggested using the halo bias with respect to the linear matter power spectrum in the two-halo term as a crude way to prevent overestimating the two-halo power on scales where the non-linear matter power spectrum would begin to receive contributions from within a single halo (since galaxies in a single halo are supposed to be accounted for in the one-halo term). Several more recent analyses have found that, in fact, the halo bias with respect to the linear matter power increases with scale for $k \gtrsim 0.1h$ Mpc^{-1}, both at low and high redshift (e.g., Cole et al., 2005; Tinker et al., 2005; Yoo et al., 2009; Fernandez et al., 2010; Tinker et al., 2012; Mandelbaum et al., 2012). Wavevector $k \simeq 0.1h$ Mpc^{-1} corresponds to multipole moment ℓ of several hundred at redshift $z \sim 1-2$, where much of the CIB anisotropy signal in the far-infrared and longer wavelengths originates. The two-halo term dominates the one-halo on these angular scales, only becoming subdominant at $\ell > 750$ (Amblard et al., 2011; Planck Collaboration et al., 2011c; Shang et al., 2012; Xia et al., 2012), even when only the linear matter power spectrum is used in the two-halo term. This suggests that, if the scale dependence of the halo bias is neglected, either power over a range of scales may be wrongly attributed to the one-halo term, or the inferred redshift distribution of the dusty sources will be altered, in either case likely biasing the inferred H.O.D. parameters and characteristic halo mass scales.

The angular scale dependence of the one-halo term is determined by the Fourier transform of the spatial distribution of sources within haloes (sometimes called $u_{\rm gal}$). Setting $u_{\rm gal} = u_{\rm DM}$, the Fourier space density profiles of a spherical NFW (Navarro et al., 1996) halo, truncated at the virial radius, is a convenient choice, but there is no evidence that it is an accurate reflection of the distribution of dust-dominated sources. There is, indeed, considerable evidence that galaxies near the center of groups and clusters, where the NFW dark matter density profile peaks, are forming stars less actively than those closer to the outskirts (e.g., Kennicutt 1983, Hashimoto et al. 1998, Bai et al. 2006, Bai et al. 2007; also Boselli & Gavazzi 2006 and references therein). These systems are relevant for the calculation of the one-halo power, which receives no contribution from smaller haloes hosting a single galaxy, and allowing the CIB sources to lie further from the center of their halo than a virial radius has a non-negligible effect on the one-halo power at scales of a few arcminutes (Viero et al., 2009, and Section 4.5.1).

It should be noted that the above issues are related to how the halo model is implemented rather than being limitations of the formalism itself. It is not clear, however, that quantifying the uncertainties induced in the halo model calculations by scale-dependent halo bias or alternative spatial distributions of dusty sources in haloes may be straightforwardly accomplished. It is also unclear that quantities such as the halo mass function, large-scale halo bias, and halo concentration, are sufficiently well known at $z \gtrsim 2$ that their uncertainties may be safely neglected, given the excellent signal-to-noise of current and future SPIRE and *Planck* measurements. For these reasons, we do not attempt a halo model analysis in this work. While we are not able to directly extract (for instance) characteristic mass scales for haloes hosting dusty sources, we argue that, for the reasons discussed, existing halo model analyses of angular power spectra in the FIR and longer wavelengths do not necessarily provide robust constraints on these quantities either.

This work could be considered an extended version of the analysis presented in Chapter 3, constraining a more physically motivated model using higher quality spectra, as well as the deep number counts. Compared to the CIB evolution model of (Béthermin et al., 2011, hereafter B11), this work uses the angular power spectra and counts together, rather than just one-point statistics (counts and LFs). B11 utilise data from a wider range of frequencies. Our selection is restricted to the MIPS 70 μm data and lower frequencies; while our SED parameterisation allows phenomenologically for the presence of hot dust components (see Section 5.2.2), our focus is on the colder dust that is associated with star formation. We also do not consider a model for polycyclic aromatic hydrocarbon (PAH) or other spectral line emission, which begin to contribute to the CIB at higher frequencies (e.g., Leger & Puget, 1984; Lagache et al., 2004). An expanded SED model, and constraints from data at higher frequencies, can be included in our model at a future date.

The layout of this chapter is as follows: in Section 5.2 we describe the model parameters we are attempting to constrain with our fitting, in Section 5.3 we describe our treatment of the data and uncertainties, results are presented in Section 5.4, and a discussion and conclusions follow in Sections 5.5 and 5.6. Calculations are performed using a flat, ΛCDM cosmology, with $\Omega_m = 0.2715$, $\Omega_b = 0.0455$, $h = 0.704$, $n_s = 0.967$, and $\sigma_8 = 0.81$ (Komatsu et al., 2011).

5.2 Model

In this section we present our model for the spectral and clustering properties of the dusty sources and show how it may be used to predict various statistics. The number of parameters used was determined by what was required by the data; the choice of parameters is, to some extent, arbitrary, and it is possible that other parameterisations may describe the data equally well. We find that the data strongly require redshift evolution of various quantities, and in each case we choose to parametrize this evolution as an expansion about a pure power law in $1+z$, using the form (for some quantity X):

$$\begin{aligned} \ln X &= \ln X_0 + \varepsilon \ln(1+z) + \zeta \ln^2(1+z) + ... \\ X &= X_0 (1+z)^{\varepsilon} \exp\left[\zeta \ln^2(1+z) + ...\right]. \end{aligned} \tag{5.1}$$

This reduces to a simple power law in $1+z$ if ε is the only non-zero evolution parameter, however more complex evolution, featuring a turning point or plateau, is allowed if the higher order parameters are non-zero. We prefer this expansion over the series of broken power laws adopted by B11, because it ensures that all derivatives are continuous, and, if a quantity peaks at a particular redshift, this redshift will emerge naturally (provided enough terms of the series can be constrained), without having to be separately fitted for or put in by hand. The baseline model contains only as many higher order evolution parameters for each quantity as improve the model likelihood; some alternative or extended parameterisations are considered in Section 5.4.

Our model is divided into three parts – the luminosity function, which describes the abundance of dusty sources as a function of redshift and integrated dust luminosity, the spectral energy distribution, which contains the frequency dependence of the dust emission, and the clustering properties (i.e., bias), which connects the spatial distribution of the sources to that of the underlying dark matter. Existing studies have largely dealt with only one of two of these three components at a time. B11 constrained the luminosity function evolution assuming fixed source SEDs from earlier work (Lagache et al., 2004). Pénin et al. (2012) then calculated predictions for the angular power spectra using the constraints obtained by B11. Similarly, Xia et al. (2012) fixed the spectral properties of the CIB sources using the results of Granato et al. (2004) and Lapi et al. (2011), and constrained source clustering properties using the spectra. We favour a combined analysis because, while it is more complex, it is capable of obtaining more robust parameter constraints and performing a more thorough exploration of the parameter degeneracies.

Given that the parameterisation we adopt is largely phenomenological, an important question is whether our model is capable of reproducing any data outside that directly used to constrain it, and comparisons with several other data sets are presented in Section 5.5.

5.2.1 Luminosity function

For brevity we refer to the bolometric dust luminosity, $L_{\rm dust}$, integrated over $8 < \lambda/\mu{\rm m} < 1000$, simply as L. The luminosity function, Φ, is defined such that the comoving number density of sources with luminosity in the interval $[L, L+dL]$ is given by

$$\Phi(L)\, d\log L = \frac{dN}{dV_c}. \tag{5.2}$$

Here, and throughout, 'log' refers to the base-10 logarithm. We adopt a double-exponential form for Φ (Saunders et al., 1990):

$$\Phi(L,z) = \Phi_c(z)\left(\frac{L}{L_c(z)}\right)^{1-\alpha_{\rm LF}} \exp\left(-\frac{1}{2\sigma_{\rm LF}^2}\log^2\left[1+\frac{L}{L_c(z)}\right]\right), \tag{5.3}$$

with normalisation Φ_c, characteristic luminosity L_c, power-law index $\alpha_{\rm LF}$ and spread parameter $\sigma_{\rm LF}$. This form was proposed as a modification to the classical Schechter function (Schechter, 1976), in order to fit IRAS data, and has subsequently been used in a range of CIB source analyses (e.g., Pozzi et al., 2004; Le Floc'h et al., 2005; Caputi et al., 2007), including that of B11, which is the existing work most similar to ours, and thus the most obvious choice for direct comparison with our results. We note that the number of faint sources diverges for $\alpha_{\rm LF} > 1$, but we choose to allow this behaviour since, provided the total luminosity is convergent (i.e., $\alpha_{\rm LF} < 2$), it is not necessarily prohibited by the data.

The redshift evolution of the characteristic dust luminosity is given by

$$L_c(z) = L_0(1+z)^{\varepsilon_L} \exp\left[\zeta_L \ln^2(1+z)\right]. \tag{5.4}$$

and the evolution of the normalisation, Φ_c, by:

$$\Phi_c(z) = \Phi_0(1+z)^{\varepsilon_\Phi} \exp\left[\zeta_\Phi \ln^2(1+z)\right]. \tag{5.5}$$

We find that the lower bound of $\alpha_{\rm LF}$ is poorly constrained in our fit, and we consequently adopt a prior of $\alpha_{\rm LF} > -0.5$; this value was chosen to lie far from the preferred value of $\alpha_{\rm LF} \gtrsim 1$ from existing analyses (e.g., Saunders et al., 1990; Takeuchi et al., 2003; Patel et al., 2012). The predictions of our model – counts, power spectra, and other quantities like dust luminosity density – vary minimally if we allow $\alpha_{\rm LF}$ to take more negative values. There is a strong three-way degeneracy between $\alpha_{\rm LF}$, L_0, and Φ_0. While these parameters individually are sensitive to the prior adopted for $\alpha_{\rm LF}$, our model predictions are all driven by the behaviour at the brighter end of the LF, which depends on a parameter combination that it is not dependent on the $\alpha_{\rm LF}$ prior.

5.2.2 Spectral energy distribution

The flux, S_ν, observed at frequency ν from a source at redshift z can be related to the bolometric IR luminosity L via the spectral function, ϕ_ν, as described in Section 1.4:

$$S_\nu(L,z) = \frac{L_{\nu(1+z)}}{4\pi(1+z)\chi^2(z)}, \tag{5.6}$$

where χ is the comoving distance, and

$$L_\nu = \frac{dL}{d\nu} = L\frac{\phi_\nu}{\int d\nu' \phi_{\nu'}}, \tag{5.7}$$

with the integral in the denominator of the fraction taken over 8 μm $< c/\nu <$ 1000 μm. Our model is intended to phenomenologically capture the global properties of dust emission, such that all the parameters of the model are constrained from the data, while still providing a good fit. We consequently make several simplifying assumptions when modelling the dust SED. Most importantly, we consider only a single SED at each redshift, motivated by recent studies that have found relatively little scatter about such a 'universal' SED shape for observed dusty galaxies (Elbaz et al., 2011; Lapi et al., 2011).

We adopt a six-parameter model to describe this universal SED. There are two dust components, one at temperature T_a, which evolves with redshift as

$$T_a(z) = T_0(1+z)^{\epsilon_T} \exp\left[\zeta_T \ln^2(1+z)\right], \tag{5.8}$$

and the other at a fixed temperature, T_b. We would expect dust temperature to increase naturally with increasing redshift due to the increasing temperature of the CMB (Blain, 1999a), but find that, for the range of T_b values preferred by the data ($\sim$ 50 K – see Section 5.4), and redshift range relevant to our calculations ($z \leq 6$), this effect is negligible. A single spectral emissivity index, β, is common to both components, and the final parameter, f_b, describes the contribution of the 'b' dust component to the total dust IR luminosity. The spectral function, summing the contributions from both dust components, is given by

$$\phi_\nu \propto \frac{\nu^\beta B_\nu(T_a)}{\int d\nu' \nu'^\beta B_{\nu'}(T_a)} + f_b \frac{\nu^\beta B_\nu(T_b)}{\int d\nu' \nu'^\beta B_{\nu'}(T_b)}, \tag{5.9}$$

so that $f_b = 1$ corresponds to the 'a' and 'b' components making equal contributions to the total dust luminosity.

A range of modifications to this model, such as allowing a separate emissivity index for each dust component, or evolution in the emissivity index, are considered in Section 5.4. We find that, for the data considered, none of these modifications lead to sufficient improvements in the model likelihood to warrant their inclusion in the baseline model.

Hall et al. (2010) and Shang et al. (2012) follow Blain (1999b) and replace the graybody Wien tail in the rest-frame mid-infrared with a power law in frequency, $\phi_\nu \propto \nu^{-2}$, as a phenomenological way to account for the presence of hotter dust without explicitly parameterising additional dust components. We choose to parametrize a second dust component directly in the baseline model, in order to facilitate, for instance, assessing the effect of allowing different emissivity indices between the two components, or evolution in their relative contribution to the total dust luminosity, however, we also investigated a range of SED models involving a power-law modification to the graybody Wien tail. We find that the two approaches yield similar results, provided evolution in dust temperature is allowed in each case (see Section 5.4.3). While an SED falling as a power law may provide a more realistic description of the emission from very small dust grains shortwards of the SED peak (e.g., Desert et al., 1990), there is sufficient flexibility in our baseline parameterisation to mimic this behaviour for the data considered.

It is important to note that the extent to which physical dust properties are captured by our model is not clear. Varying degrees of correlation between luminosity and dust temperature, not included in our parameterisation, are observed in different samples of dusty sources (e.g., Dunne et al. 2000; Dunne & Eales 2001; Blain et al. 2003, and references therein; Chapman et al. 2005; Sajina et al. 2006; Greve et al. 2012). There is, however, considerable scatter in this relation, both within and between different samples, and the extent to which it applies to distant faint sources, which contribute significantly to the angular power spectra, is unknown. Similarly, we have not considered the effect of dust self-absorption (the graybody equation we adopt is only valid in the optically thin limit), which may be significant, particularly at high redshift (e.g., Benford et al., 1999; Blain et al., 2003; Draine, 2006; Hayward et al., 2012). The fact that we see good consistency between our model predictions and various data over a range of frequency suggests our treatment is, however, at least phenomenologically reasonable, and it seems likely that the effects of the $L-T$ correlation or dust opacity, and their evolution, may be partially absorbed into our SED parameters (see Section 5.4.3 for further discussion).

We do not explicitly account for a duty cycle of the dust emission in our model (as considered by, e.g., Shang et al., 2012; De Bernardis & Cooray, 2012). We would expect our model predictions to be sensitive to whether star formation and dust emission on average happens continuously or in short-duration bursts – the Poisson anisotropy power, for instance, will be higher if, for some fixed total dust luminosity, the emission occurs from fewer, more luminous objects. In our model, this behaviour is absorbed into the luminosity function (and any evolution thereof), and we find excellent consistency in parameter constraints when fitting to the number counts alone, counts plus clustered power, and counts plus clustered plus Poisson power (see Section 5.5.5), suggesting that, again, our treatment is at least phenomenologically reasonable. We consequently defer considering a more physical but complex model, featuring, for example, both continuous and bursty modes of star formation, to future work.

5.2.3 CIB source clustering

The three-dimensional power spectrum of dusty galaxies can be written, neglecting stochastic bias, as

$$P_{\rm gal}(k,z) = \langle b_{\rm gal}(k,z)\rangle^2 P_{\rm DM}(k,z), \tag{5.10}$$

where $\langle b_{\rm gal}\rangle$ is averaged over all sources at a given redshift. We model the scale and redshift dependence of the bias as

$$\langle b_{\rm gal}(k,z)\rangle = b_0(1+z)^{\varepsilon_{\rm bias}}\left[1+A_{\rm bias}\left(\frac{k}{k_0}\right)\right]\exp\left(-\frac{k^2}{k_c^2}\right), \tag{5.11}$$

where the pivot scale, k_0, is chosen to be 1 Mpc^{-1}, and b_0, $\varepsilon_{\rm bias}$, $A_{\rm bias}$, and k_c are free parameters. We find that a variety of two-parameter descriptions of the scale dependence of the source bias are capable of providing an equally good fit to the data considered, but that the LF and SED constraints, which are the focus of the current work, are not sensitive to exactly what form is adopted. The model described above was chosen to include a small-scale cut-off, similar to that arising from $u_{\rm gal}$ in the halo model, while allowing some freedom on larger scales, mimicking the scale-dependence of halo bias; a more detailed description of the scale dependence of the source bias will be considered in future work. We take the dark matter power spectrum in equation (5.10) as the linear dark matter power spectrum, for simplicity, but find that treating the bias as being relative to the nonlinear matter power spectrum instead has, again, little effect of the LF and SED parameters (see Section 5.4.4). We calculate the matter power spectrum using the CAMB[a] distribution (Lewis et al., 2000).

Having described the dusty source properties we aim to constrain, we now turn to how model pre-

---

[a] http://camb.info/

dictions necessary to fit to real data may be calculated. A summary of the model parameters, along with the marginalised parameter constraints, is given in Section 5.4.

5.2.4 Angular power spectrum

As in earlier chapters, we write the angular power spectrum of CIB anisotropies from correlating a pair of maps at frequency ν as the sum of clustered and Poissonian components (e.g., Bond, 1996):

$$C_{\ell,\nu} = C^{C}_{\ell,\nu} + C^{P}_{\nu}, \tag{5.12}$$

where ℓ is the multipole moment. We take the Poisson contribution, which can be thought of arising from the correlation of the image of a source in one map with the image of the same source in the other map, to be independent of angular scale. On scales larger than $18''$ (the beam FWHM of the 250 μm SPIRE detector), all but very nearby galaxies will appear as point sources, and we assume that any local, extended sources, which may contribute scale-dependent Poisson power, since some internal structure is resolved, are masked from maps prior to calculating spectra (for instance by cross-matching with existing catalogues).

In the flat-sky limit (Limber, 1953; Kaiser, 1992), the clustered power is written as a single line-of-sight integral (e.g., Bond et al., 1991a; Kashlinsky & Odenwald, 2000; Knox et al., 2001; Tegmark et al., 2004). Since the number of faint sources is not required to be finite in our model, it proves helpful to work in terms of the comoving emissivity density, j_ν (Knox et al., 2001), rather than considering the mean properties of individual sources (as in Chapter 4). If source bias and luminosity are uncorrelated (see below), the clustered power can be written as

$$C^{C}_{\ell,\nu} = \int dz \frac{dz}{\chi^2} \frac{d\chi}{dz} \frac{1}{(1+z)^2} \langle b_{\rm gal}(k,z)\rangle^2 \, \langle j_\nu(z)\rangle^2_{\rm cut} P_{\rm DM}(k,z), \tag{5.13}$$

where wavenumber $k = (\ell + 1/2)/\chi(z)$, and $\langle j_\nu \rangle_{\rm cut}$ is the mean emissivity density once bright sources (brighter than $S_{\rm cut}$) have been masked from the map, given, in terms of the quantities defined above, by

$$\langle j_\nu(z)\rangle_{\rm cut} = (1+z)\chi^2 \int_0^{S_{\rm cut}} dS_\nu \frac{dL}{dS_\nu} \frac{\Phi(L,z)}{L \ln 10} S_\nu, \tag{5.14}$$

where here L is considered a function of S_ν, by inverting equations (5.6) and (5.7). The fact that S_ν and L are related by a simple constant at each redshift in our model simplifies this calculation.

Béthermin et al. (2012a) find evidence for dependence of star formation rate (and thus bolometric IR luminosity) on halo mass through abundance matching, and Wang et al. (2012) also find that the SFR–halo mass relation is not flat but has a peak at some characteristic mass scale, which evolves over time (see also Behroozi et al., 2012, and references therein). Since the halo bias increases with mass (e.g., Sheth & Tormen, 1999; Tinker et al., 2010a), we may therefore expect a correlation between dust luminosity and bias, and thus between j_ν and $b_{\rm gal}$. To allow for this, we consider re-writing the clustered power, via

$$\langle b_{\rm gal}(k,z)\rangle\langle j_\nu(z)\rangle_{\rm cut} \to \langle b_{\rm gal}(k,z)\, j_\nu(z)\rangle_{\rm cut}. \tag{5.15}$$

We investigate a range of treatments for the mean product of $b_{\rm gal}$ and j_ν, and find that, for the data considered, allowing an $L-b_{\rm gal}$ correlation serves primarily to degrade constraints on b_0, and has minimal effect on either the goodness of fit or other model parameters. We therefore do not include such a correlation in the baseline model; more discussion is provided in Section 5.4.4.

5.2.5 Poisson anisotropy power

Existing studies have typically treated the Poisson power either by adding an additional free parameter to each spectrum (as in Chapters 2 and 3, see also, e.g., Amblard et al., 2011; Xia et al., 2012), or using the predictions of the B11 CIB model (Planck Collaboration et al., 2011c; Shang et al., 2012). We instead require that our model for the dusty source LF and SEDs successfully reproduces the Poisson, as well as the clustered component of the angular power spectrum. In terms of the quantities introduced earlier, the Poisson contribution to the anisotropy power is given by

$$C_\nu^P = \int dz \frac{d\chi}{dz}\chi^2 \int_0^{S_{\rm cut}} dS_\nu \frac{dL}{dS_\nu}\frac{\Phi(L,z)}{L\ln 10}S_\nu^2 \tag{5.16}$$

Since the Poisson power is weighted more towards the brighter sources, one may expect that fitting to deep number counts already constrains the Poisson power. We find that, in fact, this is not the case, and that the Poisson tail in the SPIRE, ACT, and SPT spectra carries some additional constraining power over the source counts (see Section 5.5.5). The fact that there is useful signal in the shot noise is one of the main results of this work.

Our treatment of source removal in equations (5.14) and (5.16) has two potential limitations. Firstly, several fainter sources in the same instrumental beam area may appear as a single bright source with flux exceeding S_{cut}. Unless candidate bright sources are followed up with higher resolution measurements, and these multiple source cases corrected, the level of source removal in the map will not exactly match that in the model calculation. Secondly, real map masking typically involves removing a beam area from the map, which will remove flux from any sources lying near the target source (for instance, sources in the same group or cluster). These effects may be quantified by constructing a simulated sky map of CIB sources from the theoretical model, and mimicking the actual masking scheme that was used on the real data, which we will consider in future work. Uncertainty in the modelling of the bright source removal will have most effect on the Poisson power, which receives a larger relative contribution from bright sources than the clustered power. In Section 5.5.5, we consider repeating the fit using additional free parameters for the Poisson level in each spectrum (as in Chapters 2 and 3), rather than using our dusty galaxy model predictions, and show that any parameter bias induced by incorrect modelling of the source removal is likely to be small.

5.2.6 Differential number counts

The differential number counts are modelled using the quantities introduced above as (see, e.g., discussion in B11)

$$\frac{dN}{dS_\nu} = \int dz \frac{d\chi}{dz} \chi^2 \frac{dL}{dS_\nu} \frac{\Phi(L,z)}{L \ln 10}, \tag{5.17}$$

where, as in equation (5.14), L is taken as a function of S_ν and z. The Euclidean-nomalised counts (multiplied by a factor of $S^{2.5}$) are integrated over the finite width of each flux bin to compare with the measured counts.

Table 5.1: Angular power spectra used for constraining the baseline model

	Freq (GHz)	Bandpowers	Angular scale	$S_{\rm cut}^{\dagger}$ (mJy)	$\sigma_{\rm cal}^{\ddagger}$ (%)
Planck-HFI	857	9	$80 < \ell < 2240$	710	7
	545	9	$80 < \ell < 2240$	540	7
	353	9	$80 < \ell < 2240$	325	2
	217	9	$80 < \ell < 2240$	245	2
Herschel-SPIRE	1200	23	$2000 < \ell < 63300$	50	15
	860	21	$2000 < \ell < 41200$	50	15
	600	19	$2100 < \ell < 26300$	50	15
ACT	218	13	$2391 < \ell < 9900$	20	7
SPT	220	15	$2000 < \ell < 9400$	$6.4^{\dagger}$	$4.8^{\ddagger}$

† level above which bright sources are masked in the map prior to calculating spectra – $S_{\rm cut}$ is given at 150 GHz for ACT and SPT (see text)

‡ absolute map calibration uncertainty; the SPT calibration uncertainty is in units of power; other calibration uncertainties are in units of flux

5.3 Data treatment

We constrain the model parameters described in Section 5.2 using a combined fit to deep number counts from *Spitzer*-MIPS (Béthermin et al., 2010), *Herschel*-SPIRE (Béthermin et al., 2012b, hereafter B12), and angular power spectra from SPIRE (Amblard et al., 2011), *Planck*-HFI, (Planck Collaboration et al., 2011c), ACT (Das et al., 2011a), and SPT (Reichardt et al., 2012b). The MIPS number counts are given in Tables 3 to 6 of Béthermin et al. (2010), and the SPIRE number counts in Tables 2, 3 and 4 of B12. We summarise key properties of the power spectra in Table 5.1. Note that we do not use the full range of SPIRE or ACT bandpowers in the baseline fit; we use only data from $\ell > 2000$ for SPIRE, and $\ell \gtrsim 2400$ for ACT, because of uncertainty in Galactic cirrus contamination and spectrum-to-spectrum correlations in the SPIRE data, and because data from lower ℓ in ACT do not contribute significant constraining power once the primary CMB power spectrum is subtracted (see Sections 5.3.4 and 5.3.7, below). Note that the bright sources in the ACT and SPT maps were masked based on flux at 150 GHz, not 220. Our model allows us to account for this, since, for given model parameters, we know both the 150 and 220

GHz flux of all sources, and we can calculate the equivalent $S_{\rm cut}$ at 220 GHz as a function of redshift.

We do not consider counts from lower wavelengths than the 70 μm MIPS band because, as stated earlier, our focus is on dust emission associated with star formation rather than other contributions – such as hotter dust emission, or PAH features – to the SED. We do not use counts from lower frequencies than 600 GHz because of possible enhancement of the intrinsic counts by strong gravitational lensing (see Section 5.3.5). Our choice of spectra was limited to $\nu \geq 220$ GHz due to the presence of the thermal Sunyaev Zel'dovich effect (tSZ; Sunyaev & Zel'dovich, 1970), possible tSZ–CIB cross-correlations (Chapter 4), and the increased importance of the primary CMB anisotropies, in data at lower frequencies.

Given the large number of parameters and potentially complex parameter degeneracies, we explore the parameter space using the MCMC methods described in Section 1.5. The posterior probability is proportional to the product of the likelihood, $\mathscr{L}$, and the prior probability. We work with the negative log-likelihood, given by

$$-2\ln\mathscr{L} = \sum_{i=1}^{N}[\mathbf{M}_i(\theta) - \mathbf{D}_i]^T \cdot \mathbf{C}_i^{-1} \cdot [\mathbf{M}_i(\theta) - \mathbf{D}_i], \tag{5.18}$$

where the index i runs over the independent data sets, the elements of the data vectors $\mathbf{D}_i$ are either the binned spectrum bandpowers (see below) or the binned number counts, as appropriate, $\mathbf{M}_i(\theta)$ are the corresponding vectors of model predictions, which depend on the model parameters at each step, denoted by θ, and $\mathbf{C}_i$ are the covariance matrices, which contains the data uncertainties.

The data are divided into $N = 18$ independent sets, each with its own data vector and covariance matrix: one for the SPIRE spectra, one for the *Planck* spectra, one for the ACT spectrum, one for the SPT spectrum, twelve for the SPIRE counts (three bands times four redshift bins), one for the MIPS 70 μm counts and one for the MIPS 160 μm counts. We account for spectrum-to-spectrum correlations between the three SPIRE spectra and between the four *Planck* spectra (Section 5.3.7), meaning that there is not a separate covariance matrix for each individual SPIRE or *Planck* spectrum. As in B11, we assume that the quoted error bars in the number count measurements are uncorrelated across flux bins. This is probably not entirely accurate, because, for instance, of using small fields which may not be representative of the global mean (see Section 5.3.7). Future constraints on these correlations can be easily incorporated into our future modelling work.

At each step of the MCMC chain, the likelihood is multiplied by the contribution from parameter priors described later in this section. In particular, Gaussian priors are adopted on the photometric calibration parameters, f^{cal}, which are discussed in Section 5.3.3; there are a total of $N_{\mathrm{cal}} = 14$ calibration parameters: one for each of the three SPIRE spectra, each of the four *Planck* spectra, the ACT spectrum, the SPT spectrum, the three SPIRE bands for the SPIRE number counts, and the two MIPS bands. A separate calibration is allowed for the SPIRE spectra and counts (see Section 5.3.3).

The remainder of this section contains discussion of various issues relating to fitting models to the counts and angular power spectra.

5.3.1 Binned spectra

The measured power spectra were calculated using bins in ℓ rather than individual ℓ values. The resulting bandpower values C_b are related to the unbinned C_ℓs by

$$C_b = \frac{\sum_\ell W_\ell C_\ell}{\sum_\ell W_\ell}, \tag{5.19}$$

where the sum is over all ℓ values in bin b, and W_ℓ is a weight function, which is equal to unity for the SPIRE spectra, and ℓ for the *Planck* spectra (see Section 4.1 of Planck Collaboration et al., 2011c). The weighting of the ACT and SPT spectra is slightly more complex; see Das et al. (2011a) and Reichardt et al. (2012b) for more details. We use the same binning and weighting scheme used for the measured bandpowers when calculating the model predictions.

5.3.2 Accounting for bandpass filter profiles

The CIB intensity and anisotropy depend strongly on frequency over the wavelength range considered (e.g., Fixsen et al., 1998; Planck Collaboration et al., 2011c), with the anisotropy power at a given angular scale increasing by up to an order of magnitude across the microwave *Planck* and SPT bandpass filters (see Figure 3.3 in Chapter 3). Accounting for the bandpass filter transmission profile when fitting models to the measured data is therefore important. The *Planck* and SPIRE bandpowers are already corrected for the bandpass filter profile but the correction assumes a source SED that varies as $S_\nu \propto 1/\nu$ (i.e., $\nu S_\nu =$ const.). Converting the bandpowers to the 'real' flux units for a source with observed SED S_ν requires multiplying by a factor F_c^2, where (e.g., Planck HFI Core Team et al., 2011a)

$$F_c = \frac{\int d\nu\, \tau(\nu) \frac{\nu_0}{\nu}}{\int d\nu\, \tau(\nu) \frac{S_\nu}{S_{\nu_0}}}, \tag{5.20}$$

where $\tau(\nu)$ is the bandpass filter transmission profile, and ν_0 is the nominal frequency of the band (these values are listed in Table 5.1). The model predictions, evaluated at the nominal frequencies, may then be compared directly to the corrected bandpowers. For the SPIRE spectra, the transmission profile in the denominator is weighted by an additional ν^{-2} to account for the bandpass response to diffuse, as opposed to point-like, emission, as described in Section 5.2 of the SPIRE Observers Manual[b].

In practice, we find that small errors in the bandpower correction factors are largely absorbed into the map calibration uncertainties (see Section 5.3.3), without biasing any of the CIB model parameters. Consequently, rather than recalculating the bandpower correction factors for all the individual source SEDs at each step of the MCMC chain, we adopt a simplified iterative approach, similar to that used in Chapter 3. We re-run the MCMC chain several times. After each chain is complete, we take the best-fit model parameters and calculate the integrated CIB intensity as a function of frequency. This integrated CIB SED is then used in equation (5.20) to calculate the bandpower correction factors, and these factors are then used throughout the next chain. We find that this method leads to good convergence of the correction factors (values calculated at the end of the chain matching the input values) after three chains.

The ACT and SPT bandpowers are given in units of CMB temperature, which can be converted to flux density (i.e., $\mu\mathrm{K}^2$ to $\mathrm{Jy}^2\ \mathrm{sr}^{-1}$) as described in Appendix B of Chapter 2, by multiplying by $(\partial B_\nu / \partial T|_{T=T_{\mathrm{CMB}}})^2$, where

$$\frac{\partial B_\nu}{\partial T} = \frac{2 k_{\mathrm{B}} \nu^2}{c^2} \frac{x^2 e^x}{(e^x - 1)^2}, \tag{5.21}$$

$x = h_{\mathrm{p}} \nu / k_{\mathrm{B}} T_{\mathrm{CMB}}$, and T_{CMB} is the present-day CMB temperature. This conversion factor must be integrated over the filter bandpass, and the ACT and SPT bandpower correction factors, including the effects of both the units conversion and the source SED, are therefore given by $F_c'^2$, where

$$F_c' = \frac{\int d\nu\, \tau(\nu) \frac{\partial B_\nu}{\partial T}|_{T=T_{\mathrm{CMB}}}}{\int d\nu\, \tau(\nu) \frac{S_\nu}{S_{\nu_0}}}. \tag{5.22}$$

---

[b] http://herschel.esac.esa.int/Docs-SPIRE/html/spire_om.html#x1-880005.2.1

An alternative, equivalent, approach to that presented here would be to calculate the effective frequency of each bandpass for a given input SED, and use these effective frequencies to calculate the model predictions, rather than the nominal ones (as in, e.g., Chapter 3, and Reichardt et al., 2012b). We adopt the method described above because we foresee normalisation to the nominal frequencies facilitating comparison with future work, especially as additional data sets are added.

5.3.3 Photometric calibration uncertainties

The data considered in this work were obtained using instruments that do not measure absolute flux and must therefore be calibrated using ancillary measurements (see Stansberry et al. 2007, Gordon et al. 2007, Swinyard et al. 2010, Planck HFI Core Team et al. 2011, Hajian et al. 2011, and Lueker et al. 2010 for details of the MIPS 160 μm, MIPS 70 μm, SPIRE, HFI, ACT and SPT calibration, respectively). Each power spectrum was calculated from maps with the best-guess flux calibration correction applied, however the uncertainty in this calibration is not negligible compared to the statistical uncertainties in the bandpowers, and it is therefore necessary to correctly account for the calibration uncertainty during model fitting.

Let the calibration of the maps for the quoted bandpower values equal unity, and let $f^{\rm cal}$ be the factor, in flux units, that the map must be multiplied by in order to achieve the correct calibration. We fit for $f^{\rm cal}$ as eight extra free parameters (one for each spectrum), as in Chapter 3. At each step of the MCMC chain, the bandpowers and errors of each spectrum are multiplied by the corresponding $(f^{\rm cal})^2$ before the likelihood is calculated. Furthermore, in order to penalise models requiring $f^{\rm cal}$ to be considerably different from one, we impose Gaussian priors on each $f^{\rm cal}$, with mean of unity and standard deviation equal to the quoted calibration uncertainty for that band. We also account for an additional effect of the calibration uncertainty on the power spectrum, namely that bright sources are not masked to the nominal flux value, $S_{\rm cut}$, but actually to $f^{\rm cal}S_{\rm cut}$, by substituting these modified values into equations (5.14) and (5.16).

Absolute flux calibration uncertainty also affects the differential number counts; the lower and upper limits of each flux bin, $S_{\rm min}$ and $S_{\rm max}$, must be replaced by $f^{\rm cal}S_{\rm min}$ and $f^{\rm cal}S_{\rm max}$, respectively, at each MCMC step, while $S^{2.5}\frac{dN}{dS} \rightarrow (f^{\rm cal})^{1.5}S^{2.5}\frac{dN}{dS}$. In the time between the analyses of Amblard et al. (2011)

and B12, the SPIRE flux calibration uncertainty was improved from the 15% quoted above to 7% in each band, with a band-to-band relative calibration uncertainty of 2% (values taken from the SPIRE Observers Manual). We account for this by fitting for separate calibration parameters for the SPIRE spectra and the SPIRE counts. The effect of calibration on the MIPS counts is treated in the same way as for the SPIRE counts. This calibration treatment is identical to that adopted by B11.

5.3.4 Non-CIB contributions to spectrum

All the spectra were calculated from regions of the sky that are known to be relatively free from Galactic dust contamination, however some diffuse, cirrus, emission is still present. The cirrus was cleaned from the *Planck* maps using cross-correlations with high-resolution Galactic HI maps (Section 2.5 of Planck Collaboration et al., 2011c), and the *Planck* 143 GHz channel was used to remove the primary CMB contribution. Amblard et al. (2011) remove the cirrus in the SPIRE power spectrum using an extrapolation of the cirrus power from lower wavelengths, however Planck Collaboration et al. (2011c) found that this treatment overestimated the cirrus contamination. We therefore adopt a similar treatment to De Bernardis & Cooray (2012), and fit for the cirrus contamination in the SPIRE power spectra along with the CIB. We further reduce the impact of incorrect cirrus modelling by only including SPIRE data at $\ell > 2000$ in our fit (see also Section 5.3.7). We assume that the cirrus power spectrum has the form $C_\ell^{\rm cirr} = A_{cirr}(\ell/2000)^{-n_{\rm cirr}}$. We fit for the amplitude $A_{\rm cirr}$ at 1200 GHz, and assume a graybody frequency dependence of the cirrus flux with emissivity index $\beta = 1.5$ and effective temperature $T = 20$ K (consistent with results obtained by Bracco et al., 2011) to scale the cirrus to 860 and 600 GHz. Planck Collaboration et al. (2011c) find that the cirrus is negligible at these lower frequencies in the Lockman Hole (the field from which the SPIRE spectra were measured), and so we do not expect our results to be sensitive to the treatment of the cirrus in these bands. We adopt a Gaussian prior on $n_{\rm cirr}$, centred at 2.89, with a 1σ spread of 0.44, using the constraint obtained by Lagache et al. (2007), but doubling the width of the uncertainty to account for possible variation of the cirrus index with frequency. We find that, in fact, even the cirrus in the 1200 GHz SPIRE power spectrum is not significantly detected in our fit, and that the treatment of the SPIRE cirrus has essentially no impact on the CIB source properties.

We consider several non-CIB contributions to the ACT and SPT spectra. The primary lensed CMB anisotropies predicted by our adopted cosmology are subtracted from the ACT and SPT bandpowers; uncertainty in the CMB spectrum from cosmological parameter uncertainties is sufficiently small that they it may be ignored at 220 GHz on the angular scales considered (at least for a standard cosmological model), although the errors on the ACT spectra at $\ell \lesssim 2400$ after subtracting the primary CMB are large, and consequently we only include a limited range of bandpowers in the fit. Reichardt et al. (2012b) find that the Galactic cirrus contributes to the total measured SPT 220 GHz power spectrum only at the per cent level, and we therefore adopt the model described in their Section 5.6, without adding additional free parameters. No subtraction of Galactic dust is performed for the ACT spectrum. Radio source contamination is minimal with the SPT source mask; we include a radio Poisson component with amplitude fixed to the mean of the Gaussian prior adopted by Reichardt et al., namely 1.28 $\mu\mathrm{K}^2$, which corresponds to 0.16 $\mathrm{Jy}^2\ \mathrm{sr}^{-1}$ at 220 GHz. Fewer bright sources are masked in the ACT maps, and consequently the radio source power is larger; we marginalise over the amplitude of the ACT radio Poisson component with a Gaussian prior of $4.1 \pm 0.8\ \mu\mathrm{K}^2$ (corresponding to $0.48 \pm 0.09\ \mathrm{Jy}^2\ \mathrm{sr}^{-1}$), adopting the mean value obtained by Dunkley et al. (2011), but conservatively doubling the measured uncertainty; as with the SPIRE cirrus level we find that our results are not affected by the exact treatment of the ACT radio Poisson level.

While the ACT and SPT bands used are virtually at the thermal Sunyaev Zel'dovich effect null, the blackbody kinematic Sunyaev Zel'dovich (kSZ) effect will be present (although Reichardt et al. 2012 found that it contributes at most a few per cent of the total 220 GHz power). We allow for a non-zero kSZ component, fitting for the power at $\ell = 3000$, A_{kSZ}, using a fixed shape in ℓ, obtained from hydrodynamical simulations (N. Battaglia et al, in prep). We opt not to put any lower or upper limits on the kSZ amplitude. Reichardt et al. (2012b) found that, even with the three SPT bands, constraining the size of the kSZ power spectrum is extremely challenging, due to the presence of possible tSZ–CIB correlations (which were the subject of Chapter 4; also see Zahn et al., 2012), and we prefer dust emission parameter constraints to be very slightly degraded over making stronger assumptions about the kSZ power.

In principle, power spectrum measurements at 220 GHz could allow meaningful kSZ constraints to be obtained in the absence of the tSZ and tSZ–CIB contributions. We find that, for the data considered, the dominant dusty source contribution at 220 GHz is not sufficiently well-constrained for the kSZ constraints to be useful (see Section 5.5.4).

5.3.5 Effect of strong gravitational lensing

The observed bright-end CIB source counts in the submm and at longer wavelengths are expected to differ from the intrinsic counts due to the effect of strong gravitational lensing by foreground groups and clusters (e.g., Blain, 1996; Perrotta et al., 2002; Negrello et al., 2007; Lima et al., 2010b; Negrello et al., 2010). While, for any given source, this effect is not frequency dependent, the fact that lower frequencies receive a larger relative contribution from sources at higher redshift, where the lensing cross-section is higher, means that we may expect the enhancement of the intrinsic counts to increase with decreasing frequency.

A full treatment for the effect of lensing requires modelling the distribution of lens systems and lensing cross-sections (e.g., Lima et al., 2010a; Hezaveh & Holder, 2011). Furthermore, Mead et al. (2010) find that baryonic physics, including active galactic nuclei feedback, may double the strong lensing cross-section for massive clusters, while Hezaveh et al. (2012) show that compact sources are preferentially more strongly lensed, introducing a source-size dependence. Accounting for the lensing effect on CIB counts thus requires extensive modelling beyond that used to describe the intrinsic $\mathrm{d}N/\mathrm{d}S$.

In this work, we conservatively choose not to constrain our model with counts from shorter frequencies than the SPIRE 600 GHz band. Even at this frequency, significant enhancement of the counts is possible for $S \gtrsim 100$ mJy (e.g., Negrello et al., 2007, B11). The uncertainties in the B12 counts at the bright end are large due to the limited sky coverage, suggesting that the bias introduced in our parameters by ignoring the effects of the lensing is likely to be small. We consider the effect of excluding either the bright-end counts ($S \gtrsim 60$ mJy), or indeed the high-redshift ($z > 2$) SPIRE counts completely, and find that, indeed, there is no systematic change in the parameter constraints. We ignore the effect of strongly-lensed sources on the angular power spectra because the lensing preserves surface brightness, and it is fluctuations in surface brightness that the spectrum measures. In addition, the brightest sources are masked from the maps before the spectra are calculated.

5.3.6 Instrumental beam treatment

Uncertainty in the instrumental beam profile comes to dominate the power spectrum error budget on scales approaching the angular resolution of a detector. We may expect the beam uncertainty to be correlated across a range of multipoles because changing the beam shape affects the inferred power spectrum over a range of scales.

For the *Planck* spectra, we use the beam error estimates given in Table 4 of Planck Collaboration et al. (2011c), taking the error bar on each bandpower as the quadrature sum of the statistical and beam uncertainty, however we further assume a 100% correlation in the beam uncertainty across bandpowers in each spectrum (appropriate for a Gaussian beam whose width is uncertain). Since we are fitting to multiple data sets and constraints on smaller angular scales come mainly from SPIRE, ACT and SPT, our results are insensitive to the exact treatment of the *Planck* beam uncertainties, as found in Chapter 3.

The SPT bandpower covariance matrices include the contribution from estimated beam uncertainties (both in the diagonal and off-diagonal, bin-to-bin correlation, terms), and so to account for the beam uncertainty we therefore include the full covariance matrix for each spectrum in our likelihood.

Amblard et al. (2011) and Das et al. (2011a) found that bin-to-bin correlations in the SPIRE and ACT spectra, due either to correlated beam uncertainties, or the source mask, are small, and we also therefore neglect them in this work.

5.3.7 Cosmic variance

The deepest B12 number counts were obtained from an area of only half a square degree (GOODS-N field). It is difficult to quantify the extent to which these data may not be representative of the global mean, and no estimate is provided of this cosmic variance contribution to the error budget. Furthermore, it is apparent from Figure 10 of B12 that the counts, binned by redshift, are not always consistent between GOODS and the larger COSMOS field within the quoted error bars. There is good consistency between the counts in the lowest GOODS flux bin and those found from the P(D) analysis of Glenn et al. (2010), but, since both analyses use the same field, this does not help inform our treatment of the cosmic variance uncertainty. We choose to include only the counts from the larger COSMOS field counts in our fit. While we cannot rule out the possibility that the faint counts in the smaller field are, in fact, more representative of the global population, we find no current motivation for favouring these data. We consider the effect of adding the GOODS data in Section 5.4.

On large scales, uncertainties in the *Planck* and SPIRE bandpowers are dominated by a cosmic variance term, arising from the limited sampling of large scale Fourier modes, due to finite sky coverage, rather than instrumental noise. For binned bandpower, C_b, with bin b spanning $\ell_{\rm min} \leq \ell \leq \ell_{\rm max}$, this cosmic variance contribution is given analytically by (e.g., Fowler et al., 2010; Das et al., 2011a)

$$\sigma^2_{b,\nu} = \frac{2}{\ell^2_{\rm max} - \ell^2_{\rm min}} C^2_{b,\nu} \frac{1}{f_{\rm sky}}, \tag{5.23}$$

where $f_{\rm sky}$ is the fraction of sky covered by the map used to calculate the spectrum. For spectra calculated from the same patch of sky, there will be a correlation in this cosmic variance uncertainty between spectra at frequencies ν_1 and ν_2, given, for bandpower b (assuming the same binning of the two spectra), by

$$\sigma^2_{b,\nu_1\nu_2} = \frac{2}{\ell^2_{\rm max} - \ell^2_{\rm min}} C^2_{b,\nu_1\nu_2} \frac{1}{f_{\rm sky}}, \tag{5.24}$$

where $C^2_{b,\nu_1\nu_2}$ is the binned cross-spectrum. As discussed in Chapters 2 and 3, the CIB is highly coherent across the range of frequencies considered, and, consequently, we do not expect these off-diagonal $\sigma^2_{b,\nu_1\nu_2}$ terms to be negligible for the three SPIRE or four *Planck* spectra. While Amblard et al. (2011) and Planck Collaboration et al. (2011c) do not present the cross-spectrum bandpowers, we can use our model to estimate $C^2_{b,\nu_1\nu_2}$. The effect of the spectrum-to-spectrum correlation in the SPIRE spectra will be larger than for *Planck*, because considerably less sky was used and the bandpowers are binned more finely. Due to this fact, and the possible cirrus contamination on large scales in the SPIRE spectra (Section 5.3.4), we do not include any SPIRE bandpowers from $\ell < 2000$, preferring the large-scale power to be constrained by *Planck* alone. Removal of the large-scale SPIRE data does not significantly worsen parameter constraints.

We find that we can adequately account for the *Planck* and remaining SPIRE spectrum-to-spectrum correlation with a simplified iterative approach, as with the filter profile correction described in Section 5.3.2, without requiring additional calculations at each MCMC step. At the end of each MCMC chain, we use the best-fit model parameters to calculate the ratio $C^2_{b,\nu_1\nu_2}/(C_{b,\nu_1}C_{b,\nu_2})$ for each bandpower and for each cross-spectrum (e.g., 857 × 545, 857 × 353, 857 × 217, 545 × 353, 545 × 217 and 353 × 217 GHz for *Planck*, where the multiplication symbol here denotes cross-correlation). This ratio is then multiplied by the corresponding measured auto-spectra bandpowers to calculate an estimate for the cross-spectrum bandpowers, which are used to calculate the off-diagonal covariance elements, $\sigma^2_{b,\nu_1\nu_2}$, for use in the subsequent chain.

The final covariance matrix used in our likelihood for the bandpower fitting therefore contains off-diagonal elements from bin-to-bin correlations for the *Planck* and SPT bandpowers (due to correlated beam uncertainties), as well as off-diagonal elements arising from spectrum-to-spectrum correlations for the SPIRE and *Planck* bandpowers (due to correlated cosmic variance uncertainties).

We note that there is a partial overlap between the Lockman Hole region used for the Amblard et al. (2011) SPIRE analysis and one of the regions used to calculate the *Planck* spectra. Since five separate, larger, regions are also used in the *Planck* analysis, we neglect the effect of any correlation in the cosmic variance uncertainty *between* the *Planck* and SPIRE spectra. Similarly, there is an overlap of the ACT and SPT maps, but we are considering small enough angular scales in these spectra that the error budget is dominated by noise rather than cosmic variance.

5.4 Results

5.4.1 Goodness of fit and parameter constraints

Globally, the model provides a good fit to the data, with $\chi^2/\text{d.o.f.} = 223/248 = 0.90$. The degrees of freedom are calculated by summing the number of bandpowers (36 *Planck*, 63 SPIRE, 15 SPT and 13 ACT) and counts (105 SPIRE and 39 *Spitzer* flux bins), and subtracting the number of free parameters (18 CIB model parameters, plus the SPIRE cirrus amplitude and index, kSZ amplitude, and ACT radio Poisson amplitude). The χ^2 contribution from the SPIRE and MIPS number counts is low (92/144 data points). As mentioned in Section 5.3, quantifying the uncertainties in the deepest number counts from the stacking analyses is challenging. Despite this, calculating the global goodness of fit remains useful, since it allows us to discriminate between alternative models.

The 1-D marginalised parameter constraints, and CIB parameter correlation matrix, are shown in Tables 5.2 and 5.3, respectively. The parameters are grouped into three sections – luminosity function, SED and bias. While there are strong correlations within each section, a combined fit to the counts and spectra greatly reduces the correlation between parameters in different sections. In particular, the parameters describing the CIB source bias parameters are virtually decoupled from the LF and SED parameters. This is a clear advantage of combining a wide range of data sets and is why, as stated in Section 5.2, our LF and SED results are robust against changes in the choice of bias parameterisation.

The best-fit model angular power spectra are shown in Figure 5.1. The bandpowers shown include the corrections for source SEDs and bandpass filter transmission described in Section 5.3.2, as well as the best-fit calibration parameters. Figures 5.2 and 5.3 show differential number counts from SPIRE and MIPS respectively, similarly corrected. When comparing our model with other data sets, or predictions from other models, it is therefore not sufficient to consider only the model curves plotted in Figures 5.1 to 5.3, which do not reflect the variation allowed by the calibration uncertainty. The full model covariance, including the effect of the calibration uncertainties, is used for all the confidence contour plots presented later in this chapter.

The remainder of this section deals, in turn, with the three parts of our model. We make comparisons with existing work and discuss a range of model extensions or modifications.

5.4.2 Luminosity function

The faint-end slope of the LF, $\alpha_{\rm LF} = 0.33^{+0.53}_{-0.55}$, is poorly constrained using the data we have considered, even with the $\alpha_{\rm LF} > -0.5$ prior discussed in Section 2.1. While our result is consistent with the value of $\alpha_{\rm LF} \sim 1.2$ typically obtained in the literature (e.g., Saunders et al., 1990, B11) within 2σ, considerably lower values are also permitted. B11 found $\alpha_{\rm LF} = 1.223 \pm 0.044$; their constraint is tighter than ours only because of including very local constraints from IRAS and so does not correspond to a tighter constraint on the behaviour of faint high-redshift sources. Including the GOODS-N counts from B12 in the fit (which are not included in the baseline fit – see discussion in Section 5.3.7) improves the constraint substantially to $\alpha_{\rm LF} = 0.64 \pm 0.26$; being able to robustly extract deep number counts is clearly important for future constraints on the shape of the faint-end luminosity function at high redshift. Given the mild preference shown for lower values of $\alpha_{\rm LF}$, we consider allowing $\alpha_{\rm LF}$ to evolve as a power law in $1+z$, but with $\alpha_{\rm LF}$ fixed to 1.2 at $z = 0$, and, indeed, the data prefer a decrease in $\alpha_{\rm LF}$ with increasing z, but

Table 5.2: Marginalised parameter constraints

Parameter	Mean	Description
$\alpha_{\rm LF}$	$0.33^{+0.53}_{-0.55}$	power law index describing faint-end slope of LF ($\Phi \propto L^{1-\alpha}$ for low L)
$\sigma_{\rm LF}$	$0.372^{+0.020}_{-0.021}$	LF spread
$\log L_0/L_\odot$	$9.60^{+0.27}_{-0.26}$	characteristic bolometric dust luminosity at redshift zero
ε_L	$4.75^{+0.46}_{-0.45}$	first order characteristic luminosity redshift evolution
ζ_L	-0.76 ± 0.25	second order characteristic luminosity redshift evolution
$\log \Phi_0$ / gal dex^{-1} Mpc^{-3}	$-1.92^{+0.15}_{-0.16}$	LF normalisation at redshift zero
ε_Φ	$-1.82^{+0.74}_{-0.75}$	first order LF normalisation redshift evolution
ζ_Φ	-0.66 ± 0.45	second order LF normalisation redshift evolution
T_a / K	25.8 ± 1.4	temperature of dust component 'a' at redshift zero
ε_T	-0.53 ± 0.10	first order T_a redshift evolution
ζ_T	0.55 ± 0.07	second order T_a redshift evolution
T_b / K	52 ± 6	temperature of dust component 'b' (does not vary with redshift)
β	$1.86^{+0.08}_{-0.09}$	dust spectral emissivity index
f_b	0.53 ± 0.10	contribution of dust component 'b' to bolometric dust luminosity
b_0	0.86 ± 0.19	dusty source bias at redshift zero
$\varepsilon_{\rm bias}$	1.20 ± 0.23	bias redshift evolution parameter
$A_{\rm bias}$	2.3 ± 0.2	first bias scale-dependence parameter
k_c / Mpc^{-1}	4.3 ± 0.5	second bias scale-dependence parameter
$A^{\rm cirr}$ / Jy sr^{-1}	$(1.2 \pm 1.0) \times 10^3$	Galactic cirrus power at $\ell = 2000$ in SPIRE 1200 GHz spectrum
$n_{\rm cirr}$	2.83 ± 0.44	slope of Galactic cirrus power in SPIRE spectra ($C_\ell^{\rm cirr} \propto \ell^{-n_{\rm cirr}}$)
$A_{\rm radio}$ / μK^2	0.47 ± 0.09	amplitude of the radio Poisson power in the ACT spectrum
$A_{\rm kSZ}$ / μK^2	7.8 ± 6.4	amplitude of the kinematic Sunyaev Zel'dovich angular power spectrum at $\ell = 3000$

Table 5.3: CIB source parameter correlation matrix

	α_{LF}	σ_{LF}	$\log L_0$	ε_L	ζ_L	$\log \Phi_0$	ε_Φ	ζ_Φ	T_0	ε_T	ζ_T	T_b	β	f_b	b_0	$\varepsilon_{\mathrm{bias}}$	A_{bias}	k_c
α_{LF}	100	-64	90	0	-3	52	-3	4	-8	-12	13	11	-24	27	-25	0	9	-6
σ_{LF}	-64	100	-75	-7	2	-24	8	-3	11	13	-16	-12	18	-9	20	-10	-16	9
$\log L_0$	90	-75	100	-33	29	23	25	-24	15	-23	17	1	-4	33	-23	1	10	-8
ε_L	0	-7	-33	100	-97	62	-90	89	-44	39	-26	10	-23	-30	1	6	3	1
ζ_L	-3	2	29	-97	100	-59	89	-92	37	-43	34	-7	18	24	-4	-1	-1	-1
$\log \Phi_0$	52	-24	23	62	-59	100	-70	65	-13	8	-4	9	-7	-7	-13	6	4	2
ε_Φ	-3	8	25	-90	89	-70	100	-97	15	-16	12	-3	-3	20	-2	-5	-2	-3
ζ_Φ	4	-3	-24	89	-92	65	-97	100	-16	20	-15	3	2	-18	7	-2	2	2
T_0	-8	11	15	-44	37	-13	15	-16	100	-34	11	-65	86	-4	7	-3	-8	3
ε_T	-12	13	-23	39	-43	8	-16	20	-34	100	-94	-21	-3	-53	-9	16	-6	-3
ζ_T	13	-16	17	-26	34	-4	12	-15	11	-94	100	25	-18	49	8	-16	10	1
T_b	11	-12	1	10	-7	9	-3	3	-65	-21	25	100	-61	29	-11	2	10	-1
β	-24	18	-4	-23	18	-7	-3	2	86	-3	-18	-61	100	-28	8	2	-8	2
f_b	27	-9	33	-30	24	-7	20	-18	-4	-53	49	29	-28	100	-0	-11	-0	3
b_0	-25	20	-23	1	-4	-13	-2	7	7	-9	8	-11	8	-0	100	-90	-52	42
$\varepsilon_{\mathrm{bias}}$	0	-10	1	6	-1	6	-5	-2	-3	16	-16	2	2	-11	-90	100	31	-26
A_{bias}	9	-16	10	3	-1	4	-2	2	-8	-6	10	10	-8	-0	-52	31	100	-87
k_c	-6	9	-8	1	-1	2	-3	2	3	-3	1	-1	2	3	42	-26	-87	100

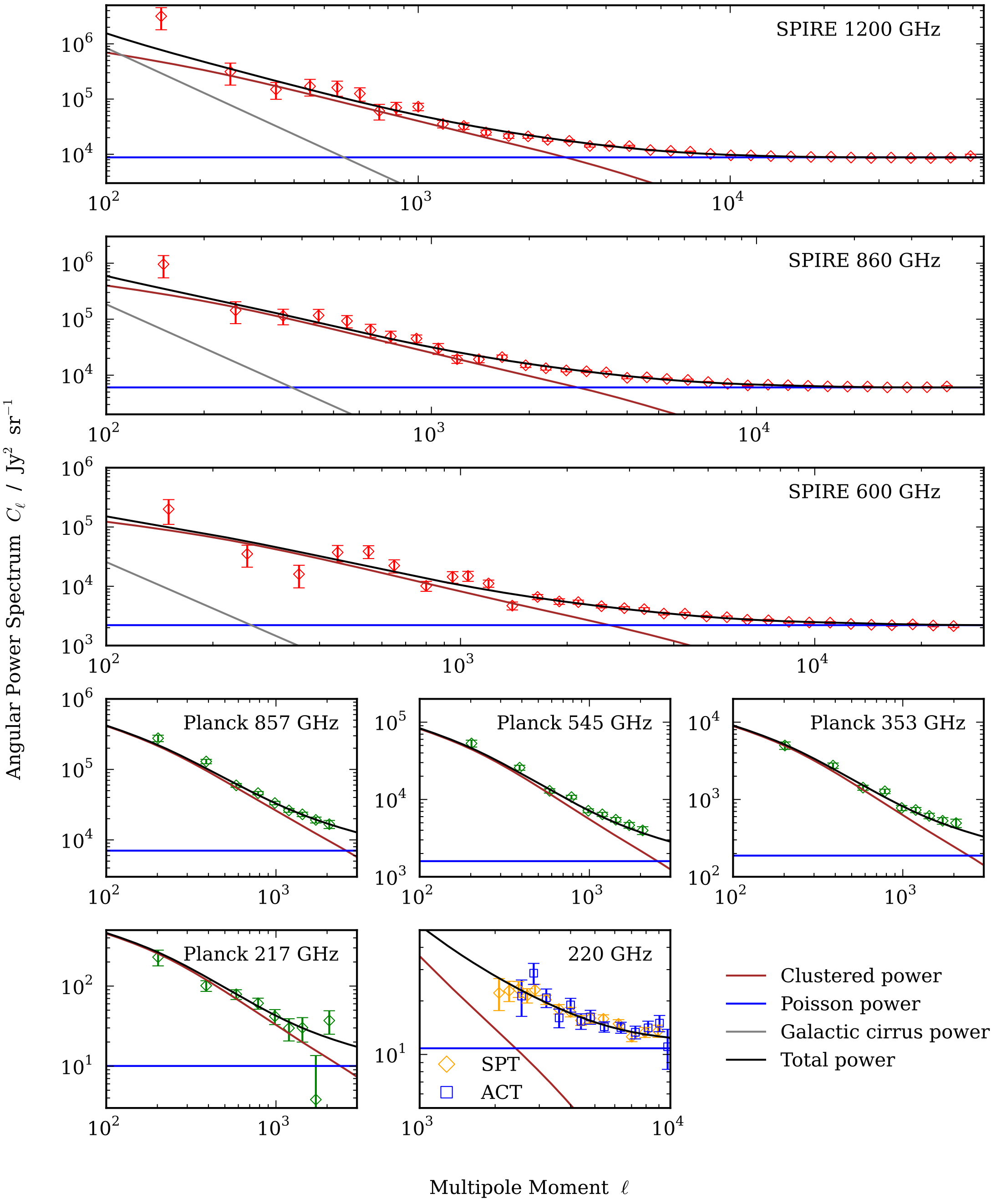

Figure 5.1: Angular power spectra from *Herschel*-SPIRE (Amblard et al., 2011), *Planck* (Planck Collaboration et al., 2011c), ACT (Das et al., 2011a) and SPT (Reichardt et al., 2012b), with our best-fit model overplotted. The power spectra consist of a Poisson component, which is independent of angular scale, and a clustered component, which varies with ℓ roughly as a power law over a wide range of scales. The best-fit Galactic cirrus power in the SPIRE spectra is also shown. The bandpower uncertainties do not include uncertainties in map calibration (see discussion in Section 5.4.1). SPIRE bandpowers from $\ell < 2000$ were not included in the fit (see Section 5.3), but are shown here for comparison. The kinematic Sunyaev Zel'dovich effect, Galactic cirrus and radio source power contribute at 220 GHz but are highly subdominant to the dusty galaxy contribution. The primary lensed CMB has been subtracted from the SPT and ACT bandpowers (see Section 5.3.4).

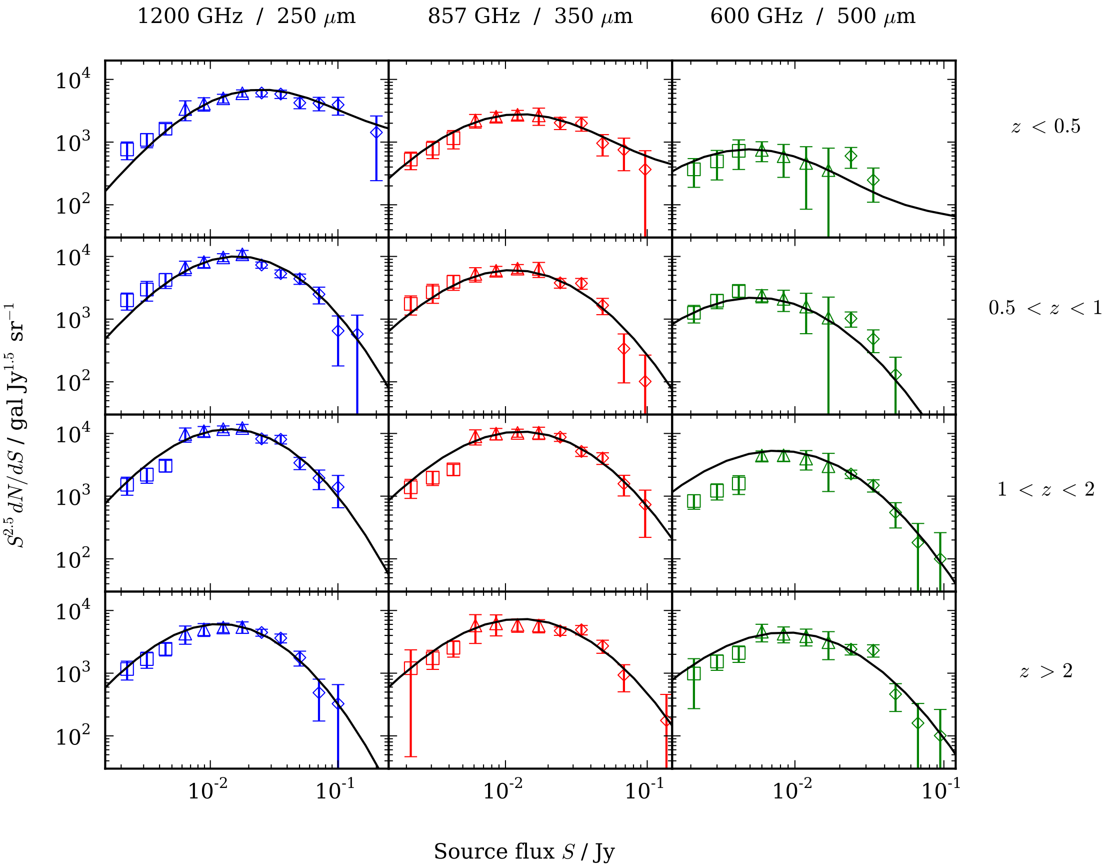

Figure 5.2: Differential number counts from *Herschel*-SPIRE (Béthermin et al., 2012b), obtained from a stacking analysis of the GOODS-N (squares) and COSMOS (triangles) fields, and by counting resolved sources in COSMOS (diamonds), with our best-fit model overplotted. The best-fit calibration values have been applied to the measured counts, as have corrections for source SED and the SPIRE bandpass filter transmission, as described in Section 5.3. The GOODS counts were not included in the fit shown (the baseline model fit) because of the difficulty in quantifying cosmic variance uncertainty (Section 5.3.7).

only at the 1.3σ level of significance. Future data, and a more rigorous exploration of possible luminosity function shape parameterisations, are required to establish whether our result is hinting at evolution in the dust LF.

Our constraint on $\sigma_{\rm LF}$, which determines the bright-end behaviour, of 0.37 ± 0.02 is, unsurprisingly, tighter, and in fairly good agreement with B11, who found $\sigma_{\rm LF} = 0.406 \pm 0.019$. We find no significant evidence for evolution in $\sigma_{\rm LF}$ when we allow a power law dependence on $1+z$; the constraint obtained on the evolution index is $-0.09^{+0.12}_{-0.10}$.

Figure 5.4 shows the evolution of L_c with redshift, including 1σ uncertainty contours. One limitation of our adopted redshift evolution is that it may not be allowing sufficiently rapid evolution at high redshift. To at least partially assess this, we have also plotted $L_c(z)$ when we deliberately over-parametrize the L_c and Φ_c evolution by adding third order terms in $\ln(1+z)$ to the series expansion for each (see equation 5.1). The individual red and blue curves show $L_c(z)$ for two fixed models, which feature a peak in $L_c(z)$ at redshift $z \sim 2$ and $z \sim 2.5$, respectively, but with low-redshift behaviour perfectly consistent with our baseline model. Even allowing additional orders in the evolution of Φ_c to compensate the lack of freedom in the evolution of L_c, these models are strongly disfavoured, at the 8σ and 5σ levels, respectively.

It is possible that our results are being biased by our simplistic SED treatment, or failing to explicitly account for multiple CIB source populations. We do not attempt further interpretation, for instance inferring the star formation rate density, in the present work, however, our findings suggest that joint fits to the number counts and power spectra can provide meaningful constraints on the evolution of the dust luminosity function at high redshift. This approach is completely independent from existing analyses using direct luminosity measurements of resolved sources (for recent examples using *Spitzer* data, see, e.g., Magnelli et al., 2011; Patel et al., 2012).

The comoving bolometric dust luminosity density is shown as a function of redshift in the lower panel of Figure 5.4. Also plotted are various constraints on the bolometric IR luminosity density from existing analyses. As stated in Section 5.2, we have considered only the thermal dust emission in this work; the bolometric IR luminosity includes contributions down to 8 μm, which we are not probing with the data considered here. The discrepancy at the tens of per cent level between our $\rho_{\rm dust}$ and the $\rho_{\rm IR}$ results from the literature at $1 < z < 2$ is probably at least partially explained by Doppler-broadened

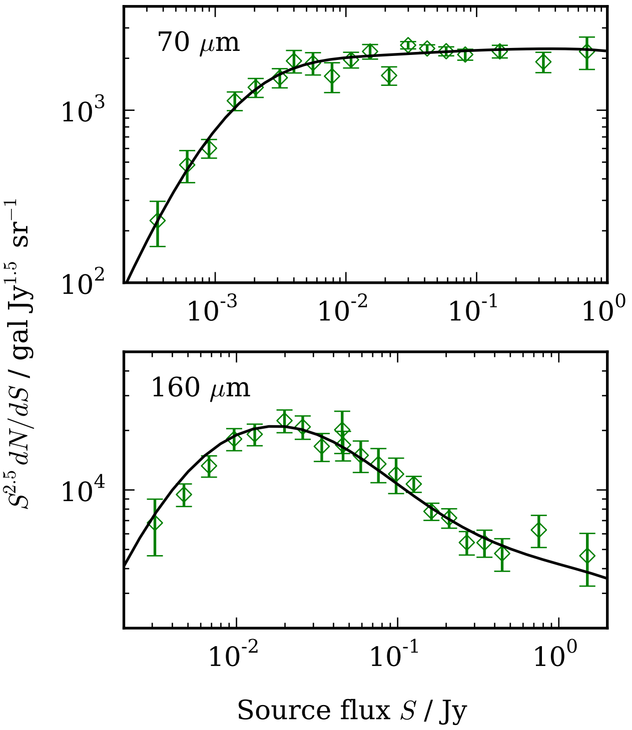

Figure 5.3: Differential number counts from *Spitzer*-MIPS (Béthermin et al., 2010), with best-fit model overplotted. The counts are corrected for best-fit calibration, source SED and bandpass filter, as in Figure 2 (see Section 3), although these corrections are small at the MIPS frequencies.

line emission, notably PAH features, contributing significantly to the rest-frame MIR SED at $\lambda \lesssim 25\ \mu$m (e.g., Lagache et al., 2004; Elbaz et al., 2011, see also Figure 1.3).

5.4.3 Spectral energy distribution

We have been able to place tight constraints on our adopted dust parameters, with a second dust component, and evolution of the temperature of the 'a' component also strongly required; at low-redshift, T_a is roughly constant (actually, decreasing slightly, although this is likely an artefact of our parameterisation of the redshift evolution), but, at higher redshift, it increases sharply, such that, by $z \sim 4$, it is as hot as the 'b' component, with $T \sim 50$ K. It seems possible that the evolution in T_a is due not an evolution in the actual dust population, but to the increase in $L_c(z)$; a strong correlation between temperature and luminosity has been observed in various studies (e.g., Blain et al., 2003; Hayward et al., 2012; Greve et al., 2012, and references therein). This could explain why, for instance, there is good consistency between

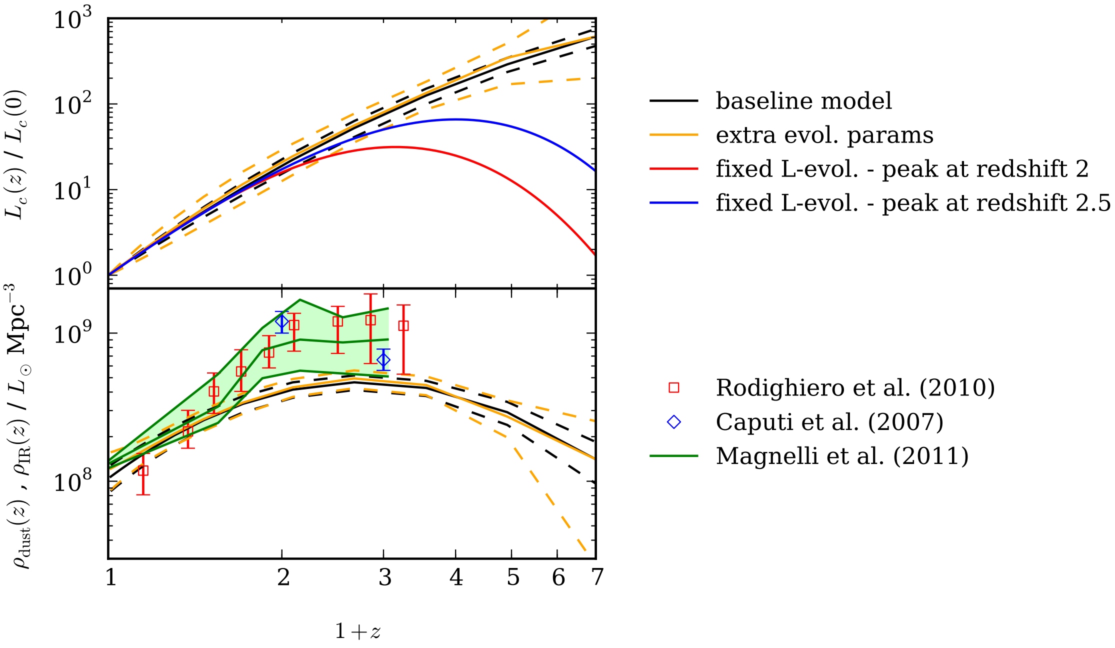

Figure 5.4: Redshift evolution of characteristic dust luminosity, L_c (upper panel) and comoving dust luminosity density, ρ_{dust} (lower panel). Model predictions are shown for the baseline model and for an alternative model in which an additional evolution parameter is allowed in both the characteristic luminosity, and the LF normalisation, Φ_c. The red and blue lines in the upper panel show two models for $L_c(z)$ chosen to feature peaks at $z \sim 2$ and 2.5 (see text). We include several measurements of the bolometric IR density from recent work using *Spitzer* observations (Caputi et al., 2007; Rodighiero et al., 2010; Magnelli et al., 2011).

the shape of our LF at the bright end (σ_{LF}) and that found by B11, despite the fact that, in our model, dust properties evolve with redshift but not luminosity, while, in their work, dust temperature evolves with luminosity but not redshift.

Regardless of the physical origin, it appears that *some* kind of SED evolution is certainly required. To demonstrate this, we consider a range of alternative SED models. We find that a single-T, single-β model, with no redshift evolution, and this same model but with a modified Wien tail, featuring a power law in frequency falling as ν^{-2}, as in Hall et al. (2010) and Shang et al. (2012), are rejected at the $> 10\sigma$ level. Clearly, these models are valid only over narrow frequency ranges, which may go some way to explain why Shang et al. (2012) were unable to find a good fit the *Planck* spectra. A two-component dust model, but with no evolution in T_a, is similarly disfavoured at the $> 10\sigma$ level. We find that the evolution in temperature cannot be substituted with an evolution in emissivity index , β, or a different β

for the ‘a’ and ‘b’ components. We note that, in the latter case, the ‘b’ component emissivity index is poorly constrained, since, on the Rayleigh-Jeans side of the dust SED, it is largely dominated by the ‘a’ component.

We find that two alternative SED parameterisations yield comparable goodness-of-fit to our baseline model ($\Delta\chi \lesssim 5$). Firstly, we consider allowing f_b, rather than T_a, to evolve with redshift (and allowing for CMB heating of the ‘a’ dust as in Blain, 1999a). In this case, the preferred temperatures of the two dust components are similar to the baseline model at $z = 0$ ($\sim 20 - 25$ K and $40 - 45$ K), and the relative importance of the hot component (through f_b) increases rapidly at high redshift, leading to the same qualitative behaviour as in the baseline model. We also find that fitting for a power-law modification to the Wien tail, with free index, $\alpha_{\rm MIR}$, as discussed above, but with allowing second order evolution in T, yields similar results to the baseline model, with $\alpha_{\rm MIR} = 2.0 \pm 0.2$, in good agreement with the value adopted in existing work. In this case, the temperature of the dust at redshift zero is several σ higher, at around 30 K, and evolves in redshift in the same qualitative way as the ‘a’ dust component in the baseline model. We find no evidence for evolution in $\alpha_{\rm MIR}$ when we adopt this parameterisation, and we likewise find no evidence for evolution in T_b in the baseline model. The data thus do not strongly discriminate between a hotter temperature component and a phenomenological power-law modification to the SED Wien tail, although evolution of the dust temperature is required in both cases. We finally note that allowing a modified MIR index *in addition* to explicitly parameterising a second temperature component does not lead to improvements in the model likelihood for the data considered.

While, as stated in Section 2, and discussed here, the extent to which our SED parameters can be associated with physical parameters is unclear, what our results demonstrate is that the counts and power spectra are capable of constraining the mean dust SED at high redshift. It is also encouraging that our dust temperature and emissivity constraints show good general agreement with the $T \sim 30 - 60$ K and $\beta \sim 1.5 - 2$ obtained in SED fits to FIR and submm-selected galaxies (e.g., Dunne & Eales, 2001; Chapman et al., 2005; Coppin et al., 2006; Chapin et al., 2011; Greve et al., 2012). The SED constraints obtained in our model hinge on the use of data covering a wide range of frequency; in this work, the submillimeter and microwave-band power spectra provide considerable improvement over the SPIRE and MIPS counts alone (see Section 5.5.5). Deep counts at lower frequencies than SPIRE (for instance, from the SCUBA-2 – Cosmology Legacy Survey[c]) could likely fulfil this role to some extent as well, provided the effect of strong lensing on the bright-end counts can be robustly treated.

5.4.4 Clustering properties

Figure 5.5 shows our constraint on the evolution of the large-scale CIB source bias. Also shown are the bias values for dark matter haloes at several fixed masses as a function of redshift, using the parametric fit to N-body simulations presented by Tinker et al. (2010a). Our results are consistent with dusty sources inhabiting haloes of mass $12.5 \lesssim \log M_{\rm halo}/M_\odot \lesssim 13.0$, which matches or slightly exceeds the mass scales found for optimal star formation in recent studies (e.g., Wang et al., 2012; Béthermin et al., 2012a; Behroozi et al., 2012). A large number of fainter sources occupying more massive groups and clusters is likely to lead to an increase in the effective bias we have measured. We also find that lower values of b_0, corresponding to a lower characteristic halo mass, are allowed if we introduce a correlation between CIB source dusty luminosity and bias (see Section 5.2.3). As an example, we consider a correlation of the form

$$\langle b_{\rm gal}(k,z) j_\nu(z)\rangle_{\rm cut} = \langle b_{\rm gal}(k,z)\rangle \left[\langle j_\nu(z)\rangle_{\rm cut} + \gamma_{\rm corr}(1+z)\chi^2 \int_0^{S_{\rm cut}} dS_\nu \frac{dL}{dS_\nu}\frac{\Phi(L,z)}{L\ln 10}\left(\frac{S_\nu^2}{S_{{\rm c},\nu}} - S_\nu\right)\right], \tag{5.25}$$

where $\gamma_{\rm corr}$ is a free parameter, which may be positive or negative, and $S_{{\rm c},\nu} = S_\nu(L_c)$, such that the term in parenthesis increases as the relative importance of the more luminous sources increases. We find that the uncertainty in b_0 increases by 50%, and that the mean value decreases by around 1σ, with a mild preference for a positive value of $\gamma_{\rm corr}$. As stated in Section 5.2.3, the data do not show a preference for an $L - b_{\rm gal}$ correlation in terms of goodness-of-fit. Further work, involving more detailed modelling of the CIB source clustering properties, is required to explore the relation between dust luminosity and halo mass in more detail.

We consider the effect of fixing the redshift evolution of the bias to be of the form $b(z) = 1 + C/D(z)$, where C is a constant and $D(z)$ is the linear growth rate (Bond et al., 1991a; Fry, 1996). This form, adopted in our initial fit to the BLAST and BLAST × ACT data in Chapter 2, is appropriate for a population that forms at a single redshift, and whose evolution is not driven by mergers (such that the

---

[c] http://www.jach.hawaii.edu/JCMT/surveys/Cosmology.html

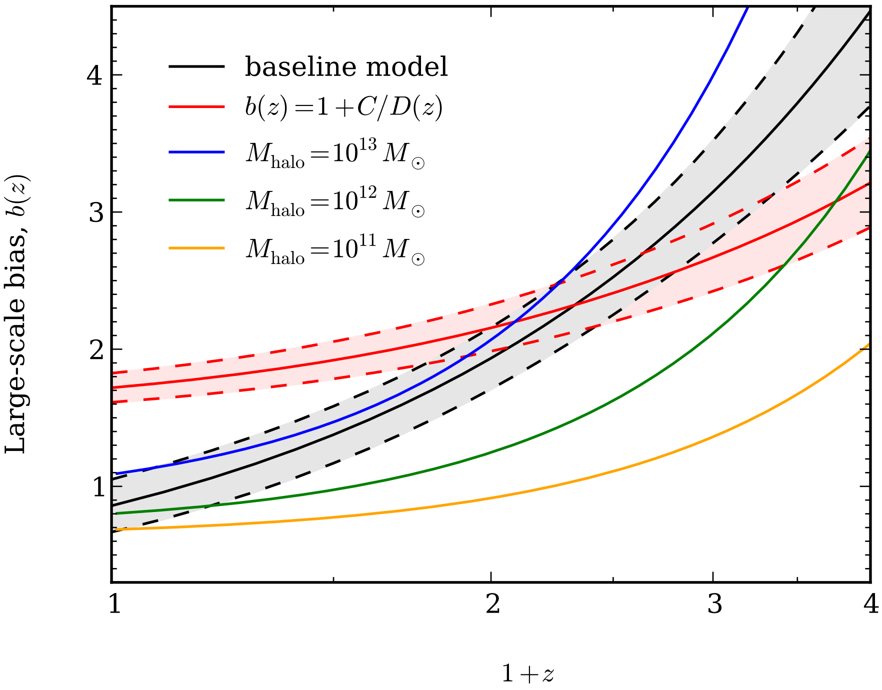

Figure 5.5: Evolution of CIB source bias inferred from our baseline model, and from repeating our fit with an alternative parameterisation of the redshift-evolution (see text). The bias of haloes of several fixed masses, taken from Tinker et al. (2010a), are also shown as a function of redshift.

number of sources is conserved). The current data prefer (at the 2.8σ level) a more rapid evolution in the bias, which would be consistent with mergers playing a significant role in CIB source evolution, as inferred by Engel et al. (2010) and assumed in various models, including, for instance, that of Righi et al. (2008).

The data very strongly require scale-dependent bias, which was to be expected given we already found that linear clustering was rejected by the *Planck* and BLAST data in Chapter 3. We investigated the effect of using the nonlinear matter power spectrum, calculated using HALOFIT from the CAMB distribution, in the clustered power calculation, rather than the linear power spectrum. We find that, while the parameters determining the scale-dependence of the clustering power are significantly affected, there are only minor shifts in the LF and SED parameters, at the level of several tens of percent of a σ, and that a preference for scale-dependent biasing remains at the $> 3\sigma$ level.

5.5 Discussion

In this section, we first compare our model's prediction with several measurements outside those used to constrain it. We then investigate the importance of the various components (counts, clustered power, Poisson power) in constraining our model and consider the implications of our results for future work.

5.5.1 Integrated CIB intensity

The integrated CIB intensity, clustered anisotropy power and Poisson anisotropy power each receive different contributions from different populations of sources, with the brightest sources making a larger relative contribution to the Poisson power, for instance. Our model correctly reproduces the anisotropy power spectra over a range of frequency; an obvious question is whether it also reproduces the integrated CIB intensity. A comparison with a fit to FIRAS measurements from Fixsen et al. (1998) is made in Table 5.4. There is consistency within $1-1.5\sigma$ over a wide range of frequency. Our model predictions are systematically lower than the Fixsen et al. (1998) values, however since we are comparing not to the FIRAS data directly, but a parametric fit, the uncertainties in the right-hand column are not independent. Also, note that the low-frequency FIRAS data are very noisy, and that this is not reflected in the uncertainty in the 150 GHz fit value; alternative fits to the FIRAS data have found significantly lower values (e.g., the fit by Gispert et al., 2000, yields 0.0095 ± 0.0029 MJy sr^{-1} at 150 GHz).

In principle, we could have used the FIRAS data to constrain the model, along with the spectra and number counts; we did not consider this because the *Planck* 857 and 545 GHz maps were calibrated from the FIRAS measurements, and thus any systematic present in the FIRAS data could have effectively entered our modelling twice.

5.5.2 Bolometric IR luminosity function

Local bolometric IR luminosity function measurements ($z \leq 0.2$) derived from SPIRE (Vaccari et al., 2010) and *Spitzer* (Patel et al., 2012) measurements are plotted in Figure 5.6. The large uncertainty in the model predictions at the faint-end is discussed in Sections 5.2.1 and 5.4.2, and does not prevent us from making meaningful predictions for a range of statistics. There is a discrepancy between our model and the *Spitzer* measurements at intermediate luminosities, which may be connected to possible

Table 5.4: Integrated CIB intensity predictions

Frequency (GHz)	Prediction MJy sr^{-1}	Fit to FIRAS† MJy sr^{-1}
150	0.0065 ± 0.0005	0.020 ± 0.005
600	0.360 ± 0.032	0.395 ± 0.072
1050	0.748 ± 0.059	0.792 ± 0.098
1500	0.741 ± 0.077	0.866 ± 0.055
1950	0.582 ± 0.070	0.690 ± 0.035
2400	0.431 ± 0.059	0.455 ± 0.050

† CIB SED fit to FIRAS data, from Fixsen et al. (1998)

evolution in the shape of the luminosity function discussed in Section 5.4.2, as our model is primarily constrained by data at $z \gtrsim 1$. It should also be noted, though, that the data points shown assume a (fixed) source SED, which may be biasing the inferred bolometric luminosity function values.

5.5.3 Power spectra at lower frequencies

As stated in Section 3, we limited our analysis to spectra containing negligible contribution from the Sunyaev Zel'dovich effect or its cross-correlation with CIB sources. A good test of our model assumptions is to extrapolate the power spectrum predictions to lower frequencies. We compare our predictions with the constraints obtained by Reichardt et al. (2012b) in Table 5.5. The predictions were made assuming removal of sources above 6.4 mJy in the 150 GHz map. We compare to the SPT measurements obtained when a correlation between the thermal Sunyaev Zel'dovich effect and CIB sources is allowed, since we found in Chapter 4 that such a correlation may be expected at the 10–20% level in units of power. The is good consistency between our predictions and the SPT measurements, and our constraints, at least on the clustered power amplitude, are competitive with the direct measurements. This suggests that extending our model to include the lower frequency ACT, SPT and *Planck* data (at $\nu < 220$ GHz) may improve constraints both in the dust emission model parameters, and on secondary anisotropies like the Sunyaev Zel'dovich effect.

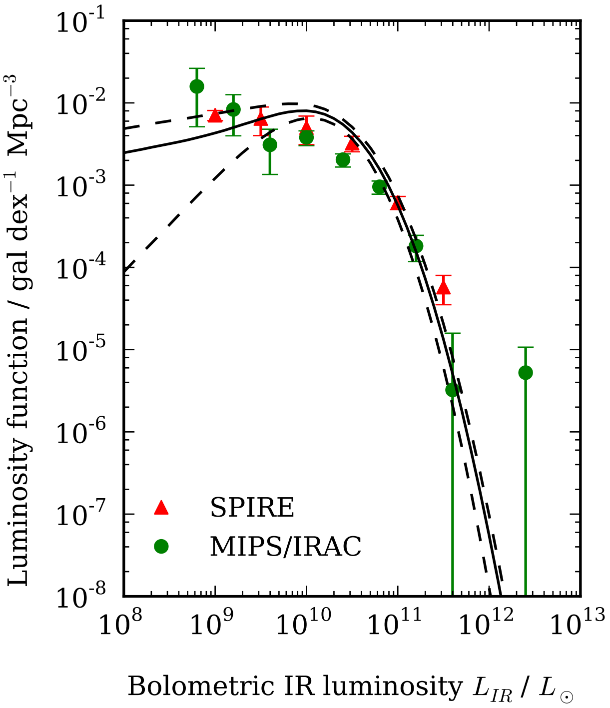

Figure 5.6: Local ($z \leq 0.2$) bolometric IR luminosity function derived using measurements from *Herschel*-SPIRE (Vaccari et al., 2010) and *Spitzer*-MIPS/IRAC (Patel et al., 2012), with our baseline model mean and 1σ confidence contour predictions over-plotted. There is good agreement between the faint and bright-end measurements and our model; the apparent discrepancy with the *Spitzer* measurements at intermediate luminosities may be connected to evolution in the LF shape.

Table 5.5: Power spectrum predictions for lower frequencies (in units of $\ell(\ell+1)C_\ell/2\pi|_{\ell=3000}$, in μK^2)

		Prediction	Measured[†]
150 GHz	Poisson	9.25 ± 0.77	8.05 ± 0.48
	Clustered	6.60 ± 0.70	6.73 ± 0.73
95 GHz	Poisson	1.24 ± 0.19	1.04 ± 0.15
	Clustered	0.87 ± 0.15	0.87 ± 0.17

[†] SPT constraints from Reichardt et al. (2012b)

5.5.4 Kinematic Sunyaev Zel'dovich constraints

The data mildly prefer a positive value of the kSZ power, with $A_{\mathrm{kSZ}} = 7.6 \pm 6.4\ \mu\mathrm{K}^2$. While this is consistent with existing predictions and measurements (e.g., Reichardt et al., 2012b; Mesinger et al., 2012), the uncertainty is too large for the constraint to be useful. We find that the kSZ amplitude is not highly correlated with any of the dust model parameters, meaning that there is no single quantity which, if better known, would lead to a substantial improvement in the kSZ constraint. While constraining the kSZ power spectrum from data free from the tSZ is an attractive idea, it would appear that, at least currently, this is not feasible, given the small size of the kSZ power relative to the dust at 220 GHz. The outlook for improving kSZ constraints using lower frequency data is considerably more positive, however, because our model predicts high coherence in dust emission over a wide range of frequency (see Section 5.5.6, below).

5.5.5 The signal in the shot-noise

An interesting result from our work is the constraining power that is carried by the Poisson component of the high-resolution spectra (mainly SPIRE, but also ACT and SPT). To illustrate this, Figure 5.7 shows two-dimensional parameter constraints, with contours enclosing 68% and 95% of the samples, for a selection of our model parameters. We show constraints from three models: the baseline model, described in Section 5.2, a model constrained from the SPIRE and MIPS number counts alone, and a model constrained by the counts plus clustering power only. In this third model, the Poisson power in each of the nine power spectra is allowed to vary as an additional free parameter. The results of this comparison can be summarised as follows: including the clustered power leads to a significant improvement in SED parameter constraints over the counts alone, and inclusion of the Poisson power in the fit leads to moderate further improvements in the SED parameters constraints, and large improvements in the bias parameter constraints.

We also find that the model likelihood is not sufficiently improved by treating the Poisson levels independently to warrant any preference for this approach on goodness-of-fit grounds ($\Delta\chi^2 = 10$ for 9 fewer degrees of freedom). Furthermore, there is excellent consistency between the results from the three models for every parameter. This is a useful test of at least two features of our model. Firstly, it suggests

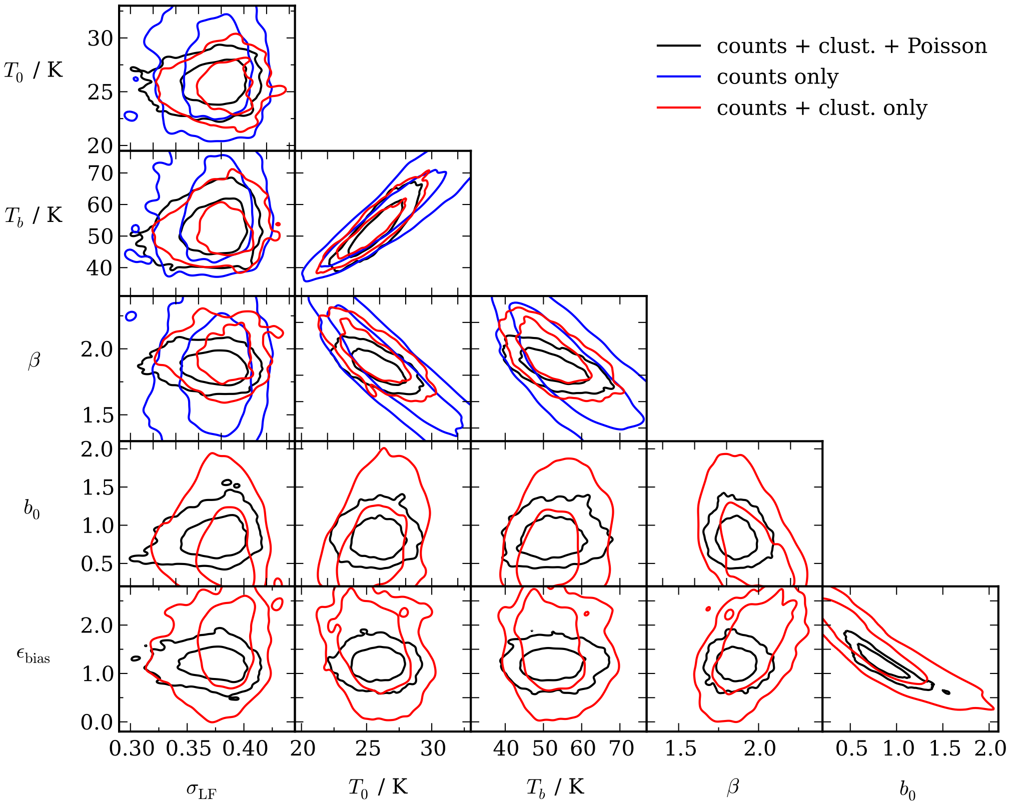

Figure 5.7: Two-dimensional parameter constraints for a selection of the dusty source model parameters. Contours containing 68% and 95% of the MCMC samples are shown for the baseline model, fit to number counts, clustered power and Poisson power, and two alternative models, one fit to the counts only and one to the counts and clustered power only. Requiring the model to reproduce the observed Poisson power significantly tightens constraints on a range of parameters, particularly those relating to the dusty source SED or clustering properties. There is excellent consistency between the constraints obtained in each of the three fits.

that our results are not significantly biased by our treatment of bright source masking prior to power spectrum calculation (see Section 5.2.5). Secondly, it suggests that the fact that we have not explicitly accounted for a dusty galaxy duty cycle in our model (which would impact most heavily on the predicted Poisson power – see, e.g., discussion in Shang et al., 2012) is not significantly affecting our results.

5.5.6 Redshift distribution of power and intensity

Figure 5.8 shows the redshift distribution of clustered and Poisson anisotropy power, and CIB intensity, as a function of frequency, for our best-fit model parameters. Our model predicts that, as expected, lower frequencies receive greater relative contribution from higher redshifts (e.g., Knox et al., 2001), but, interestingly, there is only moderate evolution in the distribution over the submm and microwave bands. Physically, this corresponds to a high degree of coherence in the dust emission across this frequency range; we predict, for instance, a correlation of 80-90% between the dust anisotropy power at 857 GHz and 217 GHz, with the clustered power more strongly correlated than the Poisson (as can be seen from Figure 5.8). This is an important result, because it suggests that much of the dust that acts as a foreground contaminant for current CMB temperature cosmology (hampering detection of the kSZ power spectrum, for example) may be removed either by direct cross-correlation of microwave maps with maps at higher frequencies, or understood through a joint fit with the high-frequency, dust-dominated data. We note that the degree of submm / mm correlation is moderately dependent on the SED parameterisation; we find that, if, for example, the evolution of the SED is parametrized through evolution in f_b, rather than T_a (see Section 5.4.3, above), the correlation in the Poisson anisotropy power is $\sim 70\%$.

The most direct test of this prediction is comparison with the power spectra from cross-correlating microwave and submm maps; in Chapter 2 we described such spectra from the cross-correlation of ACT and BLAST maps. We repeated our model fitting including the BLAST × ACT 218 GHz spectra and found that our baseline model provides a good fit ($\Delta\chi^2 = 25$ for 27 additional bandpowers, treating the BLAST map calibration parameters as described in Section 5.3.3). This is consistent with the high degree of correlation preferred by most of the ACT / BLAST cross-spectra in Sections 2.6 and 3.4.2, however, the BLAST × ACT bandpowers are noisy, and future cross-correlations (from *Planck*, or from cross-correlating SPIRE maps with ACT or SPT) will provide a stronger test of our prediction, as well as possibly discriminating more strongly between different parameterisations of the SED evolution.

It is important to note that the high-redshift fall-off in power at the FIR and microwave ends of the frequency range shown in Figure 5.8 have different physical origins. In the FIR, the decrease at $z \gtrsim 1$ comes not from a lack of sources at higher redshift, but because the dust SED is being probed beyond its peak, meaning observed flux drops rapidly with increasing redshift. In contrast, the microwave bands

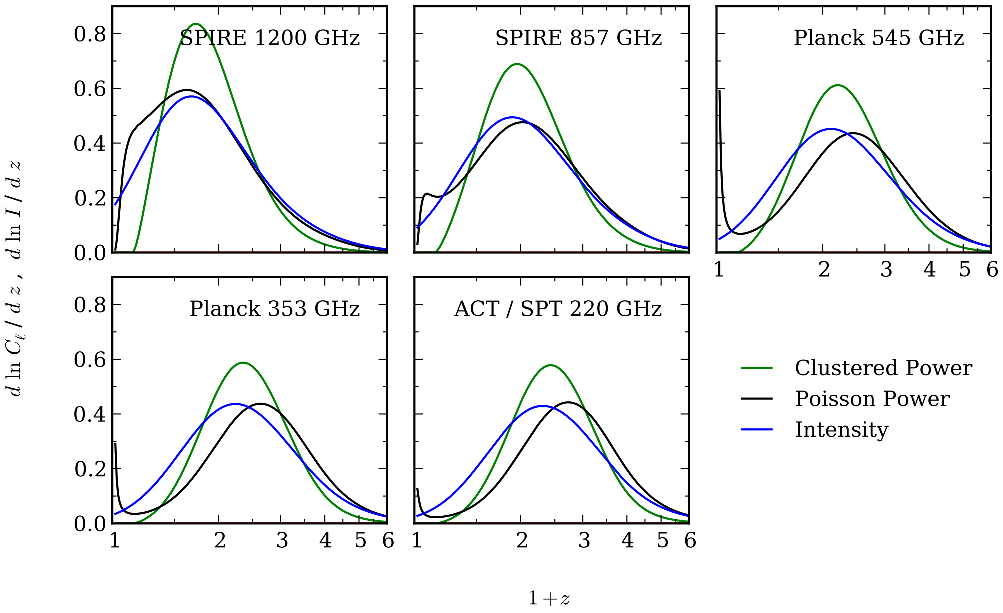

Figure 5.8: Redshift distribution of clustered anisotropy power, Poisson anisotropy power, and dust emission intensity predicted by our model, normalised such that the area under each curve is unity. The redshift dependence of the clustered power is shown at $\ell = 3000$, although the redshift distribution does not vary strongly with scale over the range of scales where the clustered power contributes significantly to the total spectrum. A few per cent of the Poisson power in the *Planck* spectra is predicted to originate from low-redshift sources that are below the source removal limit, although in each case the Poisson power remains convergent. The high degree of overlap between the curves at different frequency corresponds to a high degree of coherence in the dusty galaxy emission over the submillimeter and microwave bands. This is an important prediction of our model (see text).

never probe beyond the rest-frame peak of the SED, and the fall-off in the curves at high redshift arises simply from a decreasing number of sources, which overcomes their rising luminosity and microwave brightness. This behaviour is reflected in the change in the redshift distribution of the Poisson power, which receives a higher weighting from rare bright objects than numerous faint ones, compared to the intensity and clustered anisotropy power.

5.5.7 Model limitations and future work

A large assumption in our modelling is that the dusty sources can essentially be treated as a homogenous population, whose average properties vary smoothly over time. Much of our constraining power is in the form of integrated quantities (the power spectra), meaning our results are probably not especially sensitive to rare, extreme objects (which could distort results obtained from a flux-limited study), but it is not clear that our model would correctly capture a sharp transition in either dust or clustering properties, which features in some existing work. In the model developed by Granato et al. (2004), Lapi et al. (2011), and Xia et al. (2012), for instance, highly-clustered, massive, proto-spheroidal galaxies dominate the dusty galaxy population at high-redshift, but cease to exist at $z < 1$, where merger-driven starbursts and (eventually) spiral galaxies take over. Allowing more explicitly for multiple source populations, with separate emission or clustering properties, is a clear improvement we can consider in future work.

The possible limitations of our SED parameterisation have already been discussed (Sections 5.2.2 and 5.4.3). As noted in Section 1.4, ALMA will greatly improve our understanding of the processes relating to dust-enshrouded star formation on galaxy scales, and may enable us move on from the gray-body approximation to a more physical dust emission treatment. Additionally, extending our model to include higher frequencies, incorporating non-thermal dust contributions to the SED and bolometric IR luminosity, will facilitate comparison with infrared luminosity density and star formation rate constraints from other work.

A wide range of data sets will be available to improve constraints on high-redshift dust emission over the coming years; the first release of *Planck* maps, covering the entire sky (rather than just the ~ 140 deg^2 used for the spectra we have included here), is expected in early 2013. Spectra from these maps, in addition to future *Herschel*, ACT, SPT, ACTPol and SPTpol spectra (among others), will significantly improve constraints over those considered here. Future number counts, from additional SPIRE fields, as well as, for example, SCUBA-2, will also give much-needed improved constraints on the properties of the fainter sources. Using measurements of the angular correlation function of bright sources in flux-limited samples (e.g., Cooray et al., 2010; Maddox et al., 2010; Guo et al., 2011) in conjunction with angular power spectra will allow us to improve constraints on the $L - b_{\rm gal}$ correlation.

A host of cross-correlations, including those already mentioned in Chapter 4, using other tracers of large-scale structure, such as reconstructed CMB or galaxy weak lensing deflection maps, or optical data from the SDSS, will also add constraining power, in addition to being sensitive to different combinations of model parameters from the counts and spectra. The framework presented in Section 5.2, which features fully parametrized descriptions for the LF, SED, and source bias, can be easily extended to include constraints from these additional data sets.

5.6 Conclusions

We have simultaneously constrained the luminosity function, spectral energy distribution and clustering properties of dusty CIB galaxies using a combined fit to number counts and angular power spectra from five current instruments – *Spitzer*, *Herschel*, *Planck*, ACT and SPT. Our model allows us to predict the clustering and Poisson components of the power spectrum over a wide range of frequency and angular scales. While our model is based on fairly simple, phenomenological, parameterisations, it has yielded a number of important results, which we summarise here:

(i) We have demonstrated the ability of joint fits to counts and spectra to constrain the evolution of the dusty source luminosity function at high redshift, complementing approaches that rely on studying the rare, bright, resolved galaxies directly.

(ii) We predict a high (up to $\sim 90\%$) degree of coherence in the dust emission across the submm and microwave bands. While future data is needed to test this result, if true, it would suggest that cosmological constraints from CMB temperature anisotropy measurements that are hampered by the CIB can be greatly improved through measurements or models of the dust emission using data at higher frequencies.

(iii) Substantial constraining power may be lost if the Poisson anisotropy power measured by high-resolution instruments like SPIRE, ACT and SPT is treated simply as noise; we have shown that including the Poisson power in our fit results in improvements in a number of model parameters. The fact that there is good consistency between the parameter constraints with and without including the Poisson in the fit suggests that our results are not being strongly affected by uncertainties in the modelling of the bright source masking or failure to explicitly account for a dusty galaxy duty cycle.

(iv) The data strongly require evolution in dust properties; for our simple two component dust model, most of the dust luminosity at low-redshift is from dust at around 25 K, however, a hotter dust component at around 50 K, is also required. At $z \gtrsim 2$, the temperature of the colder component increases, such that by $z \sim 4$ it too is at ~ 50 K. It is encouraging that these temperatures appear roughly consistent with those obtained in SED fitting to individual galaxies, although further work is required to establish the extent to which our SED parameters can be associated with physical dust properties.

The basic approach put forward in this work, and in Chapter 3 – combining data from a range of instruments, with a rigorous treatment of systematic uncertainties (Section 5.3) – will be of great importance for realising the potential of future data sets.

Conclusions

I have presented a range of models describing the angular power spectrum of dusty star-forming galaxies. The quality of data in this field has improved drastically over the past few years; three years ago, very little was known about the shape (scale dependence) of the clustered component. The rapid data advances have demanded increasing complexity in the models that can be constrained. The BLAST / ACT correlations presented in Chapter 2 could be described with a simple linear clustering model; when these data were combined with the *Planck* spectra, this model was then ruled out. This cross-correlation analysis was still important, however, since the realisation that there is substantial overlap between the dusty sources that contribute to the submm and mm skies is critical to the analysis in the later chapters of this thesis.

The angular power spectra of clustered dusty sources exhibits power-law behaviour over a wide range of frequency, and in Chapter 3 I exploited this fact to construct a simple template for the clustered power that is not dependent on assumptions regarding the redshift distribution or environments of the actual galaxies. This is helpful for the purposes of separating the dusty galaxy power spectrum from other contributions (including the CMB).

In Chapter 4 I described a model for the correlation between the dusty sources and the thermal Sunyaev Zel'dovich effect. The importance of this correlation for hampering constraints on the kinematic Sunyaev Zel'dovich effect has only been realised in the past 12 months, and no significant detection of the tSZ–CIB correlation has yet been made. The theoretical prediction is subject to significant uncertainties; the investigation into which physical properties are predominantly responsible for this uncertainty described in Chapter 4 will help inform future analyses as data quality improves.

The angular power spectrum has largely been used to infer the clustering properties (bias and host halo mass) of dusty galaxies in existing analyses. In Chapter 5, I presented a joint analysis of data from *Spitzer*, *Herschel*, *Planck*, ACT and SPT and showed that the angular power spectra, in conjunction with deep number counts, can also provide information about the emission properties – SEDs – of high-redshift sources. This work, and future improvements, will be of great use in constraining star formation at high redshift with the wealth of data that will become available in coming years.

Bibliography

Albrecht, A., & Steinhardt, P. J. 1982, Phys. Rev. Lett., 48, 1220

Alexander, D. M., Bauer, F. E., Chapman, S. C., Smail, I., Blain, A. W., Brandt, W. N., & Ivison, R. J. 2005, ApJ, 632, 736, arXiv:astro-ph/0506608

Amblard, A. et al. 2011, Nature, 470, 510, 1101.1080

Arnaud, M., Pratt, G. W., Piffaretti, R., Böhringer, H., Croston, J. H., & Pointecouteau, E. 2010, A&A, 517, A92, 0910.1234

Bai, L. et al. 2007, ApJ, 664, 181, 0704.0953

Bai, L., Rieke, G. H., Rieke, M. J., Hinz, J. L., Kelly, D. M., & Blaylock, M. 2006, ApJ, 639, 827, arXiv:astro-ph/0512069

Battaglia, N., Bond, J. R., Pfrommer, C., Sievers, J. L., & Sijacki, D. 2010, ApJ, 725, 91, 1003.4256

Bavouzet, N., Dole, H., Le Floc'h, E., Caputi, K. I., Lagache, G., & Kochanek, C. S. 2008, A&A, 479, 83, 0712.0965

Behroozi, P. S., Wechsler, R. H., & Conroy, C. 2012, ArXiv e-prints, 1207.6105

Benford, D. J., Cox, P., Omont, A., Phillips, T. G., & McMahon, R. G. 1999, ApJ, 518, L65, arXiv:astro-ph/9904277

Bennett, C. L. et al. 2003a, ApJ, 583, 1

——. 2003b, ApJS, 148, 97

Benson, B. A. et al. 2011, ArXiv e-prints, 1112.5435

Berlind, A. A., & Weinberg, D. H. 2002, ApJ, 575, 587, arXiv:astro-ph/0109001

Berlind, A. A. et al. 2003, ApJ, 593, 1, arXiv:astro-ph/0212357

Bersanelli, M. et al. 2010, A&A, 520, A4, 1001.3321

Béthermin, M., Dole, H., Beelen, A., & Aussel, H. 2010, A&A, 512, A78, 1001.0896

Béthermin, M., Dole, H., Lagache, G., Le Borgne, D., & Penin, A. 2011, A&A, 529, A4+, 1010.1150

Béthermin, M., Doré, O., & Lagache, G. 2012a, A&A, 537, L5, 1201.0546

Béthermin, M. et al. 2012b, A&A, 542, A58, 1203.1925

Binney, J., & Tremaine, S. 2008, Galactic Dynamics: Second Edition (Princeton University Press)

Blain, A. W. 1996, MNRAS, 283, 1340

——. 1999a, MNRAS, 309, 955, arXiv:astro-ph/9906438

——. 1999b, MNRAS, 304, 669, arXiv:astro-ph/9903221

Blain, A. W., Barnard, V. E., & Chapman, S. C. 2003, MNRAS, 338, 733, arXiv:astro-ph/0209450

Blain, A. W., Ivison, R. J., & Smail, I. 1998, MNRAS, 296, L29, arXiv:astro-ph/9710003

Blain, A. W., Smail, I., Ivison, R. J., & Kneib, J.-P. 1999, MNRAS, 302, 632, arXiv:astro-ph/9806062

Blake, C., Collister, A., & Lahav, O. 2008, MNRAS, 385, 1257, 0704.3377

Bleem, L. E. et al. 2012, ApJ, 753, L9, 1203.4808

Böhringer, H. et al. 2007, A&A, 469, 363, arXiv:astro-ph/0703553

Bond, J. R. 1996, in Cosmology and Large Scale Structure, Les Houches Session LX, ed. R. Schaeffer (London, UK: Elsevier), 496

Bond, J. R., Carr, B. J., & Hogan, C. J. 1986, ApJ, 306, 428

——. 1991a, ApJ, 367, 420

Bond, J. R., Cole, S., Efstathiou, G., & Kaiser, N. 1991b, ApJ, 379, 440

Bond, J. R., Ruetalo, M. I., Wadsley, J. W., & Gladders, M. D. 2002, in Astronomical Society of the Pacific Conference Series, Vol. 257, AMiBA 2001: High-Z Clusters, Missing Baryons, and CMB Polarization, ed. L.-W. Chen, C.-P. Ma, K.-W. Ng, & U.-L. Pen, 15, arXiv:astro-ph/0112499

Boselli, A., & Gavazzi, G. 2006, PASP, 118, 517, arXiv:astro-ph/0601108

Bracco, A. et al. 2011, MNRAS, 412, 1151, 1011.0725

Brown, M. L. et al. 2009, ApJ, 705, 978, 0906.1003

Bull, P., Clifton, T., & Ferreira, P. G. 2012, Phys. Rev. D, 85, 024002, 1108.2222

Calabrese, E., Huterer, D., Linder, E. V., Melchiorri, A., & Pagano, L. 2011, Phys. Rev. D, 83, 123504, 1103.4132

Caputi, K. I. et al. 2007, ApJ, 660, 97, arXiv:astro-ph/0701283

Carlstrom, J. E. et al. 2011, PASP, 123, 568, 0907.4445

Chapin, E. L. et al. 2011, MNRAS, 411, 505, 1003.2647

——. 2009, MNRAS, 398, 1793, 0906.4561

Chapman, S. C., Blain, A. W., Smail, I., & Ivison, R. J. 2005, ApJ, 622, 772, arXiv:astro-ph/0412573

Coil, A. L., Newman, J. A., Cooper, M. C., Davis, M., Faber, S. M., Koo, D. C., & Willmer, C. N. A. 2006, ApJ, 644, 671, arXiv:astro-ph/0607454

Cole, S. et al. 2005, MNRAS, 362, 505

Condon, J. J. 1974, ApJ, 188, 279

Cooray, A. et al. 2010, A&A, 518, L22+, 1005.3303

Cooray, A., & Sheth, R. 2002, Phys. Rep., 372, 1

Coppin, K. et al. 2006, MNRAS, 372, 1621, arXiv:astro-ph/0609039

——. 2008, MNRAS, 384, 1597, 0711.0274

Daddi, E. et al. 2007a, ApJ, 670, 173, 0705.2832

——. 2005, ApJ, 631, L13, arXiv:astro-ph/0507504

——. 2007b, ApJ, 670, 156, 0705.2831

Das, S., Hajian, A., & Spergel, D. N. 2009, Phys. Rev. D, 79, 083008, 0809.1092

Das, S. et al. 2011a, ApJ, 729, 62, 1009.0847

——. 2011b, Physical Review Letters, 107, 021301, 1103.2124

Dawson, K. S., Holzapfel, W. L., Carlstrom, J. E., Joy, M., & LaRoque, S. J. 2006, ApJ, 647, 13, arXiv:astro-ph/0602413

De Bernardis, F., & Cooray, A. 2012, ArXiv e-prints, 1206.1324

Desert, F.-X., Boulanger, F., & Puget, J. L. 1990, A&A, 237, 215

Devlin, M. J. et al. 2009, Nature, 458, 737, 0904.1201

Dicus, D. A., et al. 1982, Phys. Rev., D26, 2694

Dodelson, S. 2003, Modern cosmology (Elsevier)

Dole, H., Lagache, G., & Puget, J.-L. 2003, ApJ, 585, 617, arXiv:astro-ph/0211312

Dole, H. et al. 2006, A&A, 451, 417, arXiv:astro-ph/0603208

Draine, B. T. 2003, ARA&A, 41, 241, arXiv:astro-ph/0304489

——. 2006, ApJ, 636, 1114, arXiv:astro-ph/0507292

Draine, B. T., & Lazarian, A. 1999, ApJ, 512, 740

Dunkley, J., Bucher, M., Ferreira, P. G., Moodley, K., & Skordis, C. 2005, MNRAS, 356, 925, arXiv:astro-ph/0405462

Dunkley, J. et al. 2011, ApJ, 739, 52, 1009.0866

——. 2009, ApJS, 180, 306, 0803.0586

Dunne, L., Eales, S., Edmunds, M., Ivison, R., Alexander, P., & Clements, D. L. 2000, MNRAS, 315, 115, arXiv:astro-ph/0002234

Dunne, L., & Eales, S. A. 2001, MNRAS, 327, 697, arXiv:astro-ph/0106362

Dünner, R. et al. 2012, ArXiv e-prints, 1208.0050

Eales, S. et al. 2010, PASP, 122, 499, 0910.4279

Eales, S., Lilly, S., Gear, W., Dunne, L., Bond, J. R., Hammer, F., Le Fèvre, O., & Crampton, D. 1999, ApJ, 515, 518, arXiv:astro-ph/9808040

Efstathiou, G., & Migliaccio, M. 2012, MNRAS, 423, 2492, 1106.3208

Eisenstein, D. J., & Hu, W. 1998, ApJ, 496, 605

Elbaz, D. et al. 2011, A&A, 533, A119, 1105.2537

Engel, H. et al. 2010, ApJ, 724, 233

Fang, W., Kadota, K., & Takada, M. 2012, Phys. Rev. D, 85, 023007, 1109.4934

Fernandez, E. R., Komatsu, E., Iliev, I. T., & Shapiro, P. R. 2010, ApJ, 710, 1089, 0906.4552

Finkbeiner, D. P., Davis, M., & Schlegel, D. J. 1999, ApJ, 524, 867, arXiv:astro-ph/9905128

Fixsen, D. J. 2009, ApJ, 707, 916, 0911.1955

Fixsen, D. J., Dwek, E., Mather, J. C., Bennett, C. L., & Shafer, R. A. 1998, ApJ, 508, 123, arXiv:astro-ph/9803021

Fowler, J. W. et al. 2010, ApJ, 722, 1148, 1001.2934

Fowler, J. W. et al. 2007, Appl. Opt., 46, 3444

Friedman, R. B. et al. 2009, ApJ, 700, L187, 0901.4334

Fry, J. N. 1996, ApJ, 461, L65+

Gautier, III, T. N., Boulanger, F., Perault, M., & Puget, J. L. 1992, AJ, 103, 1313

Giavalisco, M., Steidel, C. C., Adelberger, K. L., Dickinson, M. E., Pettini, M., & Kellogg, M. 1998, ApJ, 503, 543, arXiv:astro-ph/9802318

Gispert, R., Lagache, G., & Puget, J. L. 2000, A&A, 360, 1, arXiv:astro-ph/0005554

Glenn, J. et al. 2010, MNRAS, 409, 109, 1009.5675

Gordon, K. D. et al. 2007, PASP, 119, 1019, 0704.2196

Granato, G. L., De Zotti, G., Silva, L., Bressan, A., & Danese, L. 2004, ApJ, 600, 580, arXiv:astro-ph/0307202

Greve, T. R. et al. 2012, ArXiv e-prints, 1206.4550

Griffin, M. J. et al. 2010, A&A, 518, L3, 1005.5123

Griffin, M. J., Swinyard, B. M., & Vigroux, L. G. 2003, in Society of Photo-Optical Instrumentation Engineers (SPIE) Conference Series, Vol. 4850, Society of Photo-Optical Instrumentation Engineers (SPIE) Conference Series, ed. J. C. Mather, 686–697

Guo, Q. et al. 2011, MNRAS, 412, 2277, 1011.3048

Guth, A. H. 1981, Phys. Rev. D, 23, 347

Haiman, Z., & Knox, L. 2000, ApJ, 530, 124, arXiv:astro-ph/9906399

Hajian, A. et al. 2011, ApJ, 740, 86, 1009.0777

Hall, N. R. et al. 2010, ApJ, 718, 632, 0912.4315

Hand, N. et al. 2012, Physical Review Letters, 109, 041101, 1203.4219

Hashimoto, Y., Oemler, Jr., A., Lin, H., & Tucker, D. L. 1998, ApJ, 499, 589, arXiv:astro-ph/9712319

Haslam, C. G. T., Stoffel, H., Salter, C. J., & Wilson, W. E. 1982, A&AS, 47, 1

Hauser, M. G., & Dwek, E. 2001, ARA&A, 39, 249, arXiv:astro-ph/0105539

Hauser, M. G., Kelsall, T., Moseley, Jr., S. H., Silverberg, R. F., Murdock, T., Toller, G., Spiesman, W., & Weiland, J. 1991, in American Institute of Physics Conference Series, Vol. 222, After the first three minutes, ed. S. S. Holt, C. L. Bennett, & V. Trimble, 161–178

Hayward, C. C., Jonsson, P., Kereš, D., Magnelli, B., Hernquist, L., & Cox, T. J. 2012, MNRAS, 424, 951, 1203.1318

Hernández-Monteagudo, C., & Ho, S. 2009, MNRAS, 398, 790, 0903.2814

Hezaveh, Y. D., & Holder, G. P. 2011, ApJ, 734, 52, 1010.0998

Hezaveh, Y. D., Marrone, D. P., & Holder, G. P. 2012, ArXiv e-prints, 1203.3267

Hildebrand, R. H. 1983, QJRAS, 24, 267

Hincks, A. D. et al. 2010, ApJS, 191, 423, 0907.0461

Hinshaw, G. et al. 2009, ApJS, 180, 225, 0803.0732

Hivon, E., Górski, K. M., Netterfield, C. B., Crill, B. P., Prunet, S., & Hansen, F. 2002, ApJ, 567, 2, astro-ph/0105302

Holland, W. S. et al. 1999, MNRAS, 303, 659, arXiv:astro-ph/9809122

Hu, W., & White, M. 1996, ApJ, 471, 30

Hughes, D. H. et al. 1998, Nature, 394, 241, arXiv:astro-ph/9806297

Hui, L., & Parfrey, K. P. 2008, Phys. Rev. D, 77, 043527, 0712.1162

Hwang, H. S. et al. 2010, MNRAS, 409, 75, 1009.1058

Ilić, S., Douspis, M., Langer, M., Pénin, A., & Lagache, G. 2011, MNRAS, 416, 2688, 1106.2328

Iliev, I. T., Pen, U.-L., Richard Bond, J., Mellema, G., & Shapiro, P. R. 2006, New A Rev., 50, 909, arXiv:astro-ph/0607209

Jenkins, A., Frenk, C. S., White, S. D. M., Colberg, J. M., Cole, S., Evrard, A. E., Couchman, H. M. P., & Yoshida, N. 2001, MNRAS, 321, 372

Kaiser, N. 1992, ApJ, 388, 272

Kashlinsky, A. 2005, Phys. Rep., 409, 361, arXiv:astro-ph/0412235

Kashlinsky, A., & Odenwald, S. 2000, ApJ, 528, 74, arXiv:astro-ph/9908304

Keisler, R. et al. 2011, ApJ, 743, 28, 1105.3182

Kennicutt, Jr., R. C. 1983, AJ, 88, 483

——. 1998, ApJ, 498, 541, arXiv:astro-ph/9712213

Kessler, M. F. et al. 1996, A&A, 315, L27

Knox, L., Cooray, A., Eisenstein, D., & Haiman, Z. 2001, ApJ, 550, 7, arXiv:astro-ph/0009151

Knox, L., Scoccimarro, R., & Dodelson, S. 1998, Physical Review Letters, 81, 2004, arXiv:astro-ph/9805012

Komatsu, E., & Kitayama, T. 1999, ApJ, 526, L1

Komatsu, E., & Seljak, U. 2002, MNRAS, 336, 1256

Komatsu, E. et al. 2011, ApJS, 192, 18, 1001.4538

Kosowsky, A., & Turner, M. S. 1995, Phys. Rev. D, 52, 1739

Kravtsov, A. V., Berlind, A. A., Wechsler, R. H., Klypin, A. A., Gottlöber, S., Allgood, B., & Primack, J. R. 2004, ApJ, 609, 35, arXiv:astro-ph/0308519

Lagache, G., Abergel, A., Boulanger, F., Désert, F. X., & Puget, J.-L. 1999, A&A, 344, 322, arXiv:astro-ph/9901059

Lagache, G., Bavouzet, N., Fernandez-Conde, N., Ponthieu, N., Rodet, T., Dole, H., Miville-Deschênes, M.-A., & Puget, J.-L. 2007, ApJ, 665, L89, 0707.2443

Lagache, G., Dole, H., & Puget, J.-L. 2003, MNRAS, 338, 555, arXiv:astro-ph/0209115

Lagache, G. et al. 2004, ApJS, 154, 112, arXiv:astro-ph/0406016

Lamarre, J.-M. et al. 2010, A&A, 520, A9

Lapi, A. et al. 2011, ApJ, 742, 24, 1108.3911

Lawrence, E., Heitmann, K., White, M., Higdon, D., Wagner, C., Habib, S., & Williams, B. 2010, ApJ, 713, 1322, 0912.4490

Le Floc'h, E. et al. 2005, ApJ, 632, 169, arXiv:astro-ph/0506462

——. 2007, ApJ, 660, L65, arXiv:astro-ph/0609466

Lee, K.-S., Giavalisco, M., Gnedin, O. Y., Somerville, R. S., Ferguson, H. C., Dickinson, M., & Ouchi, M. 2006, ApJ, 642, 63, arXiv:astro-ph/0508090

Leger, A., & Puget, J. L. 1984, A&A, 137, L5

Lewis, A., & Challinor, A. 2006, Phys. Rep., 429, 1, arXiv:astro-ph/0601594

Lewis, A., Challinor, A., & Lasenby, A. 2000, ApJ, 538, 473, arXiv:astro-ph/9911177

Lima, M., Jain, B., & Devlin, M. 2010a, MNRAS, 406, 2352, 0907.4387

Lima, M., Jain, B., Devlin, M., & Aguirre, J. 2010b, ApJ, 717, L31, 1004.4889

Limber, D. N. 1953, ApJ, 117, 134

Linde, A. D. 1982, Phys. Lett., B108, 389

Lueker, M. et al. 2010, ApJ, 719, 1045, 0912.4317

Lutz, D., Valiante, E., Sturm, E., Genzel, R., Tacconi, L. J., Lehnert, M. D., Sternberg, A., & Baker, A. J. 2005, ApJ, 625, L83, arXiv:astro-ph/0504431

Maddox, S. J. et al. 2010, A&A, 518, L11, 1005.2406

Magnelli, B., Elbaz, D., Chary, R. R., Dickinson, M., Le Borgne, D., Frayer, D. T., & Willmer, C. N. A. 2011, A&A, 528, A35+, 1101.2467

Mandelbaum, R., Slosar, A., Baldauf, T., Seljak, U., Hirata, C. M., Nakajima, R., Reyes, R., & Smith, R. E. 2012, ArXiv e-prints, 1207.1120

Marriage, T. A. et al. 2011a, ApJ, 737, 61, 1010.1065

——. 2011b, ApJ, 731, 100, 1007.5256

Marsden, G. et al. 2009, ApJ, 707, 1729, 0904.1205

——. 2011, MNRAS, 417, 1192, 1010.1176

Marshall, P., Rajguru, N., & Slosar, A. 2006, Phys. Rev. D, 73, 067302, arXiv:astro-ph/0412535

Mather, J. C., Fixsen, D. J., & Shafer, R. A. 1993, in Society of Photo-Optical Instrumentation Engineers (SPIE) Conference Series, Vol. 2019, Society of Photo-Optical Instrumentation Engineers (SPIE) Conference Series, ed. M. S. Scholl, 168–179

Matsuura, S. et al. 2011, ApJ, 737, 2, 1002.3674

McMahon, J. J. et al. 2009, in American Institute of Physics Conference Series, Vol. 1185, American Institute of Physics Conference Series, ed. B. Young, B. Cabrera, & A. Miller, 511–514

Mead, J. M. G., King, L. J., Sijacki, D., Leonard, A., Puchwein, E., & McCarthy, I. G. 2010, MNRAS, 406, 434, 1001.2281

Mesinger, A., McQuinn, M., & Spergel, D. N. 2012, MNRAS, 422, 1403, 1112.1820

Metropolis, N., Rosenbluth, A. W., & Rosenbluth, M. N. and Teller, A. H. 1953, J. Chem. Phys., 21, 1087

Millea, M., Doré, O., Dudley, J., Holder, G., Knox, L., Shaw, L., Song, Y.-S., & Zahn, O. 2012, ApJ, 746, 4, 1102.5195

Miville-Deschênes, M.-A., Boulanger, F., Reach, W. T., & Noriega-Crespo, A. 2005, ApJ, 631, L57, arXiv:astro-ph/0508154

Miville-Deschênes, M.-A., Lagache, G., Boulanger, F., & Puget, J.-L. 2007, A&A, 469, 595, 0704.2175

Miville-Deschênes, M.-A., Ysard, N., Lavabre, A., Ponthieu, N., Macías-Pérez, J. F., Aumont, J., & Bernard, J. P. 2008, A&A, 490, 1093, 0802.3345

Navarro, J. F., Frenk, C. S., & White, S. D. M. 1996, ApJ, 462, 563, arXiv:astro-ph/9508025

Negrello, M. et al. 2010, Science, 330, 800, 1011.1255

Negrello, M., Perrotta, F., González-Nuevo, J., Silva, L., de Zotti, G., Granato, G. L., Baccigalupi, C., & Danese, L. 2007, MNRAS, 377, 1557, arXiv:astro-ph/0703210

Netterfield, C. B., et al. 2002, ApJ, 571, 604, astro-ph/0104460

Neugebauer, G. et al. 1984, ApJ, 278, L1

Niemack, M. D. et al. 2010, in Society of Photo-Optical Instrumentation Engineers (SPIE) Conference Series, Vol. 7741, Society of Photo-Optical Instrumentation Engineers (SPIE) Conference Series, 1006.5049

Nozawa, S., Itoh, N., & Kohyama, Y. 1998, ApJ, 508, 17, arXiv:astro-ph/9804051

Nozawa, S., Itoh, N., Suda, Y., & Ohhata, Y. 2006, Nuovo Cimento B Serie, 121, 487, arXiv:astro-ph/0507466

Oliver, S. J. et al. 2010, A&A, 518, L21, 1005.2184

Ostriker, J. P., & Vishniac, E. T. 1986, ApJ, 306, L51

Ouchi, M. et al. 2005, ApJ, 635, L117, arXiv:astro-ph/0508083

Pannella, M. et al. 2009, ApJ, 698, L116, 0905.1674

Pascale, E. et al. 2008, ApJ, 681, 400, 0711.3465

——. 2009, ApJ, 707, 1740, 0904.1206

Patanchon, G. et al. 2009, ApJ, 707, 1750, 0906.0981

Patel, H., Clements, D. L., Vaccari, M., Mortlock, D. J., Rowan-Robinson, M., & Perez-Fournon, I. 2012, ArXiv e-prints, 1205.5690

Peacock, J. A., & Smith, R. E. 2000, MNRAS, 318, 1144, arXiv:astro-ph/0005010

Peebles, P. J. E. 1980, The large-scale structure of the universe (Research supported by the National Science Foundation. Princeton, N.J., Princeton University Press, 1980. 435 p.)

Pénin, A. et al. 2012, A&A, 543, A123, 1105.1463

Penzias, A. A., & Wilson, R. W. 1965, ApJ, 142, 419

Percival, W. J. et al. 2010, MNRAS, 401, 2148, 0907.1660

Pérez-González, P. G. et al. 2005, ApJ, 630, 82, arXiv:astro-ph/0505101

Perrotta, F., Baccigalupi, C., Bartelmann, M., De Zotti, G., & Granato, G. L. 2002, MNRAS, 329, 445

Pilbratt, G. L. et al. 2010, A&A, 518, L1, 1005.5331

Planck Collaboration. 2012, ArXiv e-prints, 1207.4706

Planck Collaboration et al. 2011a, A&A, 536, A1, 1101.2022

——. 2011b, A&A, 536, A16, 1101.2045

——. 2011c, A&A, 536, A18, 1101.2028

——. 2011d, A&A, 536, A10, 1101.2043

Planck HFI Core Team et al. 2011a, A&A, 536, A4

——. 2011b, A&A, 536, A6, 1101.2048

Poglitsch, A. et al. 2010, A&A, 518, L2, 1005.1487

Pozzi, F. et al. 2004, ApJ, 609, 122, arXiv:astro-ph/0403242

Press, W. H., & Schechter, P. 1974, ApJ, 187, 425

Puget, J.-L., Abergel, A., Bernard, J.-P., Boulanger, F., Burton, W. B., Desert, F.-X., & Hartmann, D. 1996, A&A, 308, L5+

Reed, D. S., Smith, R. E., Potter, D., Schneider, A., Stadel, J., & Moore, B. 2012, ArXiv e-prints, 1206.5302

Reichardt, C. L. et al. 2009a, ApJ, 694, 1200, 0801.1491

Reichardt, C. L., de Putter, R., Zahn, O., & Hou, Z. 2012a, ApJ, 749, L9, 1110.5328

Reichardt, C. L. et al. 2012b, ApJ, 755, 70, 1111.0932

——. 2009b, ApJ, 701, 1958, 0904.3939

Reid, B. A., & Spergel, D. N. 2009, ApJ, 698, 143, 0809.4505

Riess, A. G. et al. 2011, ApJ, 730, 119, 1103.2976

Righi, M., Hernández-Monteagudo, C., & Sunyaev, R. A. 2008, A&A, 478, 685, 0707.0288

Rodighiero, G. et al. 2010, A&A, 515, A8, 0910.5649

Sajina, A., Scott, D., Dennefeld, M., Dole, H., Lacy, M., & Lagache, G. 2006, MNRAS, 369, 939, arXiv:astro-ph/0603614

Sajina, A., Yan, L., Fadda, D., Dasyra, K., & Huynh, M. 2012, ArXiv e-prints, 1207.4963

Santos, M. G., et al. 2003, MNRAS, 341, 623, astro-ph/0211123

Saunders, W., Rowan-Robinson, M., Lawrence, A., Efstathiou, G., Kaiser, N., Ellis, R. S., & Frenk, C. S. 1990, MNRAS, 242, 318

Sayers, J. et al. 2009, ApJ, 690, 1597, 0805.3151

Schechter, P. 1976, ApJ, 203, 297

Scheuer, P. A. G. 1957, Proceedings of the Cambridge Philosophical Society, 53, 764

Scoccimarro, R., Feldman, H. A., Fry, J. N., & Frieman, J. A. 2001, ApJ, 546, 652, arXiv:astro-ph/0004087

Scott, D., & Smoot, G. 2006, ArXiv Astrophysics e-prints, arXiv:astro-ph/0601307

Scott, D., & White, M. 1999, A&A, 346, 1, arXiv:astro-ph/9808003

Scott, K. S. et al. 2010, ApJS, 191, 212, 1007.0038

Sehgal, N., Bode, P., Das, S., Hernandez-Monteagudo, C., Huffenberger, K., Lin, Y.-T., Ostriker, J. P., & Trac, H. 2010, ApJ, 709, 920, 0908.0540

Sehgal, N. et al. 2011, ApJ, 732, 44, 1010.1025

Shang, C., Haiman, Z., Knox, L., & Oh, S. P. 2012, MNRAS, 2559, 1109.1522

Sharp, M. K. et al. 2010, ApJ, 713, 82, 0901.4342

Shaw, L. D., Nagai, D., Bhattacharya, S., & Lau, E. T. 2010, ApJ, 725, 1452, 1006.1945

Shaw, L. D., Zahn, O., Holder, G. P., & Doré, O. 2009, ApJ, 702, 368, 0903.5322

Sherwin, B. D. et al. 2012, ArXiv e-prints, 1207.4543

Sheth, R. K., Mo, H. J., & Tormen, G. 2001, MNRAS, 323, 1, arXiv:astro-ph/9907024

Sheth, R. K., & Tormen, G. 1999, MNRAS, 308, 119

Shirokoff, E. et al. 2011, ApJ, 736, 61, 1012.4788

Sievers, J. L. et al. 2009, ArXiv e-prints, 0901.4540

Silk, J. 1968, ApJ, 151, 459

Smail, I., Ivison, R. J., & Blain, A. W. 1997, ApJ, 490, L5, arXiv:astro-ph/9708135

Smith, K. M., Zahn, O., & Doré, O. 2007, Phys. Rev. D, 76, 043510, 0705.3980

Smith, R. E. et al. 2003, MNRAS, 341, 1311

Spergel, D. N. et al. 2007, ApJS, 170, 377, arXiv:astro-ph/0603449

——. 2003, ApJS, 148, 175

Staniszewski, Z. et al. 2009, ApJ, 701, 32, 0810.1578

Stansberry, J. A. et al. 2007, PASP, 119, 1038, 0707.2103

Sunyaev, R. A., & Zeldovich, I. B. 1980, MNRAS, 190, 413

Sunyaev, R. A., & Zel'dovich, Y. B. 1970, Ap&SS, 7, 3

Sunyaev, R. A., & Zeldovich, Y. B. 1972, Comments on Astrophysics and Space Physics, 4, 173

Swetz, D. S. et al. 2011, ApJS, 194, 41, 1007.0290

Swinyard, B. M. et al. 2010, A&A, 518, L4, 1005.5073

Taburet, N., Hernández-Monteagudo, C., Aghanim, N., Douspis, M., & Sunyaev, R. A. 2011, MNRAS, 418, 2207

Takeuchi, T. T., Yoshikawa, K., & Ishii, T. T. 2003, ApJ, 587, L89, arXiv:astro-ph/0303181

Tauber, J. A. et al. 2010, A&A, 520, A1

Tegmark, M. et al. 2004, ApJ, 606, 702

——. 2002, ApJ, 571, 191, arXiv:astro-ph/0107418

Tinker, J., Kravtsov, A. V., Klypin, A., Abazajian, K., Warren, M., Yepes, G., Gottlöber, S., & Holz, D. E. 2008, ApJ, 688, 709, 0803.2706

Tinker, J. L., Robertson, B. E., Kravtsov, A. V., Klypin, A., Warren, M. S., Yepes, G., & Gottlöber, S. 2010a, ApJ, 724, 878, 1001.3162

Tinker, J. L. et al. 2012, ApJ, 745, 16, 1104.1635

Tinker, J. L., Wechsler, R. H., & Zheng, Z. 2010b, ApJ, 709, 67, 0902.1748

Tinker, J. L., Weinberg, D. H., Zheng, Z., & Zehavi, I. 2005, ApJ, 631, 41, arXiv:astro-ph/0411777

Trac, H., Bode, P., & Ostriker, J. P. 2011, ApJ, 727, 94, 1006.2828

Truch, M. D. P. et al. 2009, ApJ, 707, 1723, 0904.1202

Vaccari, M. et al. 2010, A&A, 518, L20, 1005.2187

Valiante, E. et al. 2010, ApJS, 191, 222, 1007.3259

van Engelen, A. et al. 2012, ApJ, 756, 142, 1202.0546

Vanderlinde, K. et al. 2010, ApJ, 722, 1180, 1003.0003

Vieira, J. D. et al. 2010, ApJ, 719, 763, 0912.2338

Viero, M. P. et al. 2009, ApJ, 707, 1766, 0904.1200

Vishniac, E. T. 1987, ApJ, 322, 597

Wake, D. A. et al. 2011, ApJ, 728, 46, 1012.1317

Wang, L. et al. 2012, ArXiv e-prints, 1203.5828

Warren, M. S., Abazajian, K., Holz, D. E., & Teodoro, L. 2006, ApJ, 646, 881, arXiv:astro-ph/0506395

Watson, D. F., Berlind, A. A., & Zentner, A. R. 2011, ApJ, 738, 22, 1101.5155

Weinberg, S. 2008, Cosmology (Oxford University Press)

Werner, M. W. et al. 2004, ApJS, 154, 1, arXiv:astro-ph/0406223

White, M. et al. 2011, ApJ, 728, 126, 1010.4915

White, M. J., & Majumdar, S. 2004, Astrophys. J., 602, 565, astro-ph/0308464

Wright, E. L. et al. 1992, ApJ, 396, L13

Xia, J.-Q., Negrello, M., Lapi, A., de Zotti, G., Danese, L., & Viel, M. 2012, MNRAS, 2554, 1111.4212

Yan, L. et al. 2005, ApJ, 628, 604, arXiv:astro-ph/0504336

Yoo, J., Weinberg, D. H., Tinker, J. L., Zheng, Z., & Warren, M. S. 2009, ApJ, 698, 967, 0808.2988

Zahn, O. et al. 2012, ApJ, 756, 65, 1111.6386

Zehavi, I. et al. 2002, ApJ, 571, 172, arXiv:astro-ph/0106476

——. 2004, ApJ, 608, 16, arXiv:astro-ph/0301280

——. 2011, ApJ, 736, 59, 1005.2413

——. 2005, ApJ, 630, 1

Zheng, Z. et al. 2005, ApJ, 633, 791, arXiv:astro-ph/0408564

Zheng, Z., Zehavi, I., Eisenstein, D. J., Weinberg, D. H., & Jing, Y. P. 2009, ApJ, 707, 554, 0809.1868